Liquid Crystal Mixed Beam-Switching and Beam-Steering Network in Hybrid Metallic and Dielectric Waveguide Technology

Matthias Jost

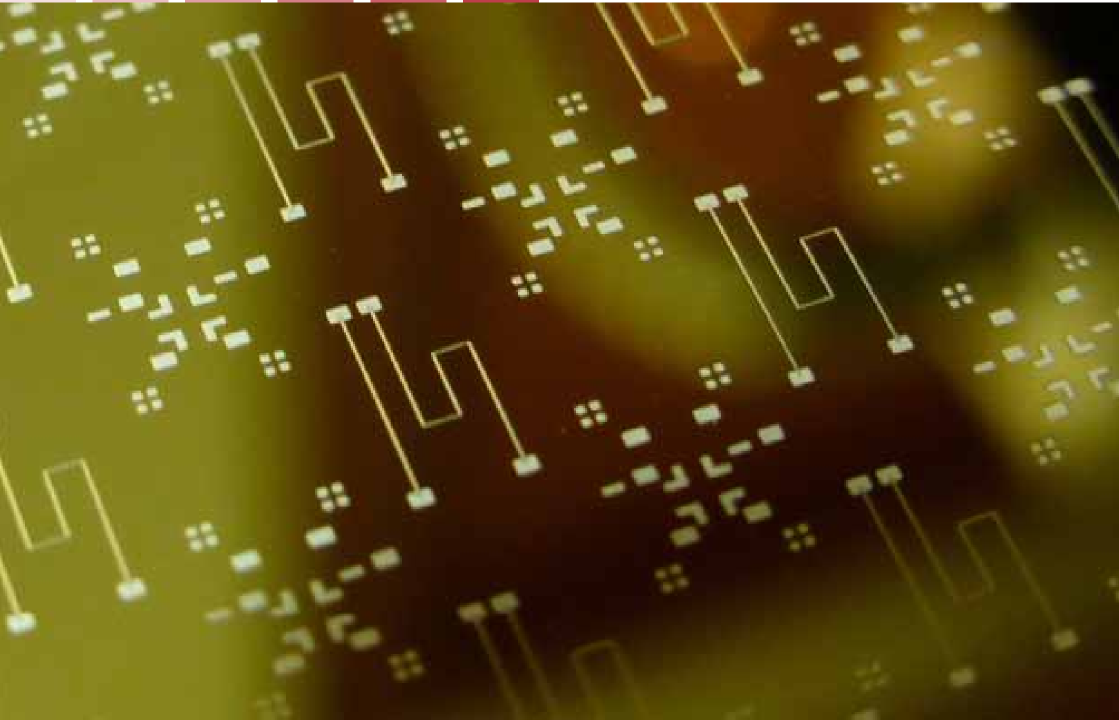

Liquid Crystal Mixed Beam-Switching and Beam-Steering Network in Hybrid Metallic and Dielectric Waveguide Technology

Vom Fachbereich Elektrotechnik und Informationstechnik
der Technischen Universität Darmstadt
zur Erlangung des akademischen Grades eines
Doktor-Ingenieurs (Dr.-Ing.)
genehmigte

Dissertation

von

Dipl.-Phys.
Matthias Jost
geboren am 10.07.1985
in Birkenfeld (Nahe), Deutschland

Referent:	Prof. Dr.-Ing. Rolf Jakoby
Korreferent:	Prof. Dr. Philippe Ferrari

Tag der Einreichung:	02.02.2018
Tag der mündlichen Prüfung:	26.04.2018

D17
Darmstadt 2018

Berichte aus der Hochfrequenztechnik

Matthias Jost

Liquid Crystal Mixed Beam-Switching and Beam-Steering Network in Hybrid Metallic and Dielectric Waveguide Technology

D 17 (Diss. TU Darmstadt)

Shaker Verlag
Aachen 2018

Bibliographic information published by the Deutsche Nationalbibliothek
The Deutsche Nationalbibliothek lists this publication in the Deutsche Nationalbibliografie; detailed bibliographic data are available in the Internet at http://dnb.d-nb.de.

Zugl.: Darmstadt, Techn. Univ., Diss., 2018

Printed in Germany.

ISBN 978-3-8440-6042-3
ISSN 0945-0793

Shaker Verlag GmbH • P.O. BOX 101818 • D-52018 Aachen
Phone: 0049/2407/9596-0 • Telefax: 0049/2407/9596-9
Internet: www.shaker.de • e-mail: info@shaker.de

Erklärung laut § 9 der Promotionsordnung

Ich versichere hiermit, dass ich die vorliegende Dissertation allein und nur unter Verwendung der angegebenen Literatur verfasst habe. Die Arbeit hat bisher noch nicht zu Prüfungszwecken gedient.

Darmstadt, den 02.02.2018

Preface

This thesis presents my research results performed as a Ph.D. candidate in the Institute for Microwave Engineering and Photonics (IMP) at Technische Universität Darmstadt. At this point, I would like to acknowledge all the people who supported me on the long way to my doctorate.

First, I want to sincerely thank my supervisor Prof. Dr.-Ing. Rolf Jakoby for his trustful and patient guidance throughout my complete Ph.D. time. The high degree of freedom he offered for my research activities together with the responsibilities he assigned me within our team allowed me to improve myself in the scientific, personal and cultural point of view. Mahalo!

A special thanks goes to Prof. Dr. Philippe Ferrari from the Institut de Microélectronique Electromagnétisme et Photonique and Laboratoire d'Hyperfréquences et de Caractérisation (IMEP-LaHC) for evaluating this dissertation, for the fruitful cooperation throughout the years and for always providing me a different perspective on certain challenges.

Many thanks also go to:

- Dr.-Ing. Carsten Fritzsch, Dr. Herbert Plach and Dr. Michael Wittek from Merck KGaA
- Prof. Dr. Gustavo P. Rehder, Prof. Dr. Ariana L. C. Serrano and Leonardo G. Gomes from the Laboratório de Microeletrônica at Universidade de São Paulo
- Bärbel Schulz, Andreas Heunisch and Dr. Torsten Rabe from the Bundesanstalt für Materialforschung und -prüfung
- Dr. Rüdiger Follmann and Matthias Quibeldey from IMST GmbH
- Dr. Anke Pagels-Kerp from Deutsches Zentrum für Luft- und Raumfahrt

Special thanks go to Dr. Martin Letz from Schott AG. His "golden rules" have proven to be very useful and have always inspired me. Also, I want to thank my former fellow students Dr. Julian Lingner and Dr. Hubertus P. Braun.

I am very grateful for having the opportunity to interact with so many great personalities during my time at the IMP. Specifically I want to name Dr.-Ing. Alex Wiens for always offering a helping hand and for sharing the same sense of humor, Sönke Schmidt for a great time and all the "fruitful" discussions in 417, as well as Roland Reese, without whom this work would not have been as successful as it became. Further, I would like to express my appreciation to Dr.-Ing. Christian Weickhmann, Dr.-Ing. Sebastian Strunck, Dr.-Ing. Matthias Maasch, Christian Schuster, Ersin Polat, Matthias Nickel, Dr.-Ing. Holger Maune and Prof. Dr.-Ing. Christian Damm for their support, as well as Dr.-Ing. Martin Schüßler, Dr.-Ing. Matthias Hansli and Henning Tesmer for the musical after work program.

The technical staff from IMP and EMK are highly acknowledged, since most components within this thesis were only realisable due to their high expertise: Peter Kießlich, Andreas Semrad, Karin Boye, Silke Schober, Walter Albrecht, Corinna Harsche, Viktor Fröse and Tom Schildknecht.

Last but not least I want to thank my family, friends and especially my wife Alexandra. Without their unconditional motivation and support, this thesis would not have been possible!

Mainz, June 2018 Matthias Jost

Kurzfassung

Zukünftige Kommunikationssysteme im W-Band erfordern nicht nur direktive, sondern zur Strahlführung ebenso rekonfigurierbare Antennensysteme. Für die Realisierung solcher adaptiven Systeme sind speziell für den Mikrowellenbereich synthetisierte Flüssigkristalle (engl.: Liquid Crystal, LC) bestens geeignet. Durch die Integration in geeignete Komponenten mit entsprechenden Ansteuerkonzepten, kann die Orientierung der Flüssigkristalle und damit die effektive Permittivität kontinuierlich gesteuert werden. Zudem weisen diese Flüssigkristalle oberhalb von 10 GHz geringe dielektrische Verluste auf, welche mit steigender Frequenz sogar sinken. Um diese einzigartigen Eigenschaften des Materials auszunutzen, liegt der Fokus der vorliegenden wissenschaftlichen Arbeit erstmals auf der Untersuchung eines LC-basierten Antennennetzwerks im W-Band, welches auf einer Kombination aus einer diskreten Strahlumschaltung und einer kontinuierlichen Strahlsteuerung zwischen den umgeschalteten Zuständen beruht. Dieses Netzwerk basiert auf einer Butler-Matrix, welche mit kontinuierlich steuerbaren LC-Phasenschiebern erweitert wird. Für die Auswahl der Butler-Matrix Eingänge wird ein neuartiger, interferenzbasierter HF-Schalter verwendet. Das Interferenzprinzip dieses speziellen Schalters erlaubt ein stufenlos einstellbares Verhältnis der Ausgangsleistungen, welches für die zeitgleiche Anregung mehrerer Signale erforderlich ist und mit dem somit gleichzeitig mehrere Antennenkeulen generiert werden.

Für die Realisierung des gemischten strahlumschaltenden und strahlsteuerndn Netzwerks werden verschiedene Technologien untersucht. Aufgrund der hohen Integrationsfähigkeit und kompakten Bauweise wird die Niedertemperatur-Einbrand-Keramik-Technologie für einen ersten Machbarkeitsnachweis, allerdings nur im Ka-Band, untersucht. Für das W-Band werden verlustarme Technologien in Form von metallischen Rechteckhohlleitern und dielektrischen Wellenleitern untersucht. Während sich Hohlleiter exzellent für die Realisierung der nicht steuerbaren Verteilnetzwerke eignen, sind dielektrische Wellenleiter eine sehr vielversprechende Alternative zur Realisierung der steuerbaren LC-Komponenten, da keine metallischen Berandungen die Integration von Steuerelektroden limitiert. Als nicht steuerbare Kernkomponente des angestrebten Netzwerks wird eine Butler-Matrix mit einem Einfügeverlust von im Mittel 3,5 dB bei 102 GHz präsentiert. Diese basiert

auf einer neuartigen, multifunktionellen Hohlleiterkreuzung, welche zudem eine miniaturisierte Realisierung des gesamten Netzwerks in einer einzigen Ebene erlaubt. Als Schlüsselkomponente für die Steuerbarkeit des Netzwerks wird ein kontinuierlich steuerbarer Stufenindex-LC-Phasenschieber realisiert. Mit einer Phasenschiebergüte von 100 °/dB bei 102 GHz übertrifft dieser elektrisch steuerbare Phasenschieber deutlich den heutigen Stand der Technik für elektrisch steuerbare W-Band-Phasenschieber.

Um vom Eingangsport bis hin zu den Antennenelementen eine Realisierung in einer Ebene gewährleisten zu können, wird auf der gleichen technologischen Plattform die hybride Integration aus verlustarmen metallischen Hohlleitern und steuerbaren dielektrischen Wellenleitern hoher Güte am Beispiel des interferenzbasierten HF Schalters untersucht. Der vorgestellte Demonstrator weist eine Einfügedämpfung von 3 dB auf, während eine Isolation von 27 dB erreicht wird. Die hybride Integration von nicht-steuerbaren metallischen Hohlleitern und hochperformanten steuerbaren dielektrischen Wellenleitern weist somit ein hohes Potenzial auf, nicht nur für die Realisierung des angestrebten LC-basierten Antennennetzerks, sondern allgemein für die Realisierung LC-basierter, steuerbarer Antennensysteme oberhalb von 100 GHz.

Abstract

Future communication systems at W-band are demanding highly directive antenna systems with beam-steering capability. For the hardware implementation of analogue beam-steering at millimetre waves, the microwave liquid crystal (LC) technology is ideally suited. It takes advantage of specifically synthesised LCs for microwaves in combination with appropriate device and biasing concepts, where the orientation of the LC, and therefore, its effective permittivity can be continuously tuned. It has low dielectric losses above 10 GHz with a decreasing trend with increasing frequency. To exploit these unique characteristics, the focus of this scientific work is set for the first time on the investigation of an LC-based network with mixed discrete beam-switching and continuous beam-steering capability between the switching states for high-gain antennas at W-band. It consists of a Butler matrix combined with continuously tuneable phase shifters and a novel type of RF switch, an interference-based Single-Pole n-Throw (SPnT). The interference principle of the SPnT allows a continuously adjustable power splitting ratio, and hence, the generation of multiple beams.

Different technologies are investigated for the realisation of this mixed network. Due to its high level of integrability and compact designs, the standard low temperature co-fired ceramic technology is examined, however, for a first proof-of-concept at Ka-band only. For W-band, two low-loss technologies are investigated: tuneable metallic and dielectric waveguides. While metallic waveguides are well suited for the realisation of low-loss non-tuneable feeding networks, dielectric waveguides are better suited for the realisation of tuneable LC components at (sub)millimetre waves, since no metallic boundaries are limiting the integration of an electrical biasing network. As non-tuneable core part, a Butler matrix with an average insertion loss of 3.5 dB at 102 GHz is realised, which is based on a novel multifunctional crossover design, allowing a miniaturised in-plane realisation of the overall mixed network. As key component for tuning of the mixed beam-switching and beam-steering network, a step-index dielectric waveguide phase shifter is presented. With a phase shifter figure-of-merit of 100 °/dB at 102 GHz, this fully electrically biased phase shifter is going far beyond the state-of-the-art for electrically tuneable W-band phase shifter.

To stay on the same technology platform and to allow an in-plane realisation from the input port up to the radiating elements, the interference-based SPnTs are additionally investigated by a hybrid implementation of metallic and dielectric waveguides. It exhibits an insertion loss of 3 dB, while providing an isolation of 27 dB. Hence, this hybrid metallic and dielectric waveguide technology reveals a high potential not only for the presented LC-based mixed beam-switching and beam-steering network, but also for LC-tuned continuous beam-steering networks at frequencies above 100 GHz, since low-loss metallic waveguide feeding networks can be generally combined with high-performance tuneable dielectric waveguides.

Contents

1 Introduction

Due to the steadily increasing demand for higher data rates as well as the current developments in fields such as radar imaging or radiometry, high-performance components are required, especially in the millimetre wave range. While W-band frequencies from 75 GHz to 110 GHz are already used in radiometry, e.g. for measuring water vapor, rain, etc. [Pei+04], the frequency range above 70 GHz with its extremely large bandwidths, e.g. from 71 GHz to 76 GHz destined for mobile and broadcast satellite communications, is currently insufficiently used for communication [Bun16]. However, it offers a promising alternative to the steadily ongoing increase in spectral efficiency at lower frequency bands such as the Ku- and Ka-band. Several bands[1] have been released for the usage in a wide range of new products and services such as high-speed point-to-point wireless local area networks and broadband internet access [Riv+14].

While rain is the dominant loss factor of atmospheric impairments at Ku-band, gases and clouds need to be taken into account at W-band frequencies, too. Why especially this frequency band is well-suited for communication, can be seen in Fig. 1.1. Oxygen and water vapour are the only gases which are significantly affecting the electromagnetic waves [Riv+14]. While the specific attenuation of water increases nearly steadily with increasing frequency, the oxygen attenuation is strongly frequency dependent due to resonant absorptions. Where the oxygen attenuation is around 15 dB/km at 60 GHz, it reduces down to $9 \cdot 10^{-3}$ dB/km in the frequency range between 90 GHz to 100 GHz. The corresponding water vapour attenuation in this frequency range is 0.4 dB/km to 0.5 dB/km. Accompanied with the increasing free-space path loss with increasing frequency, 60 GHz systems are only reasonable for short distance connections or inter-satellite links. Despite the increased free-space path loss, W-band systems can additionally be used for providing reliable data transmissions between ground stations and satellites.

For many applications in the (sub)millimetre wave range, e.g. for mobile systems of the 5th generation or satellite communication, antennas require a very high gain to compensate the free-space path loss. Thus, highly directive antennas or

---

[1] 71 GHz to 76 GHz, 81 GHz to 86 GHz and 92 GHz to 95 GHz

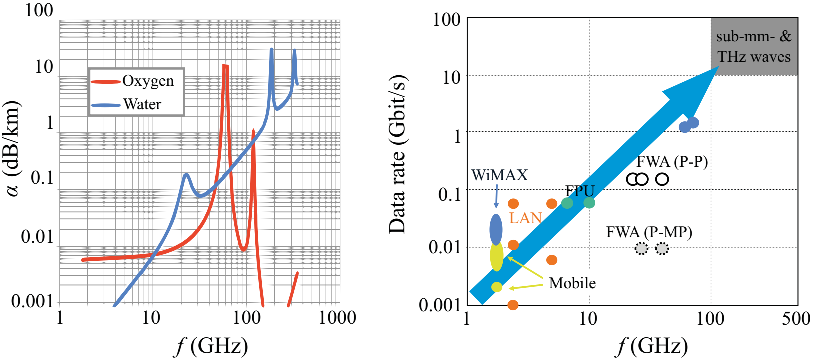

Figure 1.1: (left) Specific attenuation due to atmospheric gases [R16] and (right) relationship between carrier frequency and data rate in various wireless communications technologies [AST11].

antenna arrays with a large number of elements are needed. By increasing the number of antenna elements, highly directional pencil beams can be generated. To compensate a shift of the pencil beam due to mechanical vibrations as well as for tracking or on-the-move applications, adaptive beam-steering is mandatory. In the micro- and millimetre wave range, this is exemplarily provided by mechanically moving parabolic antennas. However, this is associated with high maintenance efforts and costs. Therefore, an electronic beam-steering without mechanically moving components is aimed for. By selectively adjusting the progressive phase shift between the individual antenna elements, the main beam direction of the antenna array can be changed. Particularly analogous techniques are of great interest, because of their easy and low-cost fabrication of large arrays, e.g. with 64 × 64 individual antenna elements. Further, even large passive arrays have a low power consumption.

Therefore, the scope of this work is the realisation of an *analogue electrically controlled mixed beam-switching and beam-steering network* for imaging and communication applications at W-band frequencies, being based on the discrete phase switching of the Butler matrix combined with continuously tuneable phase shifters.

A key component for the hardware implementation of analogue beam-steering is the phase shifter, being integrated into each signal path in front of the individual antenna elements. Phase shifters can be realised in different technologies. In semiconductor technologies, the GaAs, GaN and SiGe technologies are already established for this frequency range, but with the drawback of high losses and a low linearity in the desired millimetre wave range [Shi+07; Ozt+14; Den+11; Mar+14]. Nevertheless, they can be directly combined with active components, compensating the high loss, however, with the expense of a high power consumption and manufacturing cost. Microsystems (micro-electro-mechanical systems, MEMS) mainly allow discrete phase states by switching between different transmission line lengths. Together with their susceptibility of wear-out failures, due to the mechanically moving components, they are not really suitable for the implementation in large steerable antenna arrays with an extremely large number of switching cycles, e.g. for satellite applications [Som+12; Ste+08; Psy+13]. Tuneable components based on ferrites are also not an alternative for this application, since they require a high current flow for the provision of high magnetic field strengths, which are needed for tuning. Furthermore, they show increased losses in the desired frequency range [Hor89]. Ferroelectrics, which are already established for the lower GHz range, are suffering from high dielectric losses in the millimetre wave range, and therefore, are not considered for applications in the W-band [Vel+07; Koz+01].

The microwave liquid crystal (LC) technology, which has been innovatively developed during the last decade at TU Darmstadt, appears to be the most promising approach for tuneable components at millimetre waves, since the dielectric losses are on a very low level over a wide frequency range up to the THz regime [Wei+13a]. Up to now, the research on continuously tuneable LC components can be divided into two main categories:

1. high-performance waveguide-based devices [Gae15] and
2. low-profile components with fast response times [Kar14; Gö09].

The low profile components can be easily realised with automated manufacturing techniques similar to LC display technology, enabling a low-cost fabrication of large arrays even for a low-volume production. However, these planar structures have inherently higher losses than waveguide topologies, which are increasing with frequency. Therefore, the components investigated in this work are based on high-performance waveguide topologies, due to the required antenna efficiency. Beside the investigation of metallic waveguide topologies for the design of tuneable components, the main focus is on a new class of low-loss, lightweight tuneable dielectric waveguides. By the hybrid combination of both types of waveguides, low-loss mixed beam-switching and beam-steering networks can be realised at W-band.

This work is divided as follows. In chapter 2, the fundamentals of LC are presented to provide an insight on its unique properties for microwave applications. Chapter 3 describes the functional principle of the original beam-switching Butler matrix as well as the mixed beam-switching and beam-steering network, including the continuously LC-tuned phase shifters and single-pole double-throw (SPDT) with adjustable power-splitting ratio.

In chapter 4, low temperature co-fired ceramics (LTCC) are investigated as possible technology for the realisation of an embedded mixed beam-switching and beam-steering multilayer network. Exemplarily, tuneable phase shifters as well as SPDTs were realised at Ka-band frequencies, already including all non-tuneable components needed for a Butler matrix realisation.

In chapter 5, the applicability of the well-known LC-metallic waveguide technology is examined for W-band frequencies by means of a tuneable phase shifter as well as an SPDT. They are limited to a solely magnetically biasing, because of difficulties in the integration of an electrical biasing network. Although these components cannot be used in an electrically controlled mixed beam-switching and beam-steering network without an electrical biasing network, their performances will serve as reference for new, electrically biased technologies. Also, a non-tuneable Butler matrix was realised as a proof-of-concept for an in-plane waveguide topology based on a new innovative multifunctional crossover design.

To overcome the limitations of the LC-metallic waveguide technology, tuneable LC components based on dielectric waveguides are established for W-band frequencies and presented in chapter 6. Due to open boundaries compared to metallic waveguides, an easy implementation of the needed electrical biasing system is ensured. The system-inherently increased dimensions compared to metallic waveguides ensure an easy realisation even at frequencies in the submillimetre wave range, paving the way for tuneable high-performance LC components beyond 100 GHz. However, dielectric waveguides are prone to parasitic radiation, due to their loose field confinement, being overcome by the hybrid implementation of non-tuneable metallic and tuneable dielectric waveguides.

Finally, the results are summarised and further developments based on these research results are given. Moreover, an outlook about other approaches for the realisation of mixed beam-switching and beam steering networks for millimetre wave applications is given at the end on three different level: the component, fabrication and technology level.

2 Fundamentals of Liquid Crystal

In 1888, the Austrian botanist Friedrich Reinitzer from the German University of Prague published his observation of colourful phenomena while cooling down melts of cholesteryl acetate and benzoate. Furthermore, in cholesteryl benzoate he discovered what he defined as a "double melting point" at 145.5 °C and 178.5 °C. He described the liquid phase in between these melting points as a cloudy liquid, which he first assumed to be contaminated [Rei88]. In 1889, Otto Lehmann, who was working together with Reinitzer on the interpretation of the discovered effects, used the term of "liquid crystal" for the first time in his publication "Über fliessende Krystalle" (engl.: On liquid crystals) [Leh89]. While research on liquid crystals was going on at a low level during the following decades, it gained a high activity from the 1960s on, especially due to the nowadays well established liquid crystal display (LCD) technology. From 2002 on, research is also focussing on the implementation of the liquid crystal technology to microwave applications, e.g. as tuneable material in phased array antennas for SatCom applications.

The name "liquid crystal" (LC) is a combination of the material's main properties, since it is in a mesophase (from the greek word *μέσος* (meso) - middle) between a crystalline solid and an isotropic liquid. Therefore, it can flow like a common liquid while exhibiting characteristics, e.g. birefringence, common for crystalline structures. Due to the formation of mesophases, those kind of material systems are referred to as mesogenic compounds. Where crystals normally lose their translational periodicity as well as orientational order during the process of melting, mesogenic compounds show a stepwise melting through different mesophases, which is why liquid crystals partially retain orientational order [New05]. The most common liquid crystalline phases are depending on the systems temperature, hence, they are defined as thermotropic (see Figure 2.1). The melting and clearing point define the temperature range in which the mesophase is thermodynamically stable and both transitions are of first order, exhibiting a latent heat as well as a discontinuous change in density [Kum00]. In contrast, lyotropic liquid crystals exist between the solid state and its isotropic solution, where the amount of solvent is the most important parameter [Ste04].

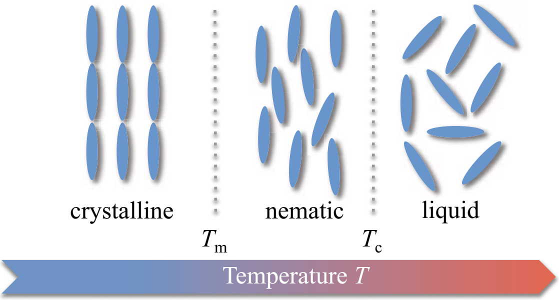

Figure 2.1: Schematic of the different phase states of thermotropic liquid crystal. At the melting point T_m the crystalline material becomes nematic, while at the clearing point T_c the mixture becomes an isotropic liquid. In contrast to non-ideally single crystalline and isotropic phase, the nematic phase shows a certain anisotropy, resulting in specific range of possible effective permittivity values.

There are two major types of thermotropic liquid crystals, being the discotic and calamitic liquid crystals. While discotic liquid crystal molecules have a disk-like shape as well as the tendency to form columns, calamitic liquid crystal molecules have a rod-like shape and tend to align in distinctive layers. The structure of calamitic smectic (from the greek word *σμῆγμα* - soap) liquid crystals come closest to a crystalline structure. There, molecules are organizing in layers with a one-dimensional translational periodicity and orientational order. Calamitic nematic (from the greek word *νῆμα* - thread) liquid crystals on the other hand lack of translational periodicity, not forming any layers, which is the reason for having a higher disorder than smectic liquid crystals. Thus, nematic phases usually occur at higher temperatures [New05].

2.1 Nematic Liquid Crystal

The main properties of nematic liquid crystals can be summarised as follow [Yan+06]:

- The molecules' long axes tend to align parallel to each other. Therefore, the main direction of the molecules inside a unit volume element can be described with the help of the director $\vec{n}$, a macroscopic unit vector. Hence, the material's phase is uniaxial with an rotational symmetry around the director.

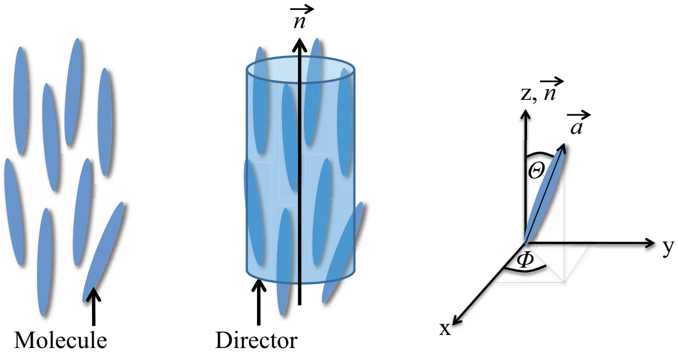

Figure 2.2: Schematic of (left) a unit volume element of liquid crystal molecules, (middle) a unit volume element of liquid crystal molecules including their director $\vec{n}$ and (right) the orientation $\vec{a}$ of a liquid crystal molecule, where the director $\vec{n}$ is showing in z-direction.

- The molecules' centres of mass do not show a long-range correlation, being the reason for the fluid character of nematic liquid crystals.
- Despite the fact that the molecules exhibit a certain polarity, it does not lead to a macroscopic effect. The uniaxial phase has no polarity ($\vec{n} = -\vec{n}$).

For nematic liquid crystal, the orientation of a single molecule is described by the vector $\vec{a}$, whose direction compared to the director is specified by the polar as well as azimuthal angles Θ and Φ (see Figure 2.2). The orientation of $\vec{a}$, and therefore, of the molecule, can be described by an orientational distribution function $f(\Theta, \Phi)$, where $f(\Theta, \Phi) \sin \Theta d\Theta d\Phi$ is the probability of the molecule being oriented within $\Theta + d\Theta$ and $\Phi + d\Phi$ [Yan+06]. The average value N of molecules being oriented in a certain direction is therefore given by

$$\langle N \rangle = \int_0^{2\pi} \int_0^{\pi} f(\Theta, \Phi) \sin \Theta d\Theta d\Phi \ . \tag{2.1}$$

Since liquid crystals are uniaxial, there is no preferred orientation along one of the two short axes and thus $f(\Theta, \Phi) = f(\Theta)$ [Col+97]. The distribution function will have its maximum around $\Theta = 0$ and $\Theta = \pi$ (parallel to the director), while a minimum is expected for $\Theta = \pi/2$ (perpendicular to the director). In a first step, an order parameter needs to be defined, which should be zero in the unordered and non-zero in the ordered phase. By this, the orientational order can be quantitatively specified. Considering the component $a_z = \cos\Theta$ of the molecule as the first-order Legendre polynomial (see Figure 2.2), the average value along the director is

$$\langle a_z \rangle = \langle \cos\Theta \rangle = \frac{\int\limits_0^\pi \cos\Theta f(\Theta) \sin\Theta d\Theta}{\int\limits_0^\pi f(\Theta) \sin\Theta d\Theta} . \tag{2.2}$$

Due to the fact that the molecules are randomly oriented in an isotropic phase and that, for a nematic phase, the probability is the same for molecules to be oriented at angles Θ or $\pi - \Theta$, equation (2.2) cannot provide information about the orientational order, since for both phases $\langle \cos\Theta \rangle = 0$. Therefore, the second-order Legendre-polynomial is used to define the order parameter as [Yan+06]

$$S = \langle P_2(\cos\Theta) \rangle = \left\langle \frac{1}{2}(3\cos^2\Theta - 1) \right\rangle = \frac{\int\limits_0^\pi \frac{1}{2}(3\cos^2\Theta - 1) f(\Theta) \sin\Theta d\Theta}{\int\limits_0^\pi f(\Theta) \sin\Theta d\Theta} . \tag{2.3}$$

While the order parameter for ideally aligned molecules in the direction of the director ($\Theta = 0$) will be $S = 1$, it will be $S = 0$ for an isotropic liquid without any preferred orientation ($f(\Theta) = \text{const.}$). Also, negative order parameter values are possible, even down to $S = -0.5$, which would correspond to molecules, being aligned in a plane perpendicularly to the director ($\Theta = \pi/2$), but at the same time randomly oriented to each other [Yan+06]. However, such kind of order parameters have not been discovered up to now.

To be able to describe the intermolecular interactions of a nematic liquid crystal, Maier and Saupe introduced a molecular-statistical theory in 1959/1960 [Yan+06]. They defined a single molecule potential

$$V(\Theta) = -\nu S \left(\frac{3}{2}\cos^2(\Theta) - \frac{1}{2} \right) , \tag{2.4}$$

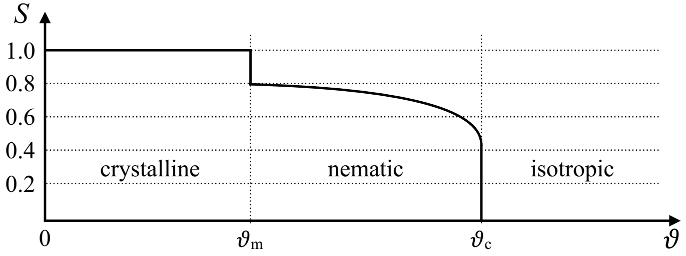

Figure 2.3: Schematic of the order parameter S as a function of the normalised temperature ϑ. The non-continuous jumps at the melting and clearing point are due to the phase transition of first order. In the nematic phase, the order parameter is varying between $0.8 \geq S \geq 0.4$ [Gae15; Col+97].

which is the potential being effective on each molecule in a mean field approximation. There, ν is the orientational interaction constant with values in the range of 1 eV. The potential has a minimum if all the molecules are aligned parallel to the director, its strength is proportional to the order parameter S and it is taking into account, that the orientation antiparallel to the director is the same as parallel to it. With the help of the orientational distribution function

$$f(\Theta) = \frac{e^{-V(\Theta)/k_B T}}{Z} = \frac{e^{-V(\Theta)/k_B T}}{\int\limits_0^\pi e^{-V(\Theta)/k_B T} \sin \Theta d\Theta} , \tag{2.5}$$

with Z being the molecule partition function, the order parameter can be calculated by

$$S = \frac{1}{Z} \int\limits_0^\pi P_2(\cos\Theta) e^{\nu S P_2(\Theta)/k_B T} \sin\Theta d\Theta \, . \tag{2.6}$$

From this formula, S can be calculated numerically for a given value of the normalised temperature $\vartheta = k_B T/\nu$. According to [Yan+06], three solutions are possible, why the corresponding free energies need to be examined. Above the clearing temperature ($\vartheta = \vartheta_c \approx 0.2$) , the free energy of the isotropic phase ($S = 0$) must be lower, while below this temperature, the nematic phase has the lower free energy.

A schematic of the order parameter as a function of the normalised temperature is given in Figure 2.3. While the order parameter of the crystalline phase is given by $S = 1$, it non-continuously drops to around 0.8 at the melting point ($\vartheta_\mathrm{m} \approx 0.1$), due to the first order phase transition. In the nematic phase it is in between 0.4 to 0.8 [Gae15; Col+97], before dropping down to $S = 0$ at the clearing point. However, the Maier-Saupe theory provides only a qualitative description. The quantitative behaviour of the order parameter as a function of the normalised temperature is better described by the empirical formula [Yan+06]

$$S = \left(1 - \frac{0.98\vartheta}{\vartheta_\mathrm{c}}\right)^{0.22} . \tag{2.7}$$

Due to their elongated molecule shape, liquid crystals exhibit a certain anisotropy in magnetic susceptibility as well as permittivity, when being influenced by an external magnetic or electric field, respectively. Hence, the effect of magnetic and electric fields on liquid crystal will be discussed in the following.

2.2 Magnetic Properties

The first anisotropic property of nematic liquid crystals to be discussed is the magnetic susceptibility. Through a magnetic field $\vec{H}$, weak magnetic dipole moments are acting on the molecular orientation, inducing a magnetisation $\vec{M}$ [Ste04]. It can be defined by the magnetic field $\vec{H}$ and the magnetic induction $\vec{B}$ by

$$\vec{M} = \frac{\vec{B}}{\mu_0} - \vec{H} , \tag{2.8}$$

with μ_0 being the magnetic constant. Using $\vec{B} = \mu\vec{H}$ and dividing this equation by $\vec{B}/\mu_0$, where the magnetic permeability μ is the product of the magnetic constant and the relative permeability $\mu = \mu_0\mu_r$, leads to the definition of the dimensionless magnetic susceptibility

$$\chi_\mathrm{m} = \mu_r - 1 = \mu\frac{\vec{M}}{\vec{B}} . \tag{2.9}$$

To describe the magnetisation induced in a nematic phase, this expression needs to be generalised to

$$M_\nu = \frac{1}{\mu} \chi_{\mathrm{m}_{\nu\omega}} B_\omega, \quad \nu, \omega = x, y, z \, . \tag{2.10}$$

Assuming the molecule/director to be pointing in z-direction, the elements $\chi_{\nu\omega}$ of the tensor are given by

$$\boldsymbol{\chi}_{\mathrm{m}} = \begin{pmatrix} \chi_{\mathrm{m}\perp} & 0 & 0 \\ 0 & \chi_{\mathrm{m}\perp} & 0 \\ 0 & 0 & \chi_{\mathrm{m}\parallel} \end{pmatrix} \, . \tag{2.11}$$

There, $\chi_{\mathrm{m}\parallel}$ and $\chi_{\mathrm{m}\perp}$ correspond to the magnetic susceptibility when the field is parallel and perpendicular to the director. This leads directly to the definition of the magnetic anisotropy

$$\Delta\chi_{\mathrm{m}} = \chi_{\mathrm{m}\parallel} - \chi_{\mathrm{m}\perp} = \mu_\parallel - \mu_\perp \, . \tag{2.12}$$

Both susceptibilities $\chi_{\mathrm{m}\parallel}$ and $\chi_{\mathrm{m}\perp}$ are of the order of 10^{-6} to 10^{-5}, resulting in a magnetic anisotropy of nematic liquid crystals of the order of 10^{-6}, which is generally positive ($\Delta\chi_{\mathrm{m}} > 0$). Therefore, the director tends to align parallel to the magnetic field. If the magnetic anisotropy has negative values, as reported for the liquid crystal 7CCH with $\Delta\chi_{\mathrm{m}} = -4.05 \cdot 10^{-7}$, the director will align perpendicularly to the magnetic field [Ste04].

This effect can also be described by the magnetic energy density

$$f_{\mathrm{mag}} = -\frac{1}{2} \vec{B} \cdot \vec{H} = -\frac{1}{2} \mu_0 \mu_\perp H^2 - \frac{1}{2} \mu_0 \Delta\chi_{\mathrm{m}} (\vec{n} \cdot \vec{H})^2 \, , \tag{2.13}$$

where $H = |\vec{H}|$ and only the last term is depending on the director's orientation [Ste04]. For minimisation of the magnetic energy, $\vec{n}$ and $\vec{H}$ need to be parallel to each other if $\Delta\chi_{\mathrm{m}} > 0$, and perpendicular if $\Delta\chi_{\mathrm{m}} < 0$.

Due to the small values of the susceptibility, the relative permeability $\mu_r = 1 + \chi_{\mathrm{m}}$ shows values close to unity. Therefore, the diamagnetic moments of the molecules are small, making the interaction between the molecules negligible. Hence, the externally applied field working on the molecules is not disturbed by interactions between the molecules.

2.3 Dielectric Properties

The second anisotropic property to be discussed is the dielectric permittivity. When applying an electric field to the liquid crystal, an electric dipole moment, and therefore, polarisation $\vec{P}$ is induced, similar to the magnetic case. If the director is oriented in z-direction, the polarisation can be described as

$$\vec{P} = \varepsilon_0 \boldsymbol{\chi}_{\mathrm{e}} \vec{E} \, , \tag{2.14}$$

with $\boldsymbol{\chi}_{\mathrm{e}}$ being the electric susceptibility [Ste04]

$$\boldsymbol{\chi}_{\mathrm{e}} = \begin{pmatrix} \chi_{\mathrm{e}\perp} & 0 & 0 \\ 0 & \chi_{\mathrm{e}\perp} & 0 \\ 0 & 0 & \chi_{\mathrm{e}\parallel} \end{pmatrix} . \tag{2.15}$$

$\chi_{\mathrm{e}\parallel}$ and $\chi_{\mathrm{e}\perp}$ correspond to the susceptibilities parallel and perpendicular to the director. Comparable with (2.10), the polarisation can be written in the general expression

$$P_\nu = \varepsilon_0 \chi_{\mathrm{e}\nu\omega} E_\omega, \quad \nu, \omega = x, y, z \, . \tag{2.16}$$

By making use of the dielectric tensor

$$\boldsymbol{\varepsilon} = \mathbb{1} + \boldsymbol{\chi}_{\mathrm{e}} = \begin{pmatrix} \varepsilon_\perp & 0 & 0 \\ 0 & \varepsilon_\perp & 0 \\ 0 & 0 & \varepsilon_\parallel \end{pmatrix} , \tag{2.17}$$

with $\mathbb{1}$ being the identity matrix, the dielectric displacement can be written as

$$\vec{D} = \varepsilon_0 \vec{E} + \vec{P} = \varepsilon_0 \boldsymbol{\varepsilon} \vec{E} \, . \tag{2.18}$$

While the parallel and perpendicular dielectric permittivities are defined as $\varepsilon_\parallel = 1 + \chi_{\mathrm{e}\parallel}$ and $\varepsilon_\perp = 1 + \chi_{\mathrm{e}\perp}$, the dielectric anisotropy is given by $\Delta\varepsilon = \varepsilon_\parallel - \varepsilon_\perp$. With this, the dielectric displacement is [Ste04; Gen+95]

$$\vec{D} = \varepsilon_0 \varepsilon_\perp \vec{E} + \varepsilon_0 \Delta\varepsilon (\vec{n} \cdot \vec{E}) \vec{n} \, . \tag{2.19}$$

Together with the definition of the electrical energy density

$$f_{\mathrm{el}} = -\frac{1}{2}\vec{D}\cdot\vec{E} = -\frac{1}{2}\varepsilon_0\varepsilon_\perp\vec{E}^2 - \frac{1}{2}\varepsilon_0\Delta\varepsilon(\vec{n}\cdot\vec{E})^2\,, \tag{2.20}$$

it can be seen that for positive dielectric anisotropies the directors tend to align parallel, while for negative dielectric anisotropies they tend to align perpendicularly to the electric field [Gen+95]. Typical values for microwave-optimised liquid crystal mixtures used in this work are between $0.7 < \Delta\varepsilon < 0.9$, thus, aligning parallel to the electric field lines. However, also *dual-frequency* LCs can be used in microwave applications. The dielectric anisotropy of this particular type of LC can be changed from positive to negative values and vice versa just by varying the frequency of its biasing fields [Kuk+02].

2.4 Biasing Schemes

Up to now, only ideal single crystals have been considered, i.e. the molecules are aligned along a common direction. In practical applications curvatures are often observed, for example when an external field is working against the force induced by surface anchoring of the molecules. Assuming small spatial variations of $\vec{n}$, the LC still is uniaxial with a variable preferred direction $\vec{n}(\vec{r})$ and a fixed order parameter $S(T)$. The overall order parameter of the complete LC volume is then described by a tensor [Gen+95]

$$Q_{\alpha\beta} = S(T)\left[n_\alpha(\vec{r})n_\beta(\vec{r}) - \frac{1}{3}\delta_{\alpha\beta}\right]\,, \tag{2.21}$$

with $\alpha, \beta = x, y, z$ and $\delta_{\alpha\beta}$ being the Kronecker delta

$$\delta_{\alpha\beta} = \begin{cases} 1\,, & \text{if} \quad \alpha = \beta \\ 0\,, & \text{if} \quad \alpha \neq \beta \end{cases}\,. \tag{2.22}$$

Significant variations usually occur in the range of µm while the molecular dimensions are in the range of nm. This is why curvatures can be described by the continuum theory of Frank and Oseen, being analogue to the classical elastic theory of a solid [Gen+95; Fra58; Ste04].

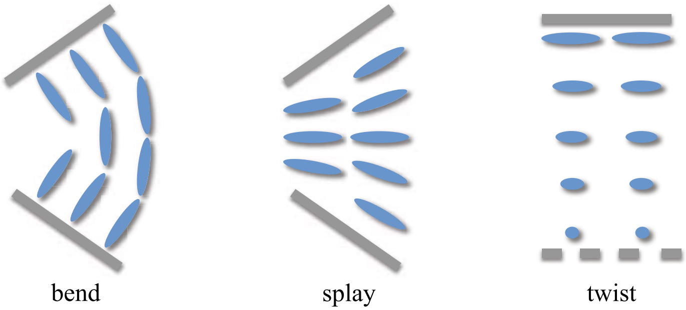

Figure 2.4: Two-dimensional schematics of the bend, splay and twist reorientation. Each of these reorientations contributes to the elastic energy and has its specific elastic constant K_{11} (splay), K_{22} (twist) and K_{33} (bend).

The free energy stored in a bulk of LC molecules is a function of its dielectric and elastic constants. In contrast to an uniform LC alignment, where the Gibbs free energy is minimised, energy needs to be applied to the system in order to cause locally effective torques, and therefore, curvatures. This kind of energy can be applied in different ways, e.g. by applying an electric or magnetic field, or by changing the volumes boundaries, i.e. the cavity walls of the LC volume. Then, the system will minimise its energy, resulting in three possible types of reorientations, the *bend*, *splay* and *twist* reorientation, shown in Fig. 2.4.

The contributions of these deformations to the energy of the system is described by the free energy density for nematics [Ste04]

$$\begin{aligned} f_{\text{elast.}} &= f_{\text{splay}} + f_{\text{twist}} + f_{\text{bend}} && (2.23)\\ &= \frac{1}{2}K_{11}(\vec{\nabla}\cdot\vec{n})^2 + \frac{1}{2}K_{22}(\vec{n}\cdot\vec{\nabla}\times\vec{n})^2 + \frac{1}{2}K_{33}(\vec{n}\times\vec{\nabla}\times\vec{n})^2\,. && (2.24)\end{aligned}$$

The quantities K_{ii} (i = 1, 2, 3) are often referred to as Frank elastic constants, being material-, temperature-, and therefore, order parameter dependent values. Further, surface terms need to be taken into account if the LC volume is small compared to its surface [Gae15]

$$f_{\text{surf.}} = -\frac{1}{2}K_{24}(\vec{\nabla}\cdot((\vec{\nabla}\cdot\vec{n})\vec{n} + \vec{n}\times\vec{\nabla}\times\vec{n}))\,, \tag{2.25}$$

with K_{24} being the *saddle-splay* constant.

Together with the contributions for the magnetic and electric field from (2.13) and (2.20), respectively, the total free energy of the system can be calculated by

$$F = \iiint_V \left(f_{\text{elast.}} + f_{\text{surf.}} + \underbrace{f_{\text{field}}}_{f_{\text{mag}}+f_{\text{el}}} \right) dV \, . \tag{2.26}$$

Since the systems free energy is always striving to a minimum, the LC molecules tend to align parallel to the field lines for an LC with positive dielectric anisotropy.

If one of the contributions changes, torques become effective until the torque-balance-equation

$$\Gamma_{\text{field}} + \Gamma_{\text{elast.}} + \Gamma_{\text{diss.}} = 0 \tag{2.27}$$

is met again, where $\Gamma_{\text{diss.}}$ is the dissipative torque. It originates from the internal friction, which occurs due to a movement of the director towards the minimum energy level, caused by an imbalance of the electrical and elastic torques. The resulting momentum counteracts the movement of the LC and its magnitude depends on the rotational viscosity γ_{rot}.

The orientation of LC can be controlled in three different ways:

- **surface anchoring**: a polyimide film is spin coated on the carrier substrate and mechanically rubbed in a preferred direction using a velvet cloth, as shown in Fig. 2.5. By this, grooves are produced on the surface to which LC molecules next to this surface will align parallel. Therefore, it is often referred to as

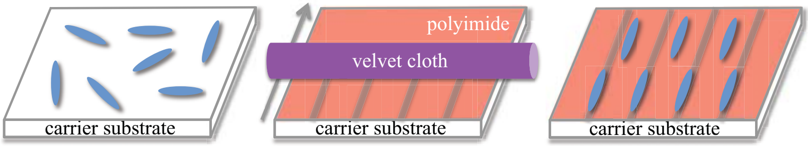

Figure 2.5: Schematic of the alignment layer fabrication process. The polyimide film is spin coated to the substrate and rubbed in a preferred direction using a velvet cloth. By this, very small grooves are applied to the polyimide layer. The LC molecules are orienting parallel to their direction.

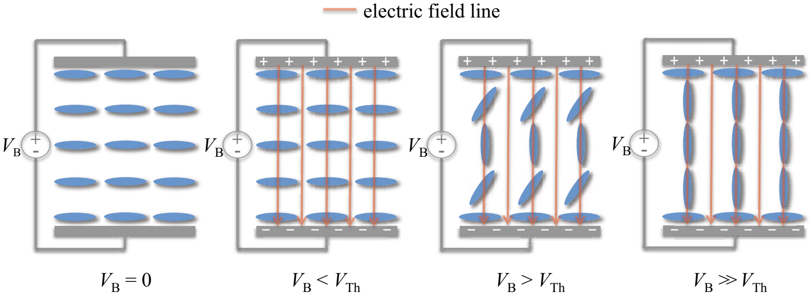

Figure 2.6: Schematic of a rudimentary electric biasing system, where a parallel plate capacitor is filled with LC. The threshold voltage V_{Th} needs to be exceeded before the LC molecules start aligning parallel to the field lines.

alignment layer. Due to the tendency of the LC molecules to align parallel to each other, the complete volume will align parallel to the grooves.

- **electric biasing**: assuming a parallel plate capacitor filled with LC, as shown in Fig. 2.6. A biasing voltage V_{B} can be introduced to the capacitor, generating an electric biasing field inside. Before an alignment of the LC is possible, the threshold voltage V_{Th}, also known as the *Freedericksz threshold*, needs to be exceeded [Ste04]. It defines the voltage where the electric and elastic forces of the surface anchoring are in an equilibrium. If the voltage is further increased, the electric torques are exceeding the elastic ones and LC is aligning parallel to the field lines.
- **magnetic biasing**: similar to the electrical biasing, two rare earth magnets are placed as parallel plates around the LC cavity, by which the directors will align parallel to the magnetic field lines. This biasing method is only used in the lab for a fast first proof-of-concept. For practical applications it is not reasonable, since the reorientation of the magnets would require a mechanical adjustment. Alternatively, electromagnets can be used with the expense of a high power consumption.

For the realisation of tuneable microwave components, LC is integrated into the transmission line or waveguide or even into the antenna element itself. In contrast to optical applications, where the polarisation of light is rotated by LC, the orientation of LC within microwave components is always changed with respect to the applied radio frequency (RF) field. A change of the LC orientation results in a variation of

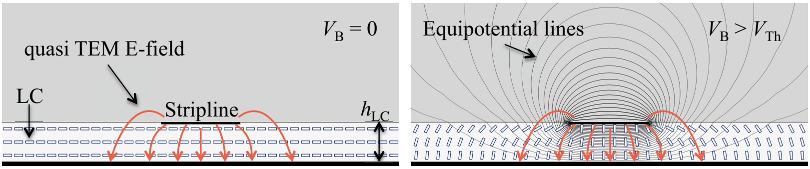

Figure 2.7: Schematic of the hybrid biasing scheme using the example of an LC filled microstrip line. The alignment layer is orienting the LC by default perpendicularly until a biasing voltage V_B is applied to the transmission line, aligning the LC ideally parallel to the RF-field, coinciding the biasing field.

the effective permittivity as well as dielectric loss. All possible orientations between the two extreme cases of perpendicular ($\varepsilon_{r,\perp}$ and $\tan\delta_\perp$) and parallel ($\varepsilon_{r,\parallel}$ and $\tan\delta_\parallel$) to the RF-field can be continuously adjusted, see also Fig. 2.7 and Fig. 2.8. Thus, a variable delay line can be realised by the implementation of LC, where the electrical length of the line can be varied just by tuning the LC's orientation.

For practical application two different biasing schemes are used:

- **hybrid scheme**: for planar devices as introduced in [Kar14], a mixture of surface anchoring and electric biasing is chosen. Since the LC layer heights are comparatively small ($h_{LC} \leq 100\,\mu m$), an alignment layer as mentioned above is used to orient the LC perpendicularly to the RF field in the unbiased state. By applying a biasing voltage V_B to the transmission line, the LC starts to align parallel to the RF- field (see Fig. 2.7). If the voltage is switched off again, the LC is reorienting.
- **fully electric scheme**: in metallic waveguide devices as presented in [Gae15], a pure electric biasing network is needed, since the use of an alignment layer is inappropriate for LC layer heights of several mm. There, several pairs of electrodes are included inside the metallic waveguide to provide a quadrupole biasing field for tuning (see Fig. 2.8). By varying the biasing voltages, the biasing field can be changed both in orientation and field strength.

While the hybrid biasing scheme is well-known from the display technology, the fully electric biasing scheme has been investigated especially for high-performance microwave application [Gae15]. This has its origin in the fact, that the response time of LC devices would be much too long when an alignment layer is used in a metallic waveguide component. In the following, the response time will be defined according to the example of the LC filled microstrip line of Fig. 2.7 [Ste04].

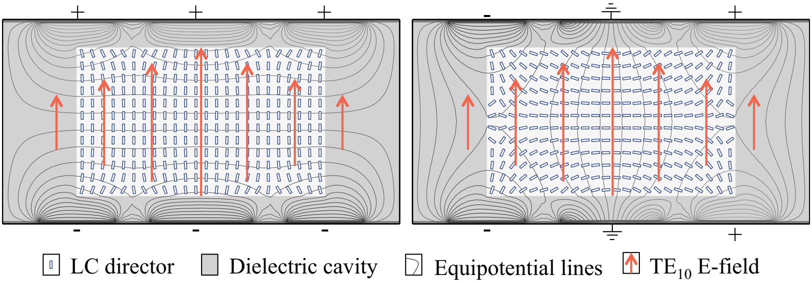

Figure 2.8: Schematic of the electric biasing scheme using the example of an LC filled metallic waveguide. There, several pairs of electrodes are included inside the waveguide to provide a quadrupole biasing field for tuning.

Let us assume the case of an ideally pre-orientated LC. The time, which is needed to align the LC directors parallel to the RF field after the biasing voltage ($V_\mathrm{B} > V_\mathrm{Th}$) is switched on, is called the *switch-on response time*

$$\tau_\mathrm{on} = \frac{\gamma_\mathrm{rot}}{\varepsilon_0 \Delta\varepsilon (E^2 - E_\mathrm{Th}^2)} \quad , \qquad E_\mathrm{Th} = \frac{\pi}{h_\mathrm{LC}} \sqrt{\frac{K_{ii}}{\varepsilon_0 \Delta\varepsilon}} \tag{2.28}$$

$$= \frac{\gamma_\mathrm{rot}\, h_\mathrm{LC}^2}{K_{ii} \pi^2 (V_\mathrm{B}^2 / V_\mathrm{Th}^2 - 1)} \; . \tag{2.29}$$

It is mainly dependent on the rotational viscosity γ_rot, the LC layer height h_LC, the biasing voltage V_B as well as the corresponding Frank elastic constant. If V_B is increased, the switch-on response time is decreasing. When the biasing voltage is switched off again, the LC starts to reorient comparatively fast, based on the degree of deformation. The restoring force, and thus, the re-aligning speed slows down steadily with decreasing elastic deformations until the perpendicular pre-orientation is almost reached again. The so-called *switch-off response time* is defined as [Ste04]

$$\tau_\mathrm{off} = \frac{\gamma_\mathrm{r}\, h_\mathrm{LC}^2}{K_{ii} \pi^2} \; . \tag{2.30}$$

Since it is only depending on the LC layer height h_{LC}, this orientation mechanism needs longer than the electric biasing scheme, especially for LC volumes with heights in the range of mm. Hence, in high-performance metallic waveguide components based on LC, this re-alignment would take much too long, which is why the fully electric biasing scheme is used.

For estimating the response times, not only the rotational viscosity of the material system is needed, but also the anisotropy $\Delta\varepsilon$ for low frequencies in the kHz range [Gae15]. Further, the design of continuously tuneable components based on LC requires a knowledge of the dielectric properties of the material.

2.5 Micro- and Millimetre Wave Characterisation

The dielectric properties of LC can be determined, either by using a broadband transmission line-based characterisation setup or by using a precise resonator-based setup, making use of the cavity perturbation technique [Pen+04; Mue07; Kar14; Gae15]. There, a resonator is measured with and without LC inside a sample holder made of silica. The dielectric properties of LC will cause a shift of the resonant frequency compared to the measurement carried out with an empty sample holder. While this kind of measurement is limited to a single frequency, the dielectric properties and especially the dielectric loss can be determined much more precise than with broadband measurement setups.

A dual-mode cylindrical resonator has been designed in [Gae15], with which the permittivity and dielectric loss of LC can be measured for both parallel and perpendicular orientation in one single step. A schematic of the resonator including the used RF modes is shown in Fig. 2.9.

The silica tube is placed in the centre of the resonator. The excitation is provided through a coupling hole just above the bottom plate of the resonator, being fed by a rectangular metallic waveguide. Two different modes are evaluated, each of them having an electric field distribution only parallel or perpendicular to the long axis of the silica tube. During the characterisation, the LC's long axes are aligned parallel to the silica tube by means of permanent magnets. Measurements with an empty and an LC filled tube are compared and evaluated. Due to the dielectric properties of LC, the field distribution, and therefore, the resonance frequency of the excited mode will shift compared to the reference measurement. A more detailed and mathematical description of this method can be found in [Gae15].

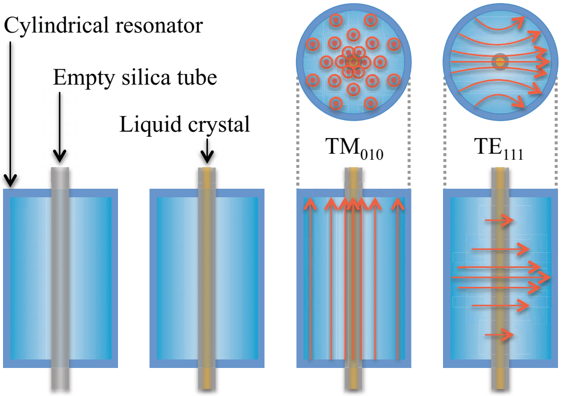

Figure 2.9: Schematic of the resonator based LC characterisation setup of [Gae15]. Two orthogonal RF modes are excited in the resonator at the same time, allowing the determination of the dielectric properties for both extreme LC orientations in a single measurement.

By providing this characterisation method, the LC mixtures could be improved for the micro- and millimetre wave range in cooperation with Merck KGaA, Darmstadt. To be able to compare different LC mixtures, two important quantities have been defined. The *material tuneability*

$$\tau_{\mathrm{LC}} = \frac{\varepsilon_{\mathrm{r},\parallel} - \varepsilon_{\mathrm{r},\perp}}{\varepsilon_{\mathrm{r},\parallel}} = \frac{\Delta\varepsilon_{\mathrm{r}}}{\varepsilon_{\mathrm{r},\parallel}} \tag{2.31}$$

quantifies the relative anisotropy of the mixture. If it is divided by the maximum dielectric loss $\tan\delta_{\max}$, the *material quality factor*

$$\eta_{\mathrm{LC}} = \frac{\tau_{\mathrm{LC}}}{\tan\delta_{\max}} \tag{2.32}$$

is achieved. A comparison of different LCs, measured at 19 GHz and room temperature, is shown in Fig. 2.10.

Where the first tuneable microwave devices in the early 2000's were realised using display LCs, new mixtures were specifically synthesised for the microwave range.

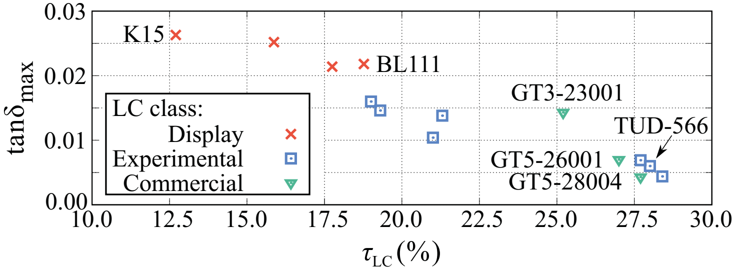

Figure 2.10: Comparison of different LC mixtures, regarding their material tuneability and dielectric loss. The measurements of these material parameters have been carried out at 19 GHz and room temperature using the resonator-based measurement setup from [Gae15; Fri+17].

Table 2.1: Dielectric properties of different LC mixtures measured at room temperature and 19 GHz (source: Merck KGaA)

Mixture	$\varepsilon_{r,\parallel}$	$\tan\delta_{\parallel}$	$\varepsilon_{r,\perp}$	$\tan\delta_{\perp}$	$\tau_{\mathrm{LC}}(\%)$	η_{LC}	$\Delta\varepsilon$ at 1 kHz
GT3-23001	3.28	$3.8 \cdot 10^{-3}$	2.46	$1.4 \cdot 10^{-2}$	25.2	17.6	4.6
GT5-26001	3.27	$2.2 \cdot 10^{-3}$	2.39	$7.0 \cdot 10^{-3}$	27.0	38.3	1.0

The values for $\tan\delta$ were reduced by more than a factor of 4 from K15 to TUD-566. Further, the tuneability has been doubled. With the GT-series, Merck launched the first commercial microwave LC mixtures. The material properties of the mixtures used in this work are given in Table 2.1. Because of their availability in larger quantities, the GT3-23001 mixture was used in chapter 4, while for the components in chapter 5 and 6 the GT5-26001 mixture was chosen.

As one advantage of LC is the decreasing dielectric loss with increasing frequency in the range above 15 GHz, measurements up to 1.5 THz have been conducted using a time-domain spectroscopy (TDS) THz measurement system [Wei+13a]. A detailed description can be found in [Wei17]. With this, LC has been proven as well-suitable material for the realisation of continuously tuneable devices not only in the microwave- but also in the (sub)millimetre wave and THz range. Thus, the devices realised in this work prove the concept in the lower and higher millimetre wave range.

3 Mixed Beam-Switching and Beam-Steering Network

As for many applications in the millimetre wave range, high gain antenna systems are needed to overcome the increasing free-space path loss. This requires not only low-loss feeding networks, but also highly directive antennas or antenna arrays with a large number of single antenna elements. For beam corrections of the pencil beams, but in particular for portable, tracking and on-the-move applications, an adaptive beam-steering is mandatory. An alternative to commonly used mechanically moving parabolic antennas or electronically beam-steering phased array antennas are mixed beam-switching and beam-steering networks based on Butler matrices in combination with tuneable phase shifters, e.g. based on varactor diodes [Cha+10].

3.1 Butler Matrix

The Butler matrix is a beam-switching network, which was invented in 1961 for the simplification of antenna array feeding networks [But+61]. It is an $N \times N$ network with $N = 2^n$ inputs/outputs. It is composed of $(N/2)\log_2 N$ hybrid couplers as well as $(N/2)\log_2(N-1)$ phase shifters [Bal+07].

Within the Butler matrix, the input signal is split equally to all output ports, by which a well-defined phase distribution is achieved. A schematic of the original 4×4 Butler matrix, fed at an outer input port, is given in Fig. 3.1. All 4×4 Butler matrices discussed in this work are equipped with 90° hybrids, generating four beams, which are equally distributed around the broadside direction. By selecting different inputs with an RF switch, the phase distribution changes, resulting in a switching of the beam to predefined directions, as shown in Fig. 3.1. Not only a single beam can be excited by this, but also multiple beams by choosing e.g. two input ports at the same time. The signal of the second input will then form a beam in another direction as for the first input. If a beam in broadside direction is preferred, more

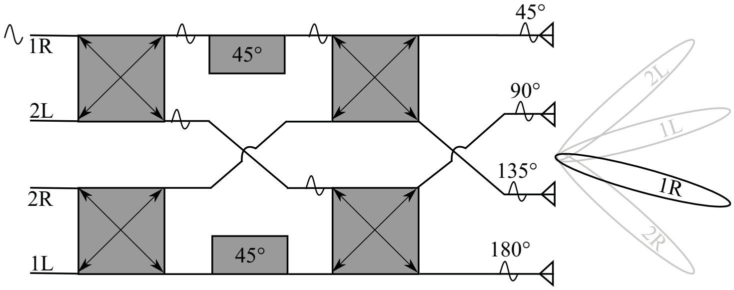

Figure 3.1: Schematic of a 4×4 Butler matrix fed at port 1. It consists of 90° hybrid coupler, fixed 45° phase shifters as well as crossovers.

complex Butler matrix designs are needed, being mostly based on 180° hybrids, e.g. rat-race coupler [Kou+05; Kam+14; Win+15].

The schematic of the Butler matrix is similar to the computational operations of the fast Fourier transformation, and therefore, performing an analogue signal processing [Nes68; She68]. Therefore, the first Butler matrix represented the analogue implementation of the fast Fourier transformation before it was even invented in 1965 [Coo+65].

Similar to the comparison between fast and conventional Fourier transformation, a Butler matrix dramatically reduces the number of required components compared to a conventional divide/combine beam-forming network. While an 8×8 Butler matrix requires 12 hybrid couplers and 8 phase shifters, a conventional beam-forming network would require 112 hybrid couplers and 64 phase shifters for the same functional complexity. Since Butler matrices are system-inherently narrow-banded, efforts were made to increase the bandwidth by designing a broadband hybrid coupler [Bar+06]. Also, the side lobe level, being limited by the uniform excitation of all individual antenna elements to −10 dB [Win+05; Liu+05], was improved by the use of a modified $2^n \times 2^{n+1}$ Butler matrix [Che+09] as well as by the combination of a 4×4 Butler matrix with four 180° directional couplers [Win+06]. However, a disadvantage of the Butler matrix is its discrete phase distribution, only allowing a beam-switching.

The beam-switching Butler matrix of Fig. 3.1 can be extended to a mixed beam-switching and beam-steering network by the implementation of tuneable phase shifters. They can be exemplarily used before the antenna elements to continuously

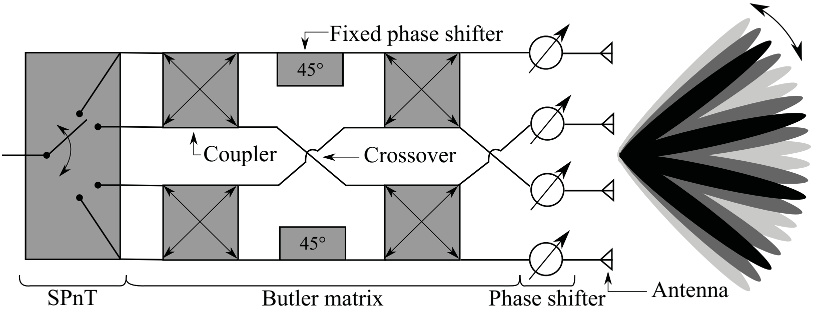

Figure 3.2: Schematics of a continuously tuneable 1×4 beam-steering network based on a 4×4 Butler matrix, a tuneable SPnT as well as tuneable phase shifters in front of each antenna element.

steer the beam in-between the states to which it can be switched by the Butler matrix. Hence, all preferred beam directions can be adjusted by this mixed beam-switching and beam-steering concept. Since the progressive phase shift between two adjacent beams is 90°, an additional progressive phase shift of ±45° is needed to steer the beam in any direction in between those adjacent switched beam positions. Therefore, an additional phase shift of only 135° is required of the tuneable phase shifters, in contrast to the phased array approach, where 360°, and therefore, larger phase shifters with higher losses are required. Further, tuneable SPnTs with continuously tuneable power splitting ratio can be used for the input selection, allowing a multiple port selection, and therefore, multiple beam excitation. A schematic of such a tuneable 1×4 beam-steering network is given in Fig. 3.2.

3.2 Tuneable Phase Shifter

A key component for many tuneable devices is the tuneable phase shifter. To change the phase of an RF signal at low frequencies, parts of reactances are used, occurring at inductances and capacitances, while delay lines are most common at high frequencies. Therefore, most phase shifters can be grouped in two categories:

- **True phase shifters** (frequency independent): the spectrum is shifted uniformly by 90° using so-called Hilbert transformer [Sch+98].

- **True delay line** (frequency dependent): a certain phase shift can be achieved by delaying a signal. Due to the different periodic times at different frequencies, this kind of phase shifting is frequency dependent.

In addition, there are special types of phase shifters not fitting in one of these definitions, e.g. the capacitively tuned reflection-type phase shifter, whose phase does not change linearly with frequency [Isk+16].

The first generation were mechanical phase shifters, meeting all phase shifting requirements until the 1960s [Fox47; Sta57; Han66]. The first electrically controlled ferrite phase shifter was introduced in 1957 by Reggia and Spencer [Reg+57], followed by semiconductor diode phase shifters [Whi65; Whi68] and many more.

True delay lines can be divided in two classes: *active* and *passive*. While the active class uses external sources for amplification [Vor+82], the passive class only relies on the power being available from the AC, without any amplification. Semiconductor phase shifters can be implemented in both, active and passive architectures. They are dominated by monolithic microwave integrated circuits (MMICs) and radio frequency integrated circuits (RFICs) [Che+13; Kan+09]. In comparison to *analogue* phase shifters, which provide a continuously varying phase, semiconductor phase shifters are mainly *digital* phase shifters, providing a discrete set of phase states. A 360° 3-bit phase shifter, for example, has a 45°-, 90°- and 180°-element, which allow discrete steps with a step size of 45° [Kou91]. Varactor diodes are an exception as they can continuously vary their phase.

The passive class is based for example on microelectromechanical systems (MEMS) [Bar+98], ferrites [Kou91], ferroelectrics, such as barium-strontium-titanate (BST) [Vel+07; Saz+11b], and LCs. Where MEMS are mainly providing discrete phase steps, ferrites show a high power consumption. BST and LC are promising alternatives for the realisation of tuneable phase shifters, due to their continuous tuneability and low power consumption. Since BST phase shifters are fully printable these days [Nik+14] and LC devices can utilise automated manufacturing techniques similar to LC display technology [Kar14], they are enabling a low-cost fabrication of larger arrays even for a low-volume production. The increasing dielectric loss with increasing frequency limits the application of BST devices to frequencies below 30 GHz [Saz+11a; Pao+14]. In contrast, LCs are ideally suited for applications above 10 GHz, since their dielectric losses decrease with increasing frequency up to a certain point, from which they stay constant even up to the THz regime [Wei+13a]. Phase shifters based on LC are used as true delay lines, where its effective permittivity, and therefore, the electrical length of the phase shifter is varied, while the physical length is staying constant.

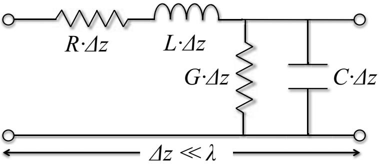

Figure 3.3: Schematic of the a quasi-TEM transmission line.

The basic principle of an LC filled phase shifter will be explained by means of the quasi-TEM transmission line section in Fig. 3.3. The tuneable material generally influences all transmission line elements R, L, G and C. Their dependency on the relative permittivity of the material is linked to the transmission line topology. Therefore,

$$R = \frac{1}{A_{\text{eff}}\,\sigma}\,, \qquad L = \sqrt{\mu}\,\frac{Z_0}{c_0}\,, \tag{3.1}$$

$$G = \omega C \tan\delta_{\text{eff}}\,, \qquad C = \frac{\sqrt{\varepsilon_{\text{r,eff}}}}{Z_0 c_0}\,, \tag{3.2}$$

with the conductor cross section A_{eff}, the metal's electrical conductivity σ and $\varepsilon_{\text{r,eff}}$ and $\tan\delta_{\text{eff}}$ being the dielectric's effective permittivity and loss, respectively. By calculating the complex propagation constant

$$\gamma = \alpha + i\beta = \sqrt{(R + i\omega L)(G + i\omega C)} \tag{3.3}$$

the well-known relation for the phase constant of a TEM wave $\beta = \omega\sqrt{\mu\varepsilon}$ ($[\Delta\beta]$ = rad/m) can be derived. The phase shift, which can be provided by the phase shifter, is calculated by means of the phase shifter length l_{PS} as well as the differential phase constant $\Delta\beta = \beta_{\parallel} - \beta_{\perp}$ to

$$\Delta\varphi = \left(\Delta\beta \cdot \frac{180^\circ}{\pi}\right) \cdot l_{\text{PS}} = \left(\frac{360^\circ \cdot f}{c_0}\left(\sqrt{\varepsilon_{\text{r,eff},\parallel}} - \sqrt{\varepsilon_{\text{r,eff},\perp}}\right)\right) l_{\text{PS}}\,, \quad [\Delta\varphi] = {}^\circ\,. \tag{3.4}$$

The indices $\perp$ and $\parallel$ are indicating the different orientations of the LC director with respect to the RF field inside the phase shifter, being described in detail in chapter

2. An important parameter for the evaluation of tuneable transmission lines is the *steering efficiency* τ_φ, being defined as the achievable phase shift per unit length

$$\tau_\varphi = \frac{\Delta\varphi}{l}\,, \quad [\tau_\varphi] = {}^\circ/\mathrm{m}\,. \tag{3.5}$$

It can be normalised to the ideally achievable phase shift for perfect alignment in all orientations. Due to certain boundary conditions inside the transmission line, the LC can never be ideally aligned, which is why the steering efficiency will always be $\tau_\varphi/\tau_{\varphi,ideal} < 1$.

To compare the performance of passive phase shifters, a *figure of merit* (FoM) has been defined as the ratio of the maximum phase shift over the maximum insertion loss (IL) for all tuning states [Kou91]

$$\mathrm{FoM} = \frac{\Delta\varphi_{\mathrm{max}}}{\mathrm{IL}_{\mathrm{max}}}\,, \quad [\mathrm{FoM}] = {}^\circ/\mathrm{dB}\,. \tag{3.6}$$

The anisotropic behaviour of the insertion loss causes different attenuation constants for different alignment states, resulting in a frequency- and alignment-dependent loss IL(f, φ). A comparison of different tuneable phase shifter technologies for K_a-, V- and W-band frequencies is given in Table 3.1.

As can be seen, LC phase shifters can be designed in different technologies, depending on the application for which they are intended. For low-loss applications, metallic waveguide based LC phase shifters are of major interest. They benefit from very low losses, and therefore, a high FoM. Hence, they are preferably used for feeding networks in satellite applications. On the other hand, they are not compact enough for an easy integration. For low-profile applications transmission line based LC phase shifters are best suited, such as a coplanar waveguide (CPW) or a microstrip line (MSL) based LC phase shifter, which have been discussed in detail in [Kar14; Gö09].

Liquid crystal based phase shifters have proven several times to be suitable for the integration in electrically steerable phased array antennas [Kar14; Gae15; Str15]. In this work, they are used for the first time in a mixed beam-switching and beam-steering network as well as the continuously adjustable interference-based SPDTs.

3.3 Interference-Based Single-Pole Double-Throw

In the past, research on SPDTs focussed solely on RF switching. The spotlight has been on the selectivity of different paths while, at the same time, ensuring a high isolation to all unselected ports. To fulfil these requirements, semiconductor and MEMS technologies have been most commonly used. With these technologies, compact circuits could be realised, where certain paths can be connected to ground when applying a biasing current or voltage [Kum+12; Sca+02]. By this, a low-loss propagation can be supplied in the thru path, while the isolation to the other ports is high due to the ground connection.

Now, for a higher flexibility in future applications, interference-based LC SPDTs are introducing a novel property: *a continuously adjustable power splitting ratio*.

By the use of continuously tuneable phase shifters, the interference scenarios inside the coupling region of an SPDT can be controlled, by which it is not only possible to switch between the different paths, but also to continuously adjust each preferred power ratio between them. This can be useful e.g. in the aimed mixed beam-switching and beam-steering network for providing a multiple beam generation.

Table 3.1: Comparison of different tuneable phase shifter technologies.

Technology	Implementation	f (GHz)	FoM (°/dB)	REF
InGaAs	PIN switch diodes	28	45	[Yan+11]
GaN	2-bit RTPS	80	17	[Mar+14]
MEMS	distributed MEMS CPW	40	47	[Bar+98]
	loaded line (4-bit)	60	83	[Kim+02]
	Waveguide MEMS	106	13	[Psy+13]
	3-bit switched line	77	55	[Ste+08]
MEMS & CMOS	RTPS (CMOS 0.18 µm)	65	42	[Cha+13]
BST	loaded CPW	40	22	[Vel+07]
LC	microstrip line	24	110	[Wei+03]
	finline	40	62	[Mue+05]
	ridged waveguide	96	70	[Mue+06]
	metallic waveguide	35	200	[Gae+09]
LC & LTCC	SIW	28	41	[Str+14]
LC & MEMS	loaded line	93	42	[Fri+11]
LC & CMOS	CPW (CMOS 0.35 µm)	45	51	[Fra+13]

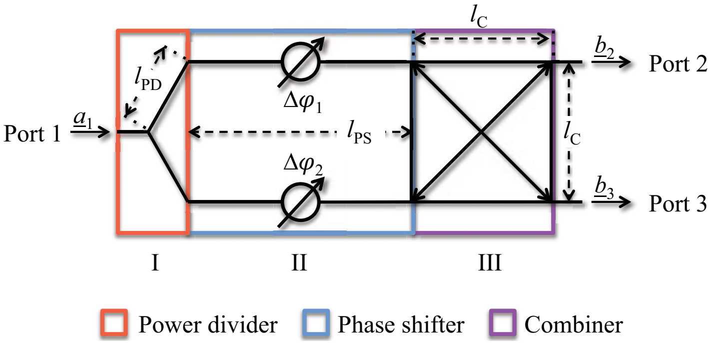

Figure 3.4: Basic principle of an interference-based SPDT equipped with tuneable phase shifters. By varying the phase shift between the two branches, the interference scenarios, and therefore, the output ports can be continuously selected for each preferred signal ratio.The lengths of the power divider branches, the separated paths including the phase shifters as well as the combiner are given by l_{PD}, l_{PS} and l_C, respectively.

Moreover, in a receive path of a radiometer both outputs can be connected to a detector each, one having a high power limit but a low sensitivity and the other having a low power limit but a high sensitivity. While one of them is suitable for continuous high power detection, the other is able to detect already small or single signals. Since the power of the signals can vary over a certain time period, an adaption to the power ratio is needed. One example of such an application is inside an RF radiometer or in satellite applications. There, interference-based SPDTs can also be used for switching to the power calibration path or between transmit and receive paths, respectively. Further advantages of this technology are the low power consumption as well as the fact that no mechanically moving parts are needed, which reduces the possibility of wear-out failures to a minimum.

In the following, the concept of interference-based SPDTs is explained in detail. A schematic of the basic principle is shown in Fig. 3.4.

According to the scattering matrix for an ideal power divider

$$\begin{pmatrix} \underline{b}_1^{\mathrm{I}} \\ \underline{b}_2^{\mathrm{I}} \\ \underline{b}_3^{\mathrm{I}} \end{pmatrix} = \frac{1}{\sqrt{2}} \begin{pmatrix} 0 & 1 & 1 \\ 1 & 0 & 0 \\ 1 & 0 & 0 \end{pmatrix} \begin{pmatrix} \underline{a}_1^{\mathrm{I}} \\ \underline{a}_2^{\mathrm{I}} \\ \underline{a}_3^{\mathrm{I}} \end{pmatrix} , \tag{3.7}$$

the incoming signal $\underline{a}_1 = \underline{a}_1^{\mathrm{I}}$ is split into two equal parts, being in phase to each other.

$$\begin{aligned} \underline{a}_1 &= \frac{1}{2}\underline{a}_1^{\mathrm{I}} + \frac{1}{2}\underline{a}_1^{\mathrm{I}} \qquad (3.8) \\ &= \frac{1}{\sqrt{2}}\underline{b}_2^{\mathrm{I}} e^{-i\beta l_{\mathrm{PD}}} + \frac{1}{\sqrt{2}}\underline{b}_3^{\mathrm{I}} e^{-i\beta l_{\mathrm{PD}}} \qquad (3.9) \end{aligned}$$

Each of the upcoming paths includes a phase shifter for 90° phase shift. Taking this into account as well as the total length of the two branches l_{PS}, this leads to

$$\underline{b}_x^{\mathrm{II}} = \underline{b}_x^{\mathrm{I}} e^{-i\beta l_{\mathrm{PS}}} e^{-i\Delta\varphi_x} , \qquad x = 2, 3 , \tag{3.10}$$

and therefore,

$$\underline{a}_1 = \frac{1}{\sqrt{2}}\underline{b}_2^{\mathrm{II}} e^{-i\beta(l_{\mathrm{PD}}+l_{\mathrm{PS}})} e^{-i\Delta\varphi_1} + \frac{1}{\sqrt{2}}\underline{b}_3^{\mathrm{II}} e^{-i\beta(l_{\mathrm{PD}}+l_{\mathrm{PS}})} e^{-i\Delta\varphi_2} . \tag{3.11}$$

At this point it is assumed that the change in propagation constant within the phase shifter is negligible. The signals are superimposed afterwards in the combiner section, being described by the scattering matrix

$$\begin{pmatrix} \underline{b}_1^{\mathrm{III}} \\ \underline{b}_2^{\mathrm{III}} \\ \underline{b}_3^{\mathrm{III}} \\ \underline{b}_4^{\mathrm{III}} \end{pmatrix} = -\frac{1}{\sqrt{2}} \begin{pmatrix} 0 & i & 1 & 0 \\ i & 0 & 0 & 1 \\ 1 & 0 & 0 & i \\ 0 & 1 & i & 0 \end{pmatrix} \begin{pmatrix} \underline{a}_1^{\mathrm{III}} \\ \underline{a}_2^{\mathrm{III}} \\ \underline{a}_3^{\mathrm{III}} \\ \underline{a}_4^{\mathrm{III}} \end{pmatrix} , \tag{3.12}$$

with $\underline{a}_1^{\mathrm{III}} = \underline{b}_2^{\mathrm{II}}$ and $\underline{a}_4^{\mathrm{III}} = \underline{b}_3^{\mathrm{II}}$. This already includes that $l_{\mathrm{C}} = n\lambda + \lambda/4$. With this in mind, the signals recombine to following output signals:

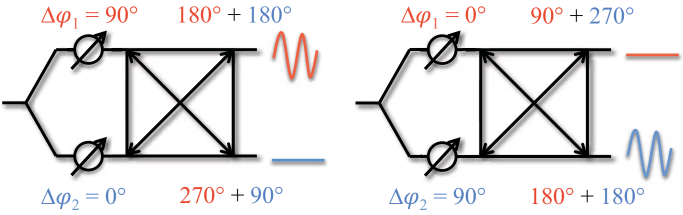

Figure 3.5: Schematic of the two extreme configurations of an interference-based SPDT, where only an output signal is adjusted at port 2 or port 3. Using continuously tunable phase shifters, the signal ratio can be continuously adjusted in between.

$$\begin{aligned}
\underline{b}_2^{\mathrm{III}} &= -\frac{i}{\sqrt{2}}\underline{a}_1^{\mathrm{III}} - \frac{1}{\sqrt{2}}\underline{a}_4^{\mathrm{III}} && (3.13)\\
&= \frac{1}{2}\underline{a}_1^{\mathrm{I}} e^{-i\beta(l_{\mathrm{PD}}+l_{\mathrm{PS}}+l_{\mathrm{C}})} e^{-i\Delta\varphi_1} && (3.14)\\
&\quad + \frac{1}{2}\underline{a}_1^{\mathrm{I}} e^{-i\beta(l_{\mathrm{PD}}+l_{\mathrm{PS}}+l_{\mathrm{C}}+\lambda/4)} e^{-i\Delta\varphi_2} && (3.15)\\
\underline{b}_3^{\mathrm{III}} &= -\frac{1}{\sqrt{2}}\underline{a}_1^{\mathrm{III}} - \frac{i}{\sqrt{2}}\underline{a}_4^{\mathrm{III}} && (3.16)\\
&= \frac{1}{2}\underline{a}_1^{\mathrm{I}} e^{-i\beta(l_{\mathrm{PD}}+l_{\mathrm{PS}}+l_{\mathrm{C}}+\lambda/4)} e^{-i\Delta\varphi_1} && (3.17)\\
&\quad + \frac{1}{2}\underline{a}_1^{\mathrm{I}} e^{-i\beta(l_{\mathrm{PD}}+l_{\mathrm{PS}}+l_{\mathrm{C}})} e^{-i\Delta\varphi_2} && (3.18)
\end{aligned}$$

Therefore, the difference in phase of the two split-up signals is introduced just by the $\lambda/4$ transformation within the combiner as well as the phase shift applied by the phase shifters. If the phase shifters are tuned equally (e.g. $\Delta\varphi_1 = \Delta\varphi_2 = 0°$), the SPDT will ideally provide two identical output signals of 3 dB. If one of the phase shifters is tuned to 90° phase shift compared to the other one, the interference conditions in the combiner section will lead to a constructive interference at one output and a destructive interference at the other output. Assuming $\Delta\varphi_1 = 90°$, $\Delta\varphi_2 = 0°$, $l_{\mathrm{PD}} = n\lambda + \lambda/4$, $l_{\mathrm{PS}} = n\lambda + \lambda/4$ and $l_{\mathrm{C}} = n\lambda + \lambda/4$, as shown in Fig. 3.5, as well as $\underline{b}_2 = \underline{b}_2^{\mathrm{III}}$ and $\underline{b}_3 = \underline{b}_3^{\mathrm{III}}$, the interference scenarios at the outputs result in

$$
\begin{aligned}
\underline{b}_3 &= \frac{1}{2} a_1^{\mathrm{I}} e^{-i3\pi/2} e^{-i\pi/2} + \frac{1}{2} a_1^{\mathrm{I}} e^{-i2\pi} e^{-i0} && (3.19)\\
&= \frac{1}{2} a_1^{\mathrm{I}} e^{-i2\pi} + \frac{1}{2} a_1^{\mathrm{I}} e^{-i2\pi} && (3.20)\\
&= \underline{a}_1 && (3.21)
\end{aligned}
$$

and

$$
\begin{aligned}
\underline{b}_3 &= \frac{1}{2} a_1^{\mathrm{I}} e^{-i2\pi} e^{-i\pi/2} + \frac{1}{2} a_1^{\mathrm{I}} e^{-i3\pi/2} e^{-i0} && (3.22)\\
&= -\frac{i}{2} a_1^{\mathrm{I}} e^{-i2\pi} + \frac{i}{2} a_1^{\mathrm{I}} e^{-i2\pi} && (3.23)\\
&= 0\,. && (3.24)
\end{aligned}
$$

This is one of two extreme configurations, while the other is given vice versa by $\Delta\varphi_1 = 0°$, $\Delta\varphi_2 = 90°$ (see Fig. 3.5). The advantage of using liquid crystal based phase shifters in this configuration is that the phase shift, and therefore, the possible signal relations can be adjusted continuously.

Since several, partly tuneable components are needed for the realisation, various challenges are addressed to the chosen technology, also depending on the specific scope conditions of the given application. Therefore, different technologies have been investigated within this work to be able to adapt best to the diverse requirements in satellite communication and imaging.

4 Planar LTCC Integrated SPDT at Ka-Band

Since nowadays the Ka-band plays an important role in satellite communication, it is used more frequently. Hence, beside an increase of the spectral efficiency, a more resourceful usage of the given frequencies is mandatory. A high degree of frequency re-use, and therefore, a significant increase in system capacity is provided by multiple spot beam antennas [Sch+11]. An example is the 82 Ka-band spot beam antenna used in Eutelsat's KA-SAT, launched in 2010. It is connected to 10 ground stations and allows data transfers with 90 GBit/s, due to the diverse usage of frequencies. The service area is covered by many overlapping small spot beams with high gain, supporting broadband up- and downlink services. There, a four colour scheme is being utilised, which has been proven as an optimal compromise between performance and system complexity. Two frequency sub-bands and two orthogonal polarisations (left and right handed circular) are used, so that the overlapping colours differ either in frequency or in polarisation. Two beams of the same colour are spatially separated from each other.

Those spots can be created by a single feed antenna each. Although this single feed per beam design is simple and shows a very good electrical performance, it is suffering from a large aperture of the overall antenna. To be able to overlap adjacent spots, additional reflector apertures are needed. An optimised design is the multiple feed per beam antenna where the spots are generated by sub-arrays. Adjacent beams share antenna elements, thus, decreasing mass and size of the antenna. The beam-forming relies upon many phase shifters as well as variable attenuators to form the single high gain spots needed for operation. This leads to a very complex beam-forming network as shown in the project *Medusa* [Sch+10].

A promising technology for the reduction of the feeding network's complexity is the standard low temperature co-fired ceramics (LTCC) technology, a multilayer technology with low loss in the micro- and millimetre wave regime. LTCC is a space qualified material and can therefore be used as a carrier material for satellite components. Parts of a beam-forming network have already been integrated into

LTCC as exemplarily shown in [Kle+11] with a Wilkinson power divider. Additional components needed are phase shifters, tuneable attenuators or SPDTs.

Besides the implementation of metallic and resistive structure networks, LTCC also allows the integration of hermetically-sealed cavities. This is a prerequisite for the use of nematic liquid crystal (LC) as a tuneable dielectric. The applicability of LC in LTCC components has already been proven in the research projects *Liquida*[1] and *Liquida 2*[2], which were supported by the German Federal Ministry for Economic Affairs and Energy under the lead of the German Aerospace Center (Deutsches Zentrum für Luft- und Raumfahrt, DLR). Microstrip line and substrate integrated waveguide phase shifters had been investigated, for the usage in electrically steerable phased array antennas [Gae15; Str15]. In *Liquida 2*, the LC-LTCC technology has also been proven to provide a high repeatability [Str+14].

In this chapter, results of the research project *Liquida K*[3] are presented. The objective of this project was the investigation of miniaturised tuneable components for beam-forming networks, specifically tuneable phase shifters, SPDTs and amplitude tuner [Pra+17]. Within the designs of the tuneable components, all non-tuneable single components needed for a Butler matrix design are investigated as well (see Fig. 4.1). By this, the suitability of the LTCC technology for the realisation of a tuneable mixed beam-switching and beam-steering network at W-band can be estimated.

---

[1] FKZ 50 YB 0618
[2] FKZ 50 YB 0921
[3] FKZ 50 YB 1316

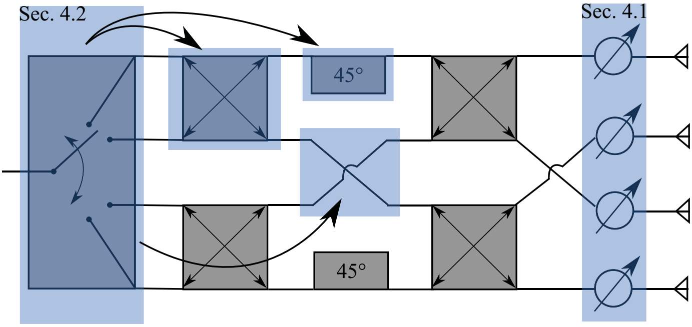

Figure 4.1: Schematic overview of the components investigated in LTCC technology with corresponding section numbers.

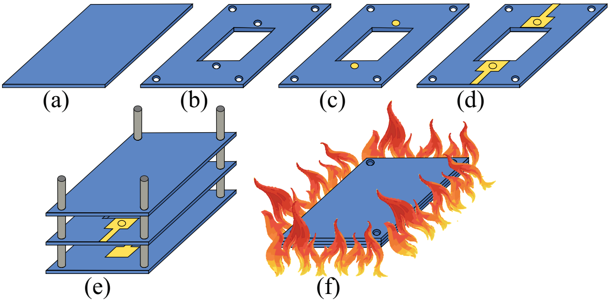

Figure 4.2: LTCC fabrication process. First, the (a) green tape is (b) punched, before (c) the via holes are filled with gold paste. After that, (d) the plane metallisation is applied by screen printing. Then, (e) the different layers are stacked manually before (f) sintering.

Realisation of microwave LC-tuned LTCC components

A schematic of the LTCC fabrication process is given in Fig. 4.2. The commercial tape 9K7 from DuPont was chosen, which is especially suited for RF applications ($\varepsilon_r = 7.1$ & $\tan\delta = 0.0010$ at 10 GHz [DuP]). The thickness of the unfired tapes are 254 µm and 127 µm. Vias and the cavity are generated by punching. For the components investigated in the *Liquida K* project, the LC cavity was punched in one of the thinner tapes only. The other layers are made of the thicker tape for stability purposes. The via holes had been filled with Au-paste LL500. After this, planar metallisation (Au-paste LL505) and resistive layers (resistor paste 2061) were applied on the tapes by screen printing. The conductivity of the gold pastes is given by the manufacturer with $\sigma = 1.33 \cdot 10^7$ S/m, while the sheet resistivity of the resistive paste is given to be $R = 1\,\mathrm{M}\Omega/\square$.

The lamination of the green (unfired) tapes was carried out at 70 °C and 15 MPa in an uniaxial press using a customised pressing tool. The LTCC layers cannot all be laminated in one step, because the buried cavity would have been damaged. Therefore, a bottom and a top part consisting of three LTCC layers each were laminated separately. The single tape containing the cavity had also been predensified with the same pressure. The three parts (bottom, top and cavity layer) were then joined still in a green state by low pressure lamination. A water based adhesive, 2 % solution of hydroxyethyl cellulose dissolved in de-ionized water, was brushed on the laminates and a low pressure of 3 MPa was applied for 3 minutes on the preheated parts (70 °C).

The components were sintered at 865 °C peak temperature for 20 minutes. A 27 h sintering profile with very low heating rates was used, which is recommended by the tape manufacturer for 9K7. During sintering, a shrinkage of 8.8 % in lateral direction and 10.6 % in thickness direction occurs. The shrinkage is already accounted for in the design of the components. After sintering, the modules were cut out of the LTCC laminate. Finally, the LC was injected in the cavity under vacuum conditions and the cavity was sealed.

4.1 Stripline Phase Shifter

As being essential for almost all tuneable components, the phase shifter has been investigated individually. The focus was set on the question, if the differential phase shift provided by the phase shifter can be accurately determined by using the in-house director dynamics simulation tool *SimLCwg* presented in [Gae15]. This is mandatory for the later application, since the overall components are completely embedded inside the LTCC and cannot be separately characterised. Further, commercially available simulation tools, such as CST Studio Suite, which was used for all design processes within this thesis, are not able to sufficiently determine the phase shift. The tuneable LC material can only be simulated as a block with homogeneous LC alignment. This is due to the fact, that director dynamics, and therefore, effects like surface anchoring cannot be taken into account.

Further, the compactness of the investigated components was an important parameter. Due to this, low profile types of transmission lines had been preferred, which is why the embedded waveguide from *Liquida 2* was not taken into account. Since the LTCC components are realised of individually screen printed layers, a CPW structure is also not reasonable, because the corresponding mode would only propagate through a marginal part of the LC, which can only be on top or below the CPW. The most useful type, being further investigated in the following, is the microstrip line.

While the high permittivity of the 9k7 green tape is beneficial for miniaturising the components, it simultaneously involves several disadvantages connected to the design and fabrication process. One disadvantage is the high permittivity difference between LTCC and LC, causing the RF field to focus in the non-tuneable LTCC material. To overcome this issue, the ground plane of the microstrip line within the LC filled section is designed with the same width as the signal line, focussing the

RF field denser inside the LC. By this, a higher phase shift per unit length can be achieved. Pre-investigations on this issue have already been presented in [Str15].

The second disadvantage is directly connected with the fixed minimum substrate height of 107 µm (after sintering): due to the fabrication limitation in the screen printing process, only allowing line widths of $\geq 100\,\mu\text{m}$, it is not possible to realise microstrip lines with a preferred impedance of $50\,\Omega$, but $46\,\Omega$ in maximum. Only in the embedded LC section a $50\,\Omega$ design is possible, due to the lower permittivity of LC. Another fabrication limitation is the dimensions of the punching tools, only allowing LC cavity widths of $\geq 1\,\text{mm}$.

Design

A cross-section of the phase shifting section is given in Fig. 4.3. The LC cavity was chosen with a height of 107 µm, corresponding to the height of one thin LTCC layer. For the LC orientation a fully electrical biasing system is implemented. While the parallel LC orientation can be provided by applying a DC voltage V_V to the microstrip line itself, the perpendicular orientation is provided by additional resistive biasing lines. By applying biasing voltages of $\pm V_\text{H}$ to these biasing lines,

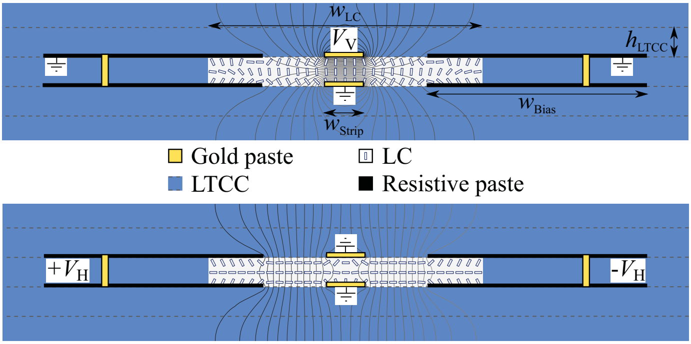

Figure 4.3: Cross-section of the LC-tuned LTCC microstrip line phase shifter. The biasing fields are given both for (top) the parallel and (bottom) the perpendicular orientation of the LC. The most important dimensions are $w_\text{LC} = 1\,\text{mm}$, $w_\text{Strip} = 140\,\mu\text{m}$, $w_\text{Bias} = 800\,\mu\text{m}$ and $h_\text{LTCC} = 107\,\mu\text{m}$.

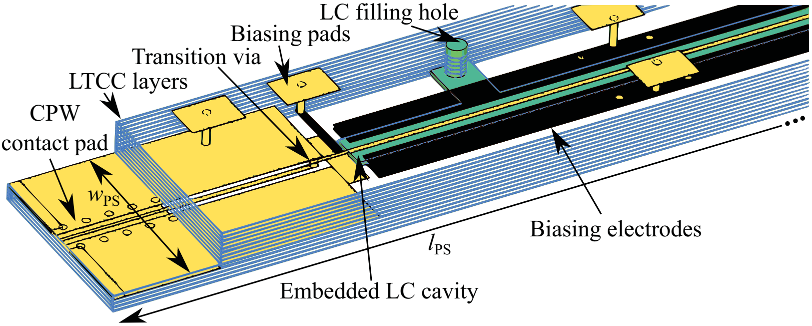

Figure 4.4: Schematic of the LC-tuned LTCC phase shifter design. The most important dimensions are $w_{PS} = 5.5\,\text{mm}$ and $l_{PS} = 31.0\,\text{mm}$.

horizontal biasing fields are generated. The biasing lines on each side are electrically connected by a via and made of high resistive paste to not affect the RF field.

A three dimensional schematic of the phase shifter design is shown in Fig. 4.4. Since the LC filling needs to be done after the sintering process, a filling hole is included to the design, by which the phase shifter is filled under vacuum conditions. Afterwards, this filling hole is sealed. The biasing voltages are provided to the biasing pads on the top of the phase shifter demonstrator, being connected to the biasing-/striplines by means of vias and resistive conductors. For the characterisation of the phase shifter, a transition from microstrip line to CPW is needed, which has been realised with the help of a via. This CPW is then guided outside the LTCC, where it changes to a grounded CPW. By the use of RF probes, the phase shifter demonstrator can then be connected to the vector network analyser (VNA).

The total design has a length of $l_{PS} = 31.0\,\text{mm}$ and a width of $w_{PS} = 5.5\,\text{mm}$. The phase shifting section has a length of $l_{LC} = 14.6\,\text{mm}$. For this length, a phase shift of 60.6° is predicted by *SimLCwg* at 30 GHz.

Realisation

Since the phase shifters will be fully embedded in LTCC, test samples need to be realised in order to verify the reliability of the fabrication process. First, embedded test cavities were fabricated under different conditions. Structural cuts of two cavities are shown in Fig. 4.5. For the first cavity no pre-lamination of the LTCC

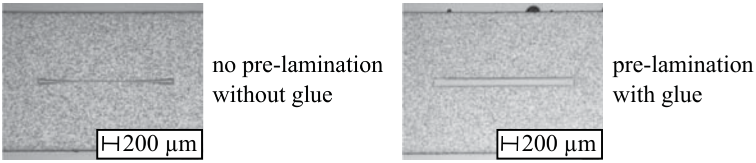

no pre-lamination without glue

pre-lamination with glue

Figure 4.5: Cut-view of embedded test cavities where (left) no pre-lamination and no additional glue was used while (right) pre-lamination and additional glue was used to provide a better stability.

parts (top, bottom and cavity, as explained before) was done and no glue had been used. It is obvious that the stability needed for the realisation of an embedded cavity is not given in this way. On the other hand, when pre-laminating the different parts and using the special water based adhesive, the cavity results in a well-defined rectangular shape. A structural cut of a complete phase shifting section is given in Fig. 4.6, including the stripline and biasing lines.

Several fabrication tolerances are shown there. First, a misalignment of the different layers to each other is visible. This is because the different layers are aligned with special tools, but still by hand. Further, the cavity is more narrow in the centre, due to the high pressure needed during lamination. Ruptures at the edges of the resistive biasing lines are also visible, which occur during the sintering process. Nevertheless, these fabrication tolerances are not affecting the overall performance of the phase

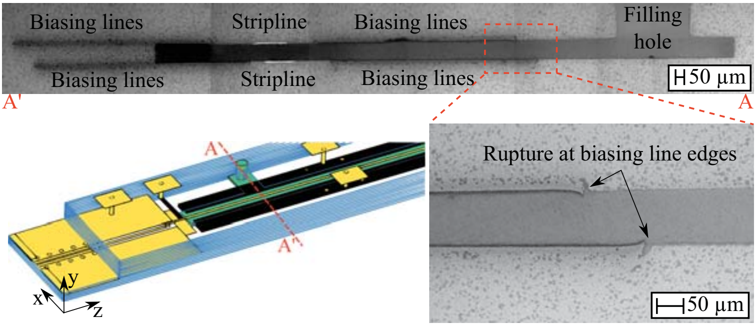

Figure 4.6: Structural cut of the phase shifter at the level of the filling hole. The cut is in the x-y-plane and the propagation direction is in z-direction.

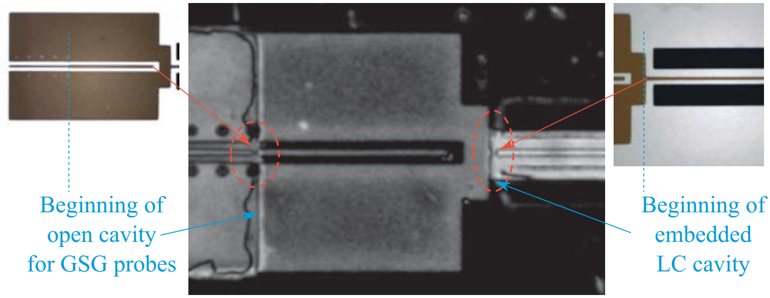

Figure 4.7: Ultrasound investigation of a realised phase shifter. At transitions from cavities to fully embedded LTCC parts, interruptions of the metallic striplines occur. On the left and right, the original structures are shown right after screen printing.

shifter much. The spatial shift between the layers is only about 50 µm, causing an increase in insertion loss of 3.5 % in maximum. The difference in height is about 10 µm (90 µm in the centre, compared to 103 µm at the edges), causing an increase in insertion loss of less than 1.0 % and a frequency shift of 1 GHz in maximum.The ruptures only distort the DC biasing field slightly. Although the lower cavity height causes a mismatch, it also results in a benefit of a reduced response time.

Further investigations on the realised phase shifters have been conducted by means of ultrasound (see Fig. 4.7). Interruptions of the gold metallisation could be made

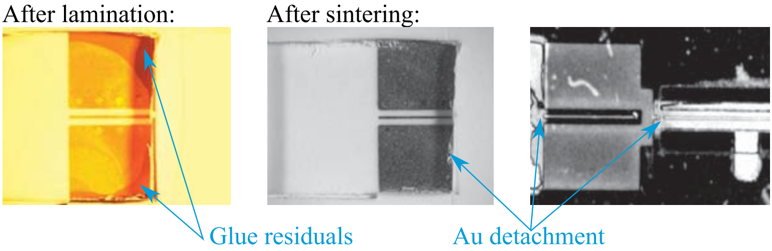

Figure 4.8: Stereomicroscopy of a phase shifter (left) with glue residuals after lamination and (middle) detached gold metallisation after the sintering process. In (right), an ultrasound image of the phase shifter with an interrupted transmission line is given.

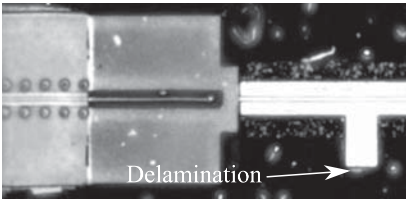

Figure 4.9: Ultrasound image of the phase shifter after the lamination and sintering process without the use of the water based adhesive. No interruptions of the transmission line can be made out but only a small delamination at the LC filling channel.

out at the transition from fully embedded LTCC parts to the embedded LC cavity or the open cavity of the CPW contact pad. It is called open cavity, since the LTCC layer above the CPW contact pad need to be punched out in this area during the fabrication process. The interruptions are due to glue residuals arising from the lamination process. If the glue is in contact with the gold paste in a region where it is not fully embedded in LTCC, it is able to dissolve the gold metallisation from the LTCC laminates during the sintering process, as shown in Fig. 4.8. Therefore, only a small amount of glue has been used in the lamination process to avoid gold detachments, although this could lead to delamination, as shown in Fig. 4.9. These delaminations only occurred in a small region at the edge of the embedded cavity as well as at the bottom of the filling section. Despite the fact that these small slits are then filled with LC, they are too far away from the signal line to influence the RF field.

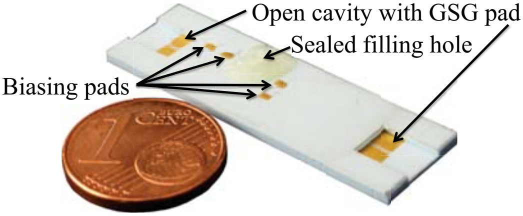

Figure 4.10: Photograph of the LC-tuned LTCC phase shifter demonstrator. The LC filling hole was sealed by epoxy glue after the filling process.

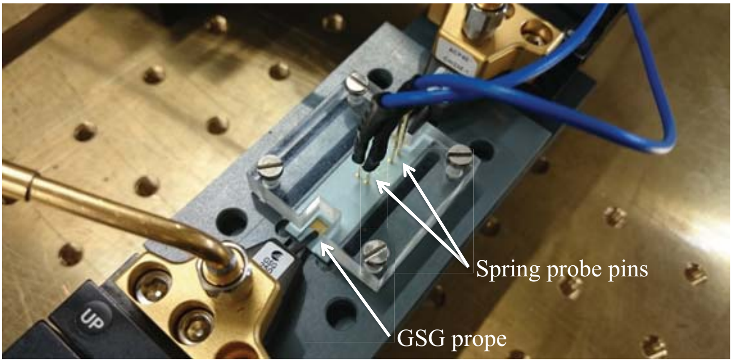

Figure 4.11: Measurement setup of the LC-tuned LTCC phase shifter. The biasing voltage is supplied by means of spring probe pins, while the contact pads in the open cavities are connected by ACP GSG 250 probes.

The final phase shifter demonstrator is given in Fig. 4.10. It has been filled with the LC GT3-23001 (for dielectric properties see Tab. 2.1) under vacuum conditions to avoid air bubbles inside the cavity, since this would lower the tuneability and lead to a mismatch. Afterwards, the filling hole was sealed with epoxy glue.

Characterisation

Fig. 4.11 shows the measurement setup of the phase shifter. It was connected to the VNA (PNA-X from Keysight Technologies) via ACP40 GSG 250 probes from Cascade Microtech. The DC biasing pads were connected with the help of spring probe pins to the voltage source (Keithley 2612). The phase shifter is mounted on a sample holder made of polyvinyl chloride (PVC), being fixed to a self-made probe station. By this, possible field distortions caused by metallic chucks are avoided. A comparison of the simulated and measured S-parameter results for the phase shifter are given in Fig. 4.12. The simulations were carried out with CST Studio Suite and the measurements were carried out using biasing voltages of $V_\mathrm{V} = 50\,\mathrm{V}$ for the parallel and $V_\mathrm{H} = \pm 200\,\mathrm{V}$ for the perpendicular alignment in maximum.

The matching fits the simulation well close to the design frequency with values better than $-10\,\mathrm{dB}$ between 30.3 GHz to 34.4 GHz. Beside this frequency range, the phase shifter is not matched sufficiently with values around $-5\,\mathrm{dB}$. The reason

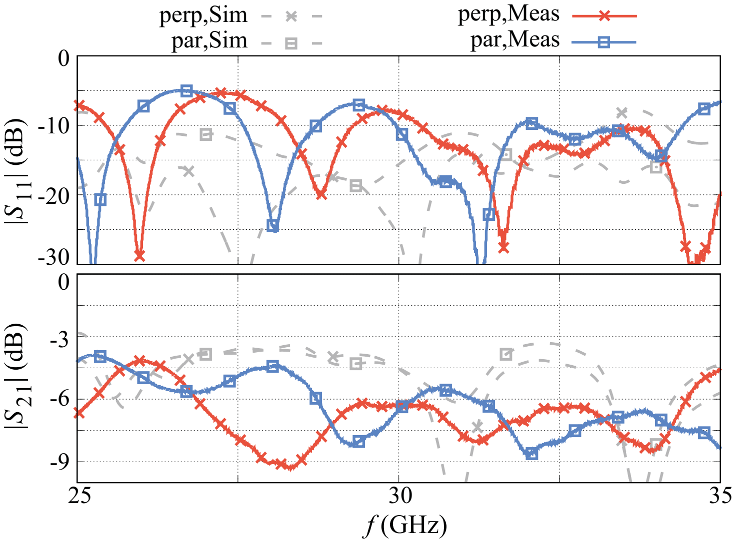

Figure 4.12: Comparison of the simulated and measured S-parameters for the LC-tuned LTCC phase shifter. The frequency dependent simulations were conducted with CST Studio Suite

for the mismatch compared to simulation is the fabrication tolerances of the LTCC process, such as the shift between the different layers due to the manually stacking process as well as the compression of the LC cavity during the lamination process.

The insertion loss is higher than expected with values of 5.5 dB to 7.5 dB between 30.3 GHz 34.4 GHz. This high insertion loss arises amongst other from the more than three times decreased conductivity of the used gold paste compared with conventional gold as well as the surface roughness of the LTCC tapes, and therefore, the transmission line structures. This aspect will be discussed in detail in the SPDT section. Nevertheless, for the design frequency of 30 GHz the phase shifter shows a constant insertion loss of 6 dB, independent from the tuning state. This is a preferred property for interference-based SPDTs.

The phase shift supplied by the phase shifter is very rippled, as can be seen in Fig. 4.13. This is caused by standing waves inside the LC section, originating from badly matched transition vias. However, the phase shift of 60.6° at 30 GHz proposed by

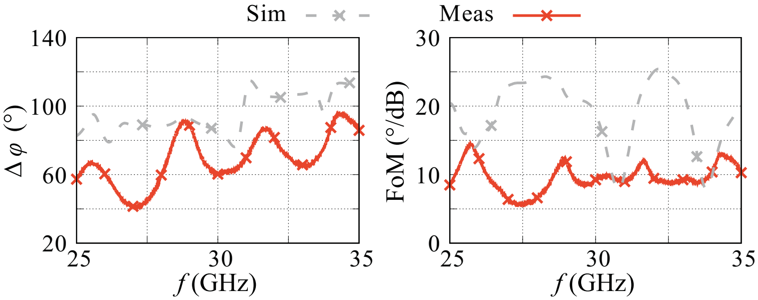

Figure 4.13: (left) Phase shift and (right) figure of merit of the LTCC based LC phase shifter. The simulations were conducted with CST Studio Suite.

the in-house simulation tool *SimLCwg* could be accurately confirmed with measured value of 60.9°. The simulated values from CST Studio Suite are higher than the measured ones and the one predicted by *SimLCwg*, since they are based on ideal parallel and perpendicular alignment of the LC.

The corresponding FoM reaches mean values of 10 °/dB between 29 GHz to 34 GHz. A not negligible part of this loss is arising from the open cavity to embedded LTCC transitions as well as the CPW-to-microstrip line transition via. This was proven by the realisation of a reference line, being the same device as the phase shifter, but excluding the phase shifting section. A schematic of this reference line and a picture of the demonstrator are given in Fig. 4.14. The simulated and measured results are shown in Fig. 4.15. While matching is partially good, it shows an insertion loss

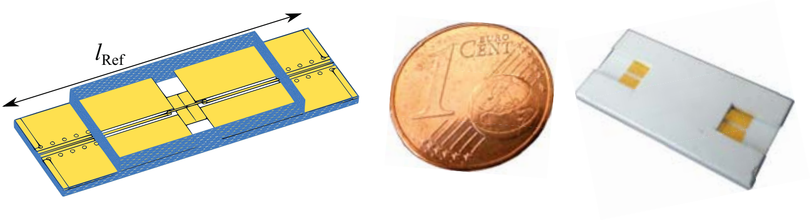

Figure 4.14: Schematic and final demonstrator of the LTCC reference line. The total length is $l_{\mathrm{Ref}} = 15\,\mathrm{mm}$.

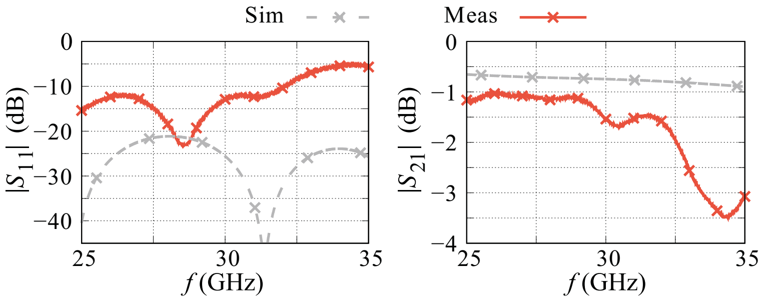

Figure 4.15: Simulated and measured (left) reflection and (right) transmission coefficients of the LTCC reference line.

from 1.0 dB to 3.5 dB in the measured frequency range. Therefore, a new transition topology is needed for the SPDT design. The deviations between the measured and simulated results are arising from the same limitations as mentioned before, such as the decreased gold conductivity as well as the surface roughness.

The results of the response time measurements are given in Fig. 4.16. They were measured with a continuous wave time sweep using Keysight's PNA-X. It was measured to $\tau_{90\%}^{10\%} = 57\,\text{ms}$ for the case from perpendicular to parallel orientation and $\tau_{10\%}^{90\%} = 36\,\text{s}$ from parallel to perpendicular orientation, when applying biasing

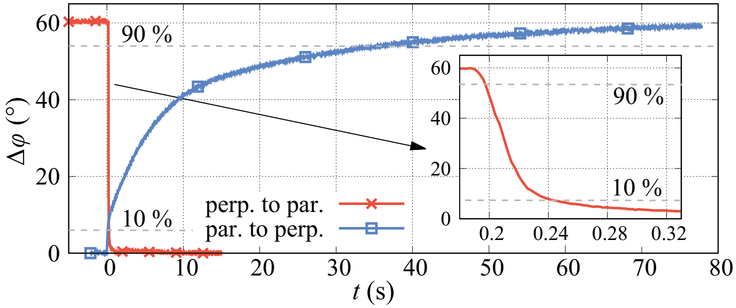

Figure 4.16: Results of the response time measurement of the LC-tuned LTCC phase shifter filled with GT3-23001. For these measurements $V_{\text{V}} = 50\,\text{V}$ had been used for the parallel and $V_{\text{H}} = \pm 200\,\text{V}$ for the perpendicular state.

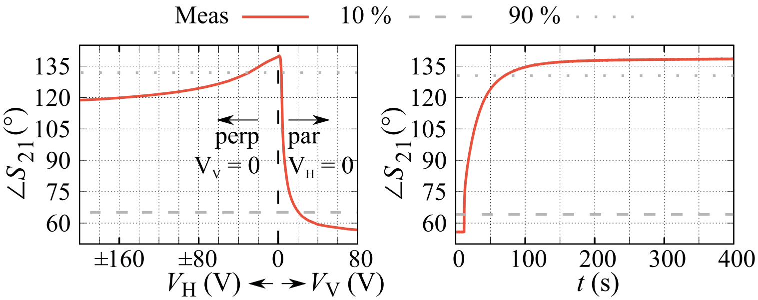

Figure 4.17: (left) Phase state of the LC-tuned LTCC phase shifter in dependency of the biasing voltage. (right) Response time measurement of the LC-tuned LTCC phase shifter for the parallel-to-switch off case.

voltages of $V_\mathrm{V} = 50\,\mathrm{V}$ and $V_\mathrm{H} = \pm 200\,\mathrm{V}$ for the parallel and perpendicular case, respectively. Although the voltage dependent measurements of the phase shift in Fig. 4.17 show that lower voltages are already sufficient, these high biasing voltages have been chosen for keeping the response time as low as possible.

The voltage-dependent measurements also show that the highest phase shift is achieved for a perpendicular orientation with a biasing voltage of $V_\mathrm{V} = V_\mathrm{H} = 0\,\mathrm{V}$. This is obvious when calling Fig. 4.3 into memory, where the RF striplines are acting as floating electrodes during the perpendicular orientation, causing a parallel LC alignment in the vicinity of the striplines. If the biasing voltages are switched off, the LC can homogeneously align to the perpendicular orientation by means of surface anchoring. Despite of the switched-off voltage and without the use of an alignment layer, this is a reproducible state. It originates from a weak surface anchoring of the LC directors at the cavity walls, striplines and the biasing electrodes, as already discussed in [Gö09]. Consequently, this switch-off state has a longer response time, which was measured to $\tau_\mathrm{off} = 58\,\mathrm{s}$ (see Fig. 4.17). However, for the SPDT design, the phase shift for the perpendicular orientation with $V_\mathrm{B} = \pm 200\,\mathrm{V}$ is taken into account in order to keep the response time low and for having some backup phase shift for compensating possible fabrication tolerances.

4.2 Single-Pole Double-Throws

In addition to tuneable phase shifters, the electrically tuneable LC-tuned LTCC SPDT comprises of the following single components:

- **DC blocking structures:** for preventing the biasing voltage applied at one phase shifter to influence the other phase shifter
- **Power divider and combiner:** for power division/re-combination at the input/output section
- **Transition:** for mode conversion from the grounded CPW at the open cavity to the fully embedded microstrip line and vice versa
- **GSG(SG)-probe contact pad:** for connection of the SPDT to the VNA

For the component design in the embedded LTCC part, a microstrip line topology was chosen, because the design of bended structures, being essential for power dividing/combining components, is much simpler than in CPW topology [Lam+08; Fan+96]. On the other hand, the demonstrator will be connected to the measurement setup by on-wafer probes, which is why for the contact pad design at the open cavities a grounded CPW topology was chosen. Hence, CPW-to-microstrip line transitions are mandatory for supplying the needed mode conversion at the interface between open cavities and the embedded LTCC part.

Due to these kind of design criteria, CPW-to-microstrip line transitions for LTCC applications are of great interest in research [Bhu+17; Nai+13; Lei+05]. While most CPW-to-microstrip line transitions are designed vertically based on vias, as for the aforementioned LC-tuned LTCC phase shifter, the transitions of the LC-tuned LTCC SPDTs are based on a capacitive coupling as in [Zhu+14]. By this, the transitions can directly function as DC blocking structures.

Due to the fabrication constraint of a minimum conductor width of 100 µm, a fully embedded microstrip line can maximally achieve an impedance of $Z_0 \approx 45\,\Omega$ for a substrate height of $h_{\mathrm{LTCC}} = 107\,\mu\mathrm{m}$ (1 layer of 9k7 tape). Further, by working at the lowest limit of the screen printing process, the edges of the transmission lines can be rippled, resulting in a continuous change in line width.

Therefore, two SPDT topologies have been realised within the *Liquida K* project, one with the highest possible impedance of $Z_0 \approx 45\,\Omega$ (SPDT50) and one with an impedance of $Z_0 \approx 32\,\Omega$ (SPDT32) within the embedded LTCC section. This results in stripline widths of $w_{\mathrm{Strip}} > 210\,\mu\mathrm{m}$, by which a rippled shape of the transmission lines can be avoided. However, the GSG(SG)-probe contact pads in the open cavities have always been designed to $Z_0 = 50\,\Omega$. Thus, the embedded structures with $Z_0 = 32\,\Omega$ are matched by the CPW-to-microstrip line transitions to the GSG(SG)-probe contact pads.

Different conductor widths also require different sub-component designs of the SPDTs. While there is still a certain variety in the design for conductor widths of $w_{\text{Strip}} > 210\,\mu\text{m}$, the options for the individual components are rather limited at conductor widths of $w_{\text{Strip}} = 100\,\mu\text{m}$. Both designs, including their simulation and characterisation results, will be explained in the following sub-sections.

4.2.1 Impedance-Dependent Designs

SPDT32

The characteristic impedance of $32\,\Omega$ was chosen, since typical dimensions needed for power divider/combiner are realisable within the screen printing limitations.

$$Z_0 = 31.3\,\Omega \;\hat{=}\; w_{\text{Strip}} = 211\,\mu\text{m} \tag{4.1}$$

$$\Rightarrow \quad Z_0/\sqrt{2} = 22.1\,\Omega \;\hat{=}\; w_{\text{Strip}} = 368\,\mu\text{m} \tag{4.2}$$

$$\Rightarrow \quad Z_0 \cdot \sqrt{2} = 44.6\,\Omega \;\hat{=}\; w_{\text{Strip}} = 100\,\mu\text{m} \tag{4.3}$$

All designed sub-components as well as their simulation results are given in Fig. 4.18 and Fig. 4.19.

The power divider was designed in a rat-race topology, where the isolated port is additionally terminated by an embedded resistor with the size of $1.00\,\text{mm} \times 1.52\,\text{mm}$. A Wilkinson power divider, commonly used for power division in microstrip line topology, could not be chosen, since the design rules of the screen printing process would need to be infringed. The size of the needed embedded resistor would be too small ($100\,\mu\text{m} \times 200\,\mu\text{m}$) to achieve a reproducible resistance, since relative deviations in the screen printing/sintering process would be high. In case of the rat-race coupler, the resistor is not underlying any design restrictions. According to the simulations, the rat-race coupler shows an equal power split of $|S_{21}| = |S_{31}| \approx -3.8\,\text{dB}$.

The combiner was designed as branchline coupler, since a four-port device is needed for the re-combination of the split-up signals and further distribution to both output ports. The system-inherent phase difference of 90° applied between the two input

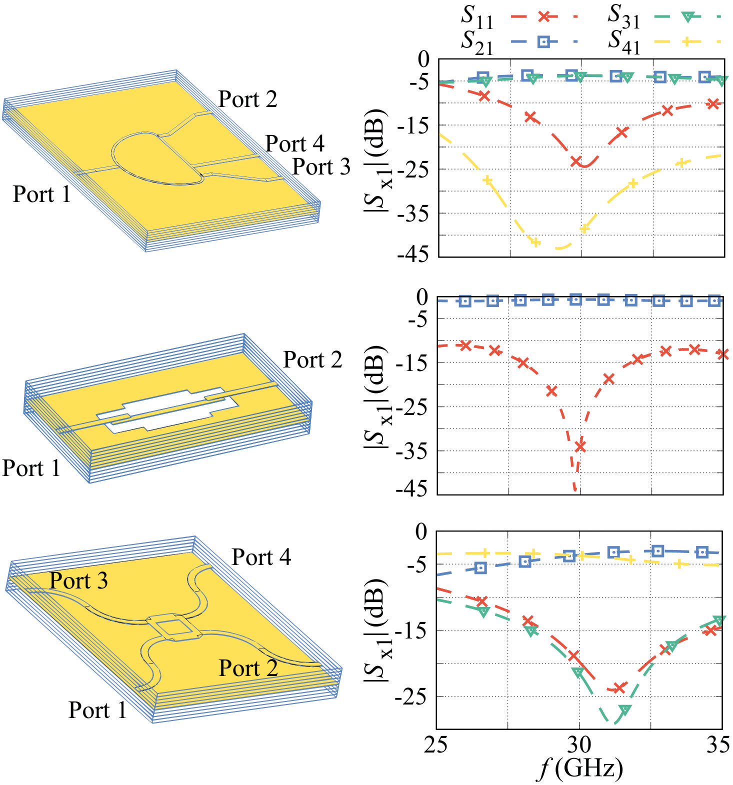

Figure 4.18: Schematics and simulation results of the embedded sub-components (from top to bottom) rat-race coupler, DC blocking structure and branchline coupler of the SPDT32. The most important dimensions are given in appendix A.1.

signals, together with the phase shift supplied by the phase shifters, lead to the preferred interference conditions at both output sections of the SPDT. The branchline coupler exhibits a simulated insertion loss of around 0.7 dB.

Cascaded CPW-to-microstrip line transitions similar to [Zhu+04], placed in each branch between phase shifter and power divider/combiner, are functioning as DC

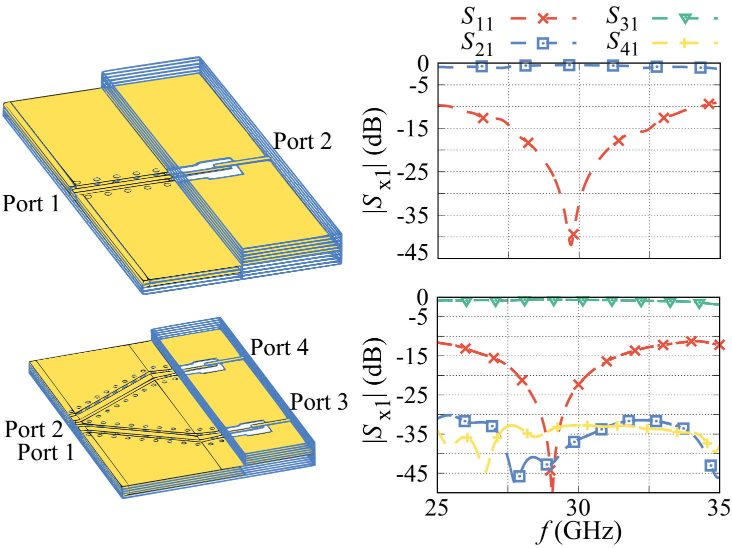

Figure 4.19: Schematics and simulation results of the GSG(SG) contact pads, including the embedded CPW-to-microstrip line transitions of the SPDT32. The most important dimensions are given in appendix A.1.

blocking structure. This ensures that the biasing voltage of one phase shifter cannot have an impact on the second one, being at an expense of 0.7 dB of insertion loss. Single versions are also used as transitions from the embedded microstrip line to the open cavities. There, a GSG as well as a GSGSG contact pad for RF probes have been designed in grounded CPW topology. Together with the CPW-to-microstrip line transitions, the GSG- and GSGSG-contact pads show a simulated insertion loss of 0.5 dB and 0.7 dB, respectively.

Fig. 4.20 shows the complete design of the SPDT32, including all the sub-components mentioned above as well as the tuneable phase shifters. Each phase shifter has a separate filling channel. The ports are labelled as they appear later on in the measurements. The complete SPDT has a width of 12.0 mm and a length of 68.2 mm, while the LC cavity already has a length of 26 mm.

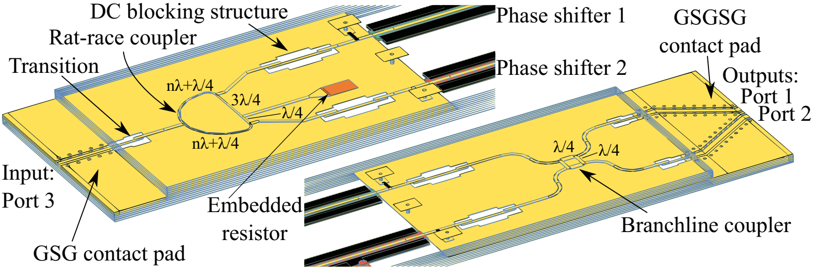

Figure 4.20: Schematic of the interference-based LC-tuned LTCC SPDT, designed for a line impedance of 32 Ω in the embedded section.

SPDT50

The second SPDT was designed as close as possible to 50 Ω with embedded stripline widths of 100 µm. The overall design is given in Fig. 4.21. Due to the small conductor width, only a branchline coupler can be considered as power splitter as well as combiner. Hence, it results in a four-port device, where the unused branch of the power dividing branchline coupler is guided back to the open cavity (port 4). By this it is possible to track the signals in this branch while at the same time terminating it ideally.

The branchline coupler causes a phase difference of 90° between the split up signals, which must be compensated by a fixed phase shifter, realised as meander line. The

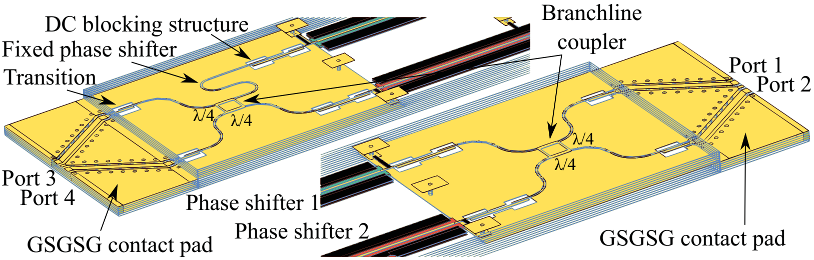

Figure 4.21: Schematic of the interference-based LC-tuned LTCC SPDT, designed for a line impedance close to 50 Ω.

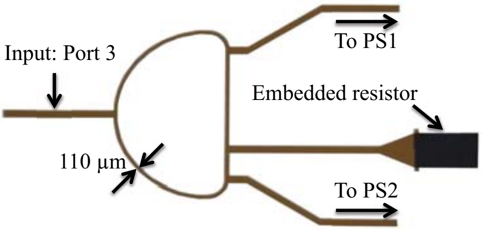

Figure 4.22: Screen-printed rat-race coupler of the SPDT 32 before the sintering process. The stripline width of the rat-race itself is 110 µm instead of the designed 100 µm, due to the shrinkage during sintering.

general design of the GSGSG contact pads, DC blocking structures and transitions are the same as for the SPDT32. Only the dimensions needed to be adapted, based on the smaller conductor widths. The total length of the SPDT50 is with 58.9 mm shorter than the SPDT32. The width is with 12.0 mm the same as for the SPDT32. The LC cavity is also shorter with 24.3 mm, being already sufficient for the the provision of 90° phase shift.

4.2.2 Demonstrator Realisation

The SPDTs have been realised in the same way as the phase shifter, only that for stability reasons 10 instead of 7 layers of LTCC were used.

The screen-printed rat-race coupler of the SPDT32 is shown in Fig. 4.22. The embedded resistor is partially overlapping the taper made of gold to ensure a proper contact. In the green state, the strip width of the rat-race is 110 µm since the shrinkage during the sintering process is taken into account. A rippled shape of this stripline can be made out, originating from the lower limit of 100 µm of the screens. Nevertheless, simulations showed that slightly rippled shapes have no significant influence on the overall performance.

Further, by taking the experience gained from the phase shifter realisation into account it was possible to fabricate the SPDT32 without any detectable delamination (see Fig. 4.23). At the SPDT50, however, similar delaminations can be made out as for the phase shifter, having no noticeable influence on the overall performance since they only appear at the edge of the biasing electrodes as well as the LC filling hole, as can be seen in Fig. 4.24.

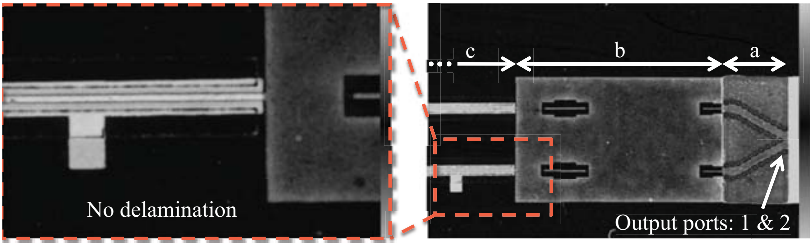

Figure 4.23: Ultrasound image of a test structure of the SPDT32. (left) No delamination can be made out in (right) the different regions of (a) open cavity, (b) embedded transmission line structures and (c) the embedded LC cavity.

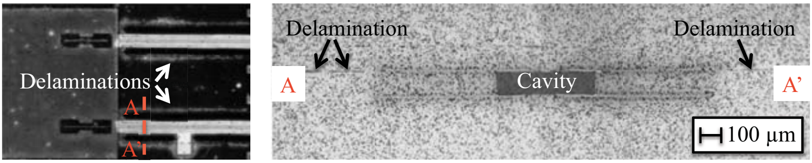

Figure 4.24: (left) Ultrasound image and (right) structural cut of the SPDT50's embedded LC cavity. Delaminations have mainly been made out at the outer part of the resistive biasing electrodes.

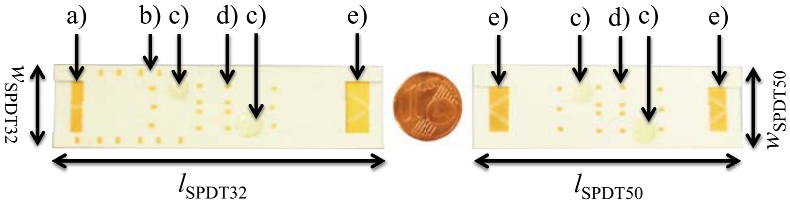

Figure 4.25: Photograph of the SPDT demonstrators with (left) the SPDT32 and (right) the SPDT50. The most important parts are given with a) the GSG contact pad, b) the embedded test resistors for the rat-race, c) the sealed filling holes, d) the DC biasing pads and e) the GSGSG contact pads. The overall dimensions are given by $l_{\text{SPDT32}} = 75\,\text{mm}$, $w_{\text{SPDT32}} = 19\,\text{mm}$, $l_{\text{SPDT50}} = 66\,\text{mm}$ and $w_{\text{SPDT50}} = 20\,\text{mm}$

The final demonstrators are shown in Fig. 4.25. At each side of the input port of the SPDT32, 3 embedded resistors, as needed for the rat-race coupler, have been included to the design, to separately validate the resistance. They are connected to the contact pads on the top of the demonstrator by gold vias. Both demonstrators were filled with the LC GT3-23001.

4.2.3 RF and Surface Roughness Characterisation

The SPDTs have been measured in the same way as the phase shifter, as can be seen in Fig. 4.26. The biasing pads are contacted by spring probe pins, while for the connection to the VNA (PNA-X from Keysight Technologies) ACP GSGSG 500 probes from Cascade Microtech were used to enable four-port measurements. The characterisation results for both SPDTs will further be compared with their simulation results, being carried out with CST Studio Suite. Fig. 4.27 gives a comparison of the measured and simulated best biasing configurations of both SPDTs. In these configurations the highest isolation between both output ports and lowest insertion loss of the thru-port are achieved.

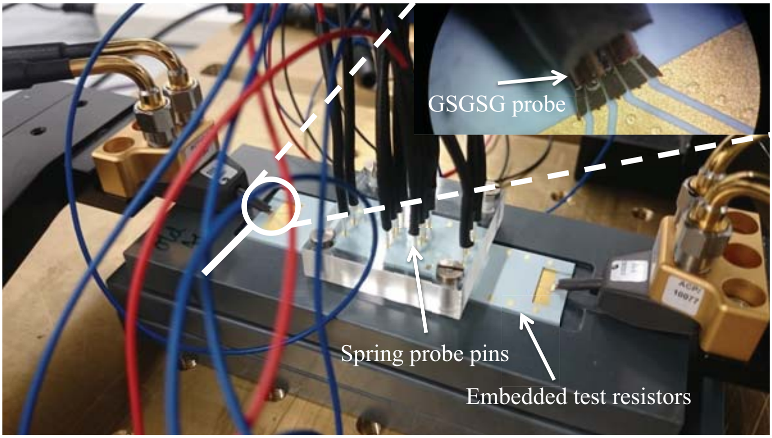

Figure 4.26: Measurement setup for the microwave characterisation of the SPDT32, including the spring probe pins for biasing as well as the ACP GSGSG 500 probes.

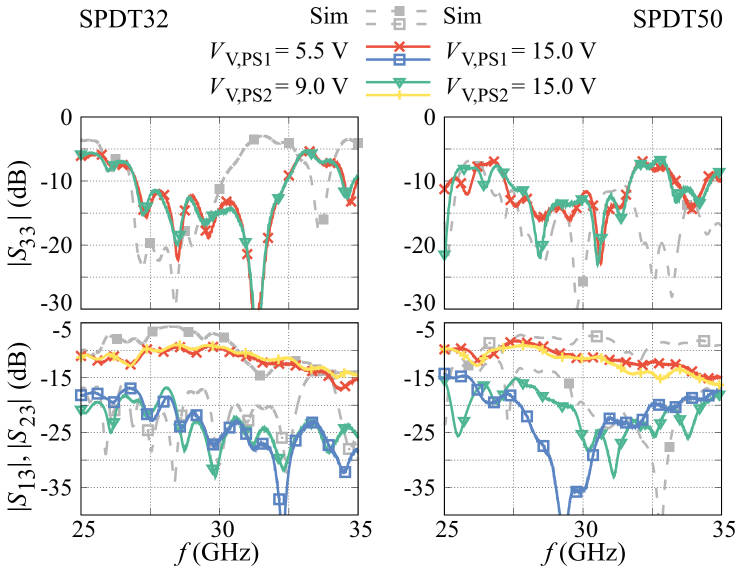

Figure 4.27: Comparison of the simulation and measurement results of the SPDT32 and SPDT50 for both best biasing configurations each. Note: both best biasing configurations of each SPDT are shown. This means, if a biasing voltage was supplied to phase shifter 1, phase shifter 2 was in the switch-off state and vice versa.

The matching of the SPDT32 is with $|S_{33}| < -10\,\text{dB}$ over a bandwidth of 18 % more wide band than simulated. The embedded test resistors were also measured with a mean value of 26.5 Ω. For the SPDT50 the measurements meet the simulation well up to 31.5 GHz. From this frequency on, the matching is getting worse. However, this SPDT is also matched well within a bandwidth of 15 %.

With values between 9 dB to 10 dB the insertion loss of the SPDT32 is around 3 dB higher than simulated, converging to the simulated values at higher frequencies. Directly linked to this is the improved isolation of 20 dB to 25 dB around the design frequency. The SPDT50 shows a steeper behaviour in the insertion loss. Where the insertion loss is around 8 dB to 9 dB at 27.5 GHz it already exhibits values of 12 dB at the design frequency of 30.0 GHz. Consequently, the isolation is also less broadband as for the SPDT32, but has higher extreme values up to 35 dB.

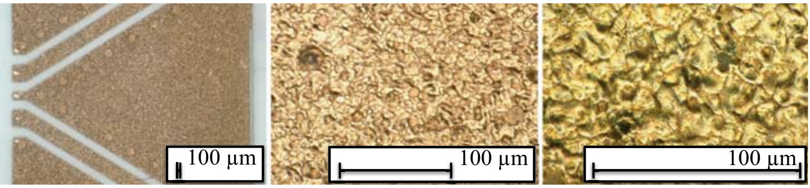

Figure 4.28: Microscopy of the SPDTs contact pad. The magnification has been increased in the area of the gold paste, to be able to evaluate the surface roughness.

The increased insertion loss arises from the surface roughness of the gold metallisation, as being mentioned in the phase shifter section. Simulations showed that only an increase in the metallisation's loss can have such an high impact on the overall performance of the SPDTs. In Fig. 4.28, a microscopy of the GSGSG contact pad of the SPDT32 is given for different magnifications, being recorded with a Keyence VHX 5000 digital microscope. While the surface seems homogeneous in the first place, it exhibits a high inhomogeneity with increasing magnification. Gold bumps of varying granulation as well as valleys with a diameter of more than 20 µm are

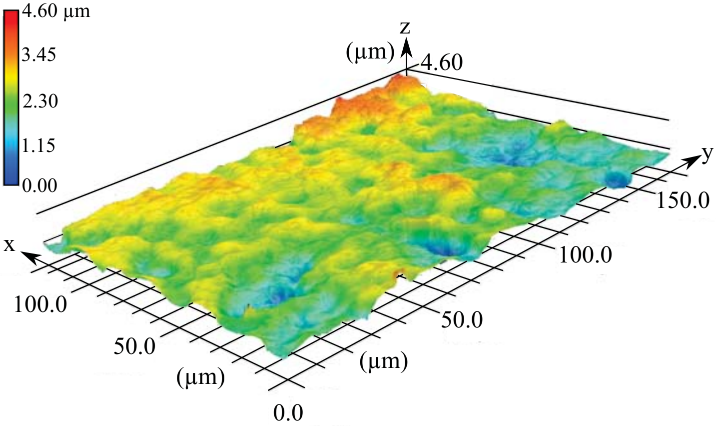

Figure 4.29: Measurement of the SPDT's gold paste surface roughness as shown in Fig. 4.28.

identifiable. The bumps and valleys are arbitrarily distributed.

The microscope was also able to evaluate the surface roughness quantitatively, which is shown in Fig. 4.29. It can be seen that the metallisation shows a difference in height of 4.6 µm between the highest and lowest point within the inspected area. The slopes can thereby almost vary strongly. This and the fact that only a small and open area had been measured make a quantitatively evaluation of the surface roughness throughout the complete SPDT impossible. Nevertheless, assuming an average roughness of 5.0 µm of height change every 50.0 µm, which is a realistic scenario in the evaluated region, the path length would increase by 0.5 %.

A more detailed investigation of the surface roughness had been conducted with a DekTak contact profilometer. There, three areas of different length were measured to evaluate not only the roughness of the metallisation, but also the LTCC itself. The results are given in Fig. 4.30. There are various parameters which are available for the evaluation of profiles. The most important ones are the arithmetical mean deviation R_a, the root-mean-squared (rms) roughness R_q, the mean roughness depth R_z and the total roughness depth R_t, all being introduced in appendix A.2.

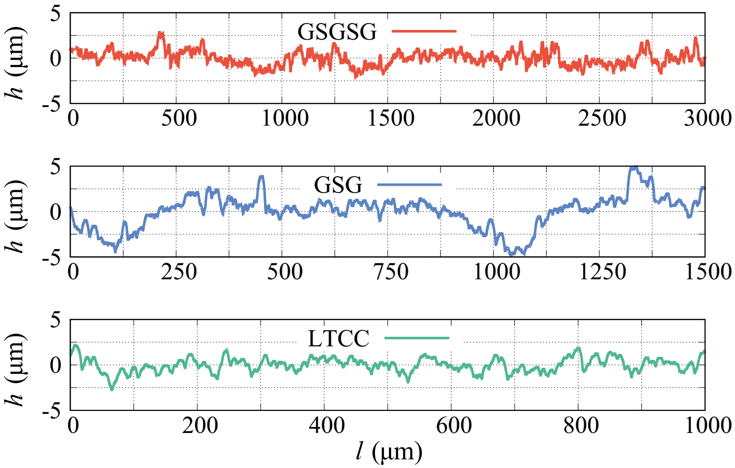

Figure 4.30: Surface roughness of the SPDT32's gold metallisation at the (top) GSGSG and (middle) GSG contact pads. In (bottom) the surface roughness of the LTCC itself is given.

Table 4.1: Evaluation of the measured surface roughnesses in Fig. 4.30. All dimensions are given in µm.

	R_a	R_q	R_z	R_max	R_t
GSGSG	0.64	0.80	3.75	4.04	4.92
GSG	1.35	1.81	5.13	6.61	9.76
LTCC	0.61	0.76	3.55	4.90	4.90

The results of the surface evaluations are given in Table 4.1. For the GSGSG contact pad, the results of the optical microscopy measurement could be reproduced, with a total roughness depth of 4.92 µm. The rms roughness is calculated to a 0.80 µm deviation from the centre line. The fact that these results are strongly correlated to the measurement region is shown by the measurements on the GSG contact pad. There, the total roughness depth is 9.76 µm, while the rms roughness reaches a value of 1.81 µm. However, from the profile measurements it can be seen that the surface roughness of the LTCC material itself is already comparable to those of the gold regions. This concludes that the surface roughness of the gold metallisation is

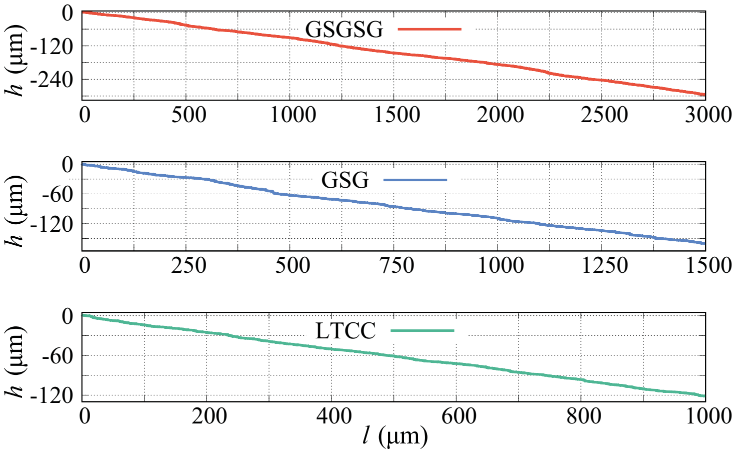

Figure 4.31: Accumulated changes in height of the SPDT32's gold metallisation at the (top) GSGSG and (middle) GSG contact pads. In (bottom) the surface roughness of the LTCC itself is given.

not caused by the screen printing process but by the LTCC material itself.

The more important parameter, however, is the additional path length which the RF signal needs to pass on the metallisation. For the evaluation of the additional path length, the measurement results of the height changes are accumulated as can be seen in Fig. 4.31. The accumulated results reveal a total change of height at the GSGSG contact pad of 295.59 µm over a length of 3000.00 µm, resulting in a percentage change in length of 0.48 %, fitting very well to the assumption made with the help of the optical measurements. The total change in height for the GSG contact pad and the LTCC part is 160.54 µm and 122.49 µm over total lengths of 1800.00 µm and 1000.00 µm, respectively. Thus, the percentage change in length is about 0.57 % at the GSG contact pad and 0.75 % for the LTCC material.

According to simulation, these small changes in length cannot cause this high increase in insertion loss. Hence, the presumption is that the conductivity of the gold paste does not qualitatively match the values of the data sheet. Only a conductivity in the range of $4 \cdot 10^6\,\mathrm{S/m}$ can explain such high losses.

Nevertheless, the high potential of this new type of SPDTs is revealed by Fig. 4.32 and Fig. 4.33, where measurements with varying biasing voltages had been conducted. For the SPDT50 less steps in the biasing voltage had been chosen compared to the SPDT32. The input matching as well as the isolation between adjacent ports are nearly independent of the biasing configuration for both demonstrators.

The signals at the thru and isolated port cannot only be adjusted continuously to each preferred ratio, but also tuned in frequency. This effect is best visible for the isolation, since the change in transmission is not as distinct. Although an interference-based SPDT is system-inherently narrow banded, this frequency selectivity makes it work in a wider frequency range than for a single biasing configuration. For the SPDT32 this results in an isolation of 22.5 dB over a bandwidth of almost 30 %, while the SPDT50 reveals an isolation of 35.0 dB over a bandwidth of 17 %. For both SPDTs isolation values of up to 50.0 dB can be achieved at the resonant points.

By this, the high potential of this new type of SPDT is proven for the application in embedded feeding networks for satellite applications. The increased insertion loss is not limiting the application, since the passive parts can be connected to low noise or power amplifiers. In general, the LTCC technology allows an easy integration and has already been successfully proven at W-band frequencies [Bhu+17]. However, the high ohmic losses of this specifically used LC-LTCC routine are limiting the application at high frequencies. Therefore, other technologies have to be investigated for high-performance applications at W-band.

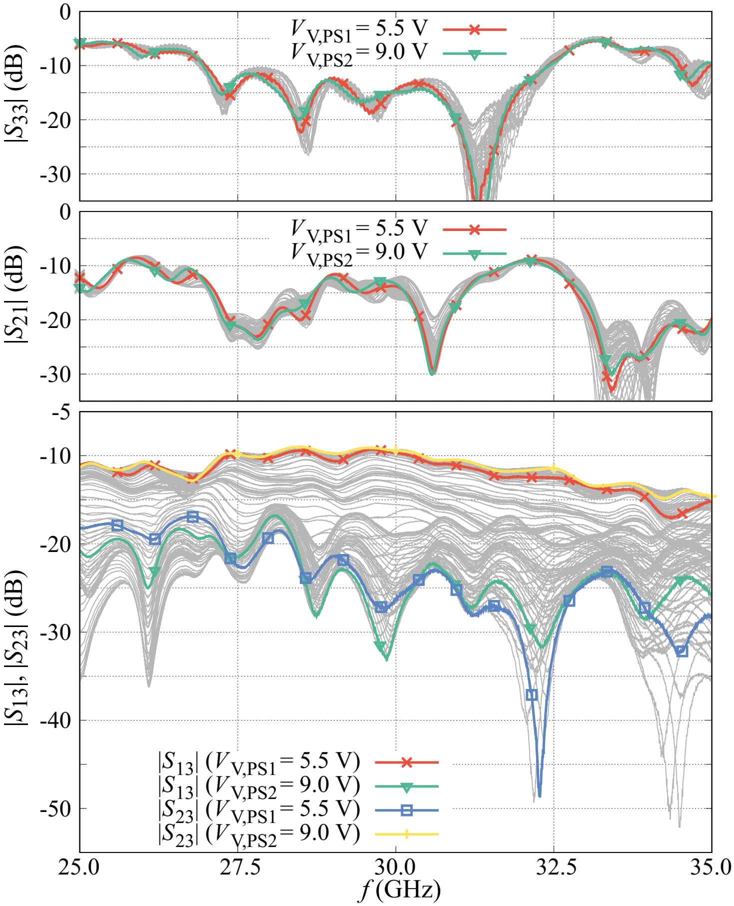

Figure 4.32: Measured best biasing configurations as well as intermediate states of the SPDT32. For the intermediate states, the biasing voltages have been changed between 0 V $\leq V_V \leq$ 80 V in 0.5 V to 10.0 V steps.

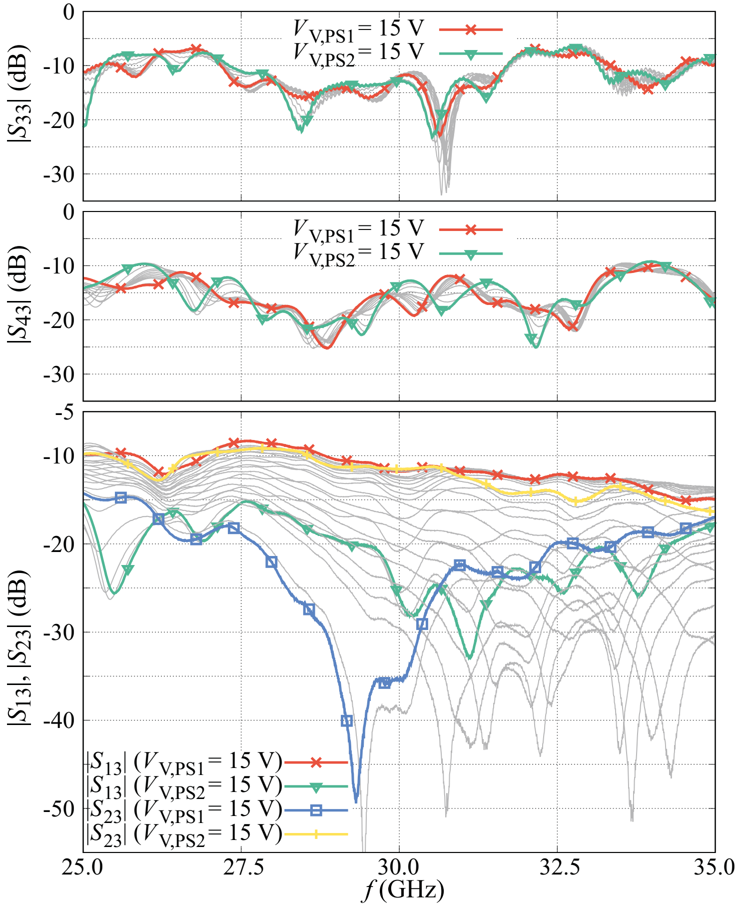

Figure 4.33: Measured best biasing configurations as well as intermediate states of the SPDT50. For the intermediate states, the biasing voltages have been changed between 0 V $\leq V_{\mathrm{V}} \leq$ 15 V in 1 V to 5 V steps.

5 Low-Loss Waveguide-Integrated Butler Matrix and SPDT at W-Band

For the realisation of low-loss beam-steering networks as well as feeding networks for radiometers at W-band and above, passive components are favoured, due to their simple architecture, low power consumption and low-loss behaviour. Waveguides are well established for these purposes, especially at Ka-band. There, the first lightweight continuously beam-steering horn antenna array based on liquid crystal technology was investigated within the project *LISA ES*[1], which was supported by the German Federal Ministry for Economic Affairs and Energy under the lead of the German Aerospace Center [Wei17].

Therefore, in this work, the experience of this well-established LC-waveguide tech-

---

[1] FKZ 50 YB 1113

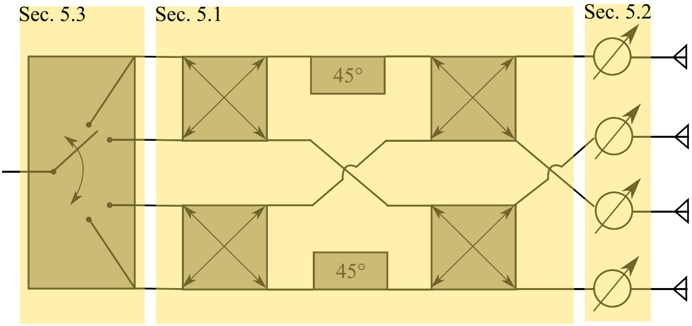

Figure 5.1: Schematic overview of the components investigated in rectangular metallic waveguide topology with corresponding section numbers.

nology for Ka-band is used for the design of the low-loss mixed beam-switching and beam-steering network at W-band. A schematic overview of the investigated components within this chapter is given in Fig. 5.1. First, the Butler matrix and all of its single components, such as the coupled line combiner and the crossover, are discussed. Afterwards, the tuneable phase shifter is introduced as being the key component for the tuneability. In the end, the realisation of a tuneable interference-based SPDT is presented. The focus at the component design for the mixed beam-switching and beam-steering network is on an in-plane fabrication. By this, the overall system can be cost efficiently realised in one step and on one single technology platform. Further, the losses will be reduced to a minimum, since connection points between different components can be avoided, being a non-negligible loss factor at W-band frequencies.

5.1 In-Plane Realisation of a Butler Matrix

As discussed in chapter 3, a Butler matrix is a combination of three non-tuneable components in a certain order: a 45° phase shifter, coupled line combiner as well as crossover. In general, a Butler matrix has a large electrical size, which is why at lower frequencies the focus is on the miniaturisation of the component's large physical size [Che+10; Bon+02; Wan+07; Cha+08]. Since this work focuses on frequencies around 100 GHz, the physical size is not critical in the first step. Therefore, and due to the increasing free-space path loss with increasing frequency, metallic waveguides are preferred for this application. Moreover, an in-plane realisation of a waveguide-based Butler matrix is preferred for keeping the losses at a comparatively low level.

For the aimed in-plane realisation, the required coupled line combiner as well as the fixed phase shifter are sufficiently discussed in literature. The case is different for the crossover. Where the realisation of crossover structures is simple, e.g. for multilayer structures [Liu+12], it can get complicated for waveguides. Either they need to be intricately bended around each other [Rem+06] or several single components need to be connected to each other. Also, in-plane realisations of waveguide-based crossovers are known from literature, based on a double-coupler design [Pio+93]. However, depending on the design, these crossovers can be sensitive to fabrication tolerances, especially for high frequencies.

In the upcoming pages, a novel in-plane crossover design is presented for waveguides which are perpendicularly crossing each other. It is based on a star-shaped dielectric inset, being also able to control the phase shift needed within a Butler matrix by the length of the star's taper sections. Therefore, the fixed phase shifter would not be needed anymore and the Butler matrix design can be reduced to two components. After the discussion of the crossover structure, the realised Butler matrix will be presented including its coupled line combiner.

5.1.1 In-Plane Crossover with Dielectric Inset

First simulations of a conventional waveguide junction with perpendicularly crossing waveguides resulted in maximum forward transmissions $|S_{21}| \approx -2\,\text{dB}$ and a comparatively high transmission to the adjacent, isolated paths $|S_{31}| = |S_{41}| \approx -9\,\text{dB}$. Therefore, if a crossover has to be realised in a conventional junction with perpendicularly aligned branches, the structure needs to be modified to provide a sufficient isolation to the adjacent paths.

The first idea being pursued in this work deals with the precise placement of metallic posts inside the waveguide junction. As a result, the lateral waveguides do not present such a large opening anymore, by which the mode dispersion is suppressed. However, each wave propagating through such a crossover structure faces two metallic posts in the centre of their field strength. Therefore, a compromise has to be found with respect to the diameter of these metallic posts: it has to be small enough to minimally disturb the propagating wave, while on the other hand being large enough to suppress the propagation to the lateral waveguides. A design of such a crossover structure including its simulated field distribution is presented in Fig. 5.2.

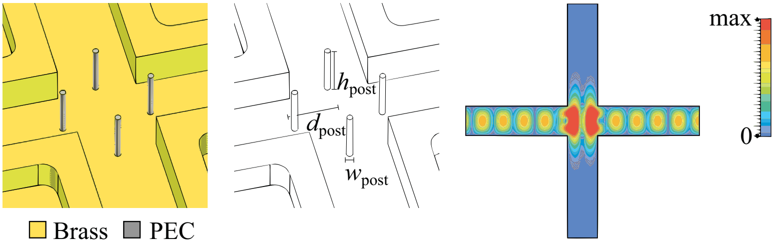

Figure 5.2: Schematic and simulated field distribution of the waveguide crossover based on metallic posts. The field distribution shows that the metallic posts are acting as a resonant structure inside this junction. The given dimensions are $h_{\text{post}} = 1.27\,\text{mm}$, $w_{\text{post}} = 0.20\,\text{mm}$ and $d_{\text{post}} = 1.42\,\text{mm}$.

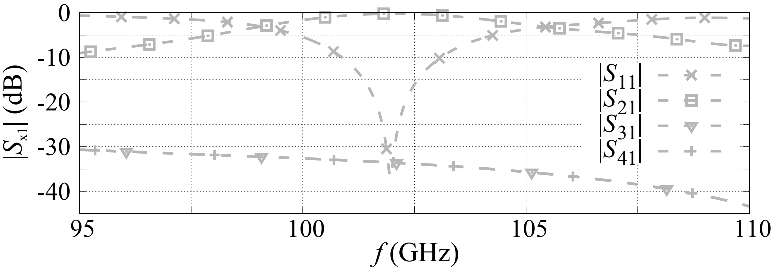

Figure 5.3: Simulation results of the metallic-posts-based crossover structure.

The field distribution displays the mode suppression to the lateral waveguides, but simultaneously, the waveguide crossing became a resonant structure. The simulation results in Fig. 5.3 promise a good performance, but because of the resonator-based behaviour only in a very narrow range. Due to the facts that such a narrow-banded sub-component can limit the use of the large available bandwidth at W-band as well as the high aspect ratio of the metallic posts with very thin diameter, this design is not considered as practical.

Moreover, the focus was set on a more promising design based on dielectric insets. This design is presented in Fig. 5.4. The core component is a star-shaped dielectric, placed in the centre of the waveguide junction in which the propagating wave is

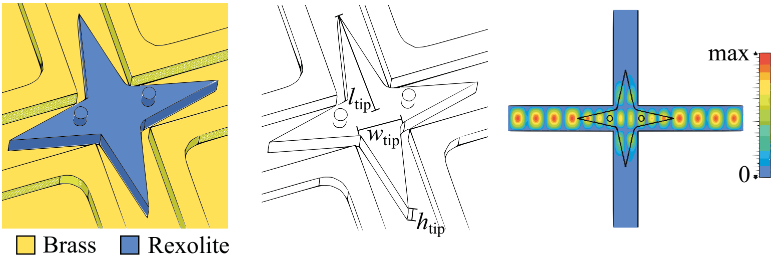

Figure 5.4: Design and simulated field distribution of the in-plane waveguide crossover based on a dielectric star inlet. Only higher order modes can propagate to the lateral waveguides while the first order mode stays focussed in the dielectric. The most important dimensions of the dielectric star are $l_{\mathrm{tip}} = 4.90\,\mathrm{mm}$, $w_{\mathrm{tip}} = 1.93\,\mathrm{mm}$ and $h_{\mathrm{tip}} = 1.27\,\mathrm{mm}$.

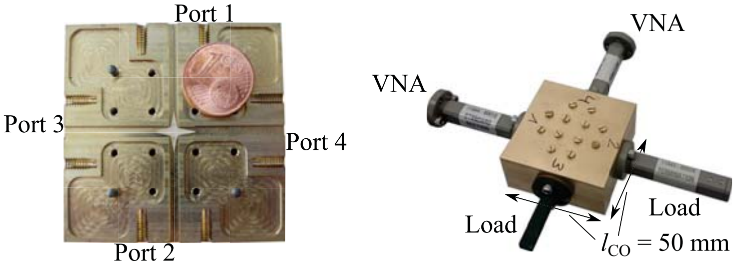

Figure 5.5: (left) Design and (right) characterisation setup of the in-plane dielectrically filled waveguide crossover. The total length of one waveguide branch is $l_{\mathrm{CO}} = 50\,\mathrm{mm}$.

focussed inside. The star's tips are acting as triangular taper for providing a good matching and smooth transition in and out of the dielectric. An important fact is the only partially dielectric filling of the waveguide in width. By remaining air at the side parts of the waveguide, the wave is guided in the dielectric material, similar to dielectric waveguides. Therefore, the propagating wave will not disperse into the lateral waveguides. For keeping the design simple, the metallic waveguide stays with the standard WR10 dimensions of $2.54\,\mathrm{mm} \times 1.27\,\mathrm{mm}$, although it is dielectrically filled. This enables a higher order mode propagation towards the lateral waveguides, which are not propagable outside the dielectrically filled regions. Thus, the generation of higher order modes will not have a significant impact on the overall performance. The star needs to be held in position by register pins also made of Rexolite. Since two pins are already sufficient they are placed in the path from port 1 to port 2, while there are no pins in the path between ports 3 and 4. By this, the impact of the used alignment pins can directly be determined.

The realised demonstrator as well as the measurement setup of the in-plane dielectrically filled waveguide crossover is given in Fig. 5.5. It is fabricated in an asymmetric u-shaped split-block design, whereby the cutting plane is at the upper corners of the short wall. The reason for this is that the complete structure of the mixed beam-switching and beam-steering network should be processable in one milling step at the end, that only a metallic lid needs to be screwed on top, although it is not the best case of split-block design. Current walls have been included for a proper sealing and the dielectric star is milled out of a piece of Rexolite 1422 from C-Lec Plastic Inc. ($\varepsilon_{\mathrm{r}} = 2.53$ and $\tan\delta = 6.6 \cdot 10^{-4}$ at 10 GHz [Inc17a]). It is a well processable hard plastic material with comparable dielectric properties in

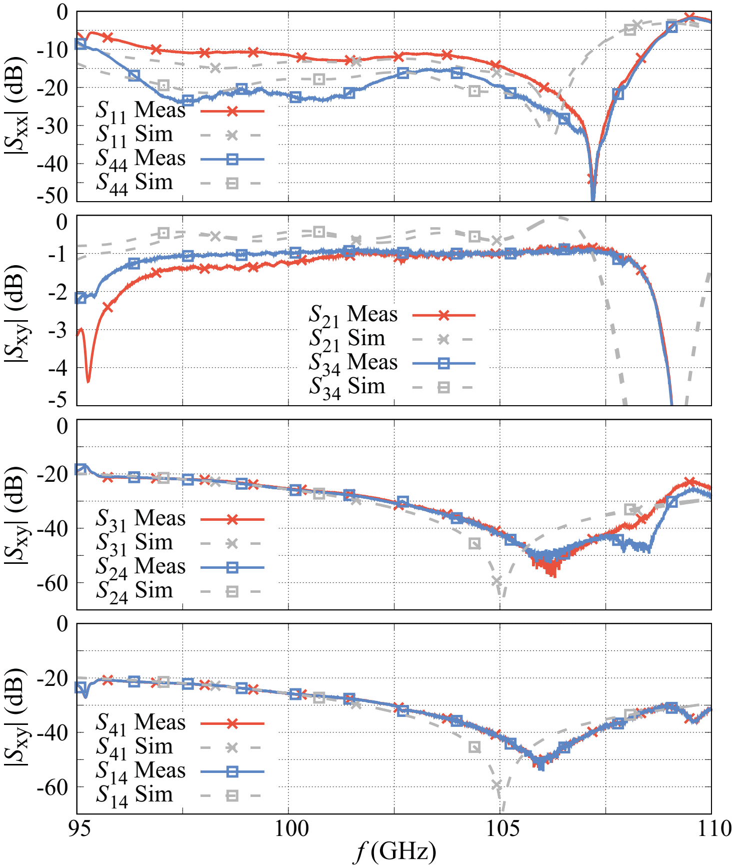

Figure 5.6: Comparison of the S-parameter simulation and measurement results of the dielectrically filled waveguide crossover. For $|S_{21}|$ the register pins are in the transmission path, while for $|S_{34}|$ the alignment pins are in the lateral waveguides.

the W-band [Fri+97]. For the characterisation, the unused ports were terminated by matched loads to avoid unintended reflections while the calibration plane was set directly at the crossover flanges. The results are shown in Fig. 5.6. For the simulation CST Studio Suite was used while a Keysight PNA with two Anritsu 3740A-EW extension modules were used for the characterisation.

The measured results are shifted around 1.0 GHz to 1.5 GHz to higher frequencies compared to the simulation results. Matching is better than -10.0 dB almost over the whole measured frequency range for the path including the register pins and even better than -15.0 dB for the path without register pins. In the best performing frequency range between 106.0 GHz to 108.0 GHz, matching is even better than -20.0 dB. The difference between the transmission coefficients $|S_{11}|$ and $|S_{44}|$ was already predicted by the simulation. The same trend can be made out for the forward transmissions $|S_{21}|$ and $|S_{34}|$. For the path with alignment pins, $|S_{21}|$ is -1.0 dB or better between 101.5 GHz to 108.0 GHz, except a small dip at 102.6 GHz. For the path without alignment pins, $|S_{34}|$ is around -1.0 dB from 98.0 GHz to 108.0 GHz. Hence, the alignment pins are influencing the forward transmission only a little, which was already predicted by the simulation. The isolated ports show values always better than -20.0 dB over the whole frequency range and even down to -50.0 dB in the best performing frequency range around 107 GHz.

These results show that the in-plane waveguide crossover based on dielectric insets is well-suited for a low-loss application in the millimetre wave range. The measurement results are matching the simulations very well. The small deviations are due to the fabrication tolerances of the dielectric star as well as slits, which can occur at the joining walls of the split-block. In future application, the register pins can be replaced by one quadratic register pin being placed in the centre, ensuring symmetric results. Further, by using this crossover in a Butler matrix fixed phase

Table 5.1: Comparison of different state-of-the-art crossovers.

Technology	f (GHz)	IL (dB)	Isol. (dB)	Bandw. (%)	in-plane	REF
Microstrip line	1.8	1.0	< 20	6	yes	[Fen+16]
	3.0	< 0.3	< 25	> 100	no	[Liu+12]
	30.0	< 1.0	< 19	3	yes	[Ye+15]
SIW	35.0	< 1.0	< 15	16	no	[Gun+12]
	60.0	< 0.7	< 20	5	yes	[Dje+09]
Waveguide	**105.0**	**< 1.0**	**> 25**	**8**	**yes**	**This work**

shifters would not be needed anymore, since the phase difference can be easily controlled by the designed taper lengths as will be shown later. The realisation process of complex structures can be simplified by this method significantly and this crossover is in the next step used inside the waveguide-based Butler matrix. Some state-of-the-art crossovers are given in Table 5.1. However, they are not directly comparable, since they operate at different frequencies.

5.1.2 Waveguide-Based In-Plane Butler Matrix

Riblet-Type Coupled Line Combiner

Keeping chapter 3 in mind, the second major component needed for the Butler matrix realisation - beside the crossover - is the coupled line combiner. Despite the fact that this structure, a Riblet-type coupled line combiner, is well known from literature [Rib52; Hil00; RC+07], it should be characterised separately for verification of the split-block fabrication process. Fig. 5.7 shows the design of the coupled line combiner from CST Studio Suite. Both branches are guided together up to $w_{\mathrm{wall}} = 0.2\,\mathrm{mm}$ while the separating wall is left open for the length of one wavelength. In this interacting region, the width between the outer waveguide walls is decreased down to $w_{\mathrm{slit}} = 4.2\,\mathrm{mm}$ for a better wave propagation to the centre of the combiner as well as prevention of a possible propagation of undesired higher order modes.

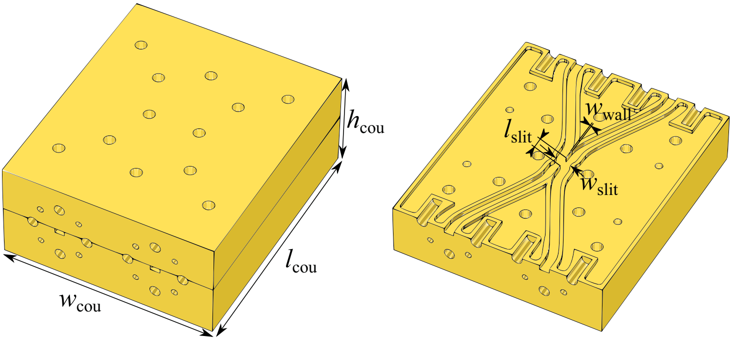

Figure 5.7: Simulation model of the waveguide-based coupled line combiner. The most important dimensions are $h_{\mathrm{cou}} = 26.3\,\mathrm{mm}$, $w_{\mathrm{cou}} = 55.1\,\mathrm{mm}$, $l_{\mathrm{cou}} = 65.0\,\mathrm{mm}$, $w_{\mathrm{slit}} = 4.2\,\mathrm{mm}$, $l_{\mathrm{slit}} = 3.0\,\mathrm{mm}$ and $w_{\mathrm{wall}} = 0.2\,\mathrm{mm}$.

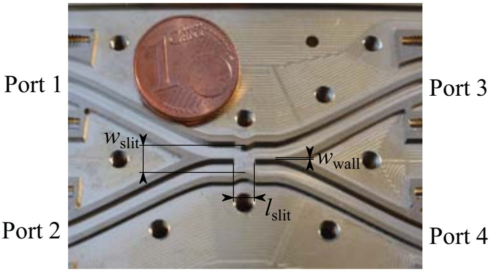

Figure 5.8: Lab demonstrator of the waveguide-based coupled line combiner. The split-block was milled out of brass and the realised dimensions are w_{slit} = 4.19 mm, l_{slit} = 3.10 mm and w_{wall} = 0.19 mm.

The opening of the separating wall is designed with sharp rectangular edges. The final demonstrator is shown in Fig. 5.8.

The complete structure is milled as u-shaped asymmetric split-block out of brass, while the upper part is a plane metallic lid, similar to the aforementioned crossover. Current walls were implemented for a better RF sealing. A comparison of the simulated and measured performance is shown in Fig. 5.9.

The matching $|S_{11}|$ as well as input-to-input transmission $|S_{21}|$ show very low values with −20 dB to −25 dB over a bandwidth of 20 %, fitting the simulation results very well. The forward transmissions are decreased by 1 dB compared to the simulation as well as the ideal case with an equal power split around −4 dB. This insertion loss of 1 dB is due to the finite conductivity of brass as well as possible slits between the joining walls of the split-block. Further, the intersection point of $|S_{31}|$ and $|S_{41}|$ is slightly shifted to lower frequencies, because of the marginally increased length of the coupling slit.

However, the most important parameter for a Butler matrix realisation is the phase difference $\Delta\varphi$ provided by the combiner between both outputs, which is given at the bottom of Fig. 5.9. It is nearly constant over the measured frequency range with values close to 90°. Hence, this coupled line combiner is very well-suited for the later application in a Butler matrix. Especially the effective insertion loss of this combiner is less than measured, since at least half of the losses are originating from the waveguide leading to the flanges, which are needed for the characterisation of this demonstrator.

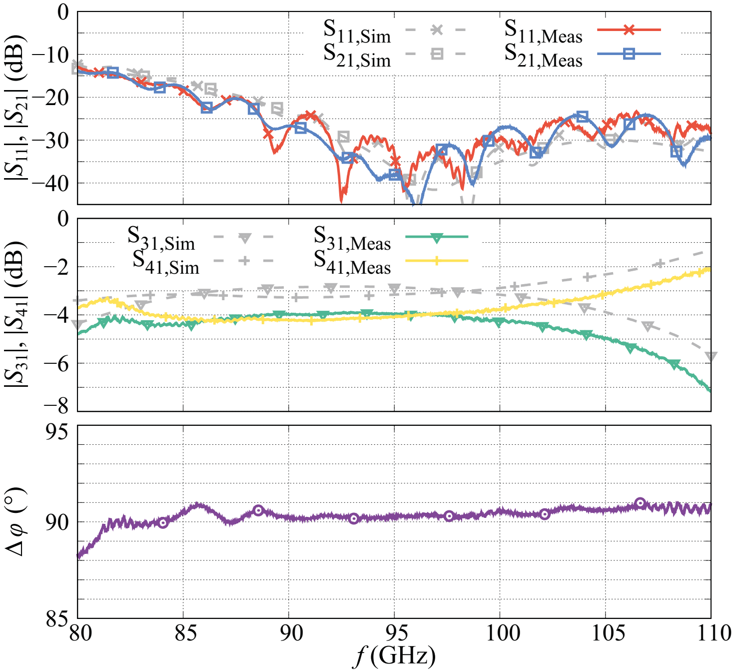

Figure 5.9: Comparison of the simulated and measured results of the waveguide-based coupled line combiner with (top) the matching as well as input-to-input isolation, (middle) the forward transmission and (bottom) the phase difference $\Delta\varphi$ between both outputs.

Butler Matrix

With the knowledge gained from the individual components characterised before, the Butler matrix can now be designed as a combination of both. Although the dielectric star is able to provide the phase shift needed within the Butler matrix, in this demonstrator it is still provided by a bended waveguide structure. This is due to the fact that the working principle of the crossover has first to be proven in a demonstrator before giving it a second task, which might introduce further error sources. The simulation design of the Butler matrix is shown in Fig. 5.10.

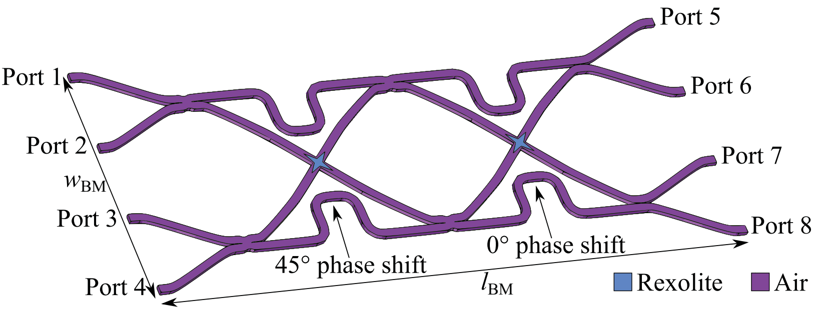

Figure 5.10: Simulation model of the in-plane Butler matrix. The background material of this simulation has been chosen as brass. The given dimensions are w_{BM} = 77.5 mm and l_{BM} = 189.0 mm.

Two crossovers, two 45°-phase shifters as well as four coupled line combiners are needed for the functional principle of a Butler matrix. The width has been chosen to 77.5 mm only because of the WR10 flanges needed for the characterisation. An exemplarily field distribution, showing the division of the input signal at port 1 to four outgoing signals, is presented in Fig. 5.11. From this representation it becomes clear that the power is equally distributed to all output ports. Moreover, this field distribution shows that only a negligible amount of the incoming wave is reflected

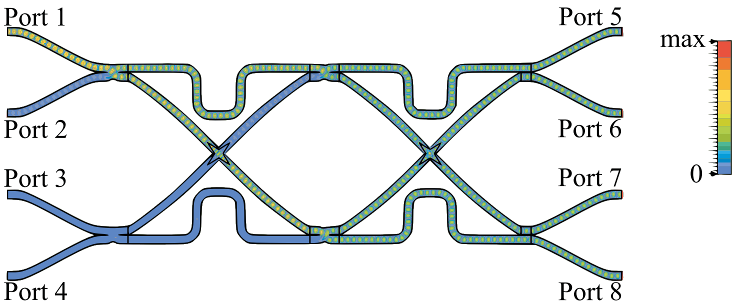

Figure 5.11: Field distribution of the Butler matrix design of Fig. 5.10. Port 1 was selected as excitation port and the simulations were carried out at 100 GHz using CST Studio Suite.

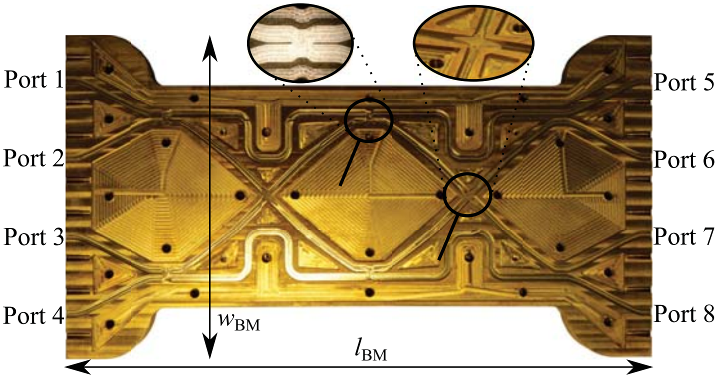

Figure 5.12: Image of the realised Butler matrix demonstrator in split-block technology. The complete structure is milled in the bottom half, while the top part is just a metallic lid.

back to the input ports 2-4. The bottom half of the final demonstrator, including the dielectric stars, is given in Fig. 5.12.

It is fabricated in the same way as the crossover in an asymmetric u-shaped split-block design made of brass. Although the current walls have been implemented, it is very challenging to uniformly seal all the waveguides. For the measurements the unused input ports have been simply left open, since the input-to-input isolations are sufficiently high and reflections within the design are on a low level, as can be seen from Fig. 5.11 as well as the simulation results in Fig. 5.13. On the other hand, the unused output ports needed to be terminated by matched loads. The comparison between the simulated and measured results for an excitation of port 1 are presented in Fig. 5.13 and Fig. 5.14.

The device's matching fits the simulation results well with values always better than $-15\,\text{dB}$ and even down to $-30\,\text{dB}$. Also, the forward transmissions fit the simulations qualitatively well, but quantitatively they show increased losses by $3\,\text{dB}$ with absolute values around $-9\,\text{dB}$ to $-10\,\text{dB}$ at $102\,\text{GHz}$. Those are mainly originating from the u-shaped split-block with the joining walls at the upper corners as well as its assembly. Due to the large size, the RF sealing is very challenging. Since this size is only needed because of the WR10 flanges, the losses will significantly decrease for a later demonstrator, only consisting of combiners and crossovers.

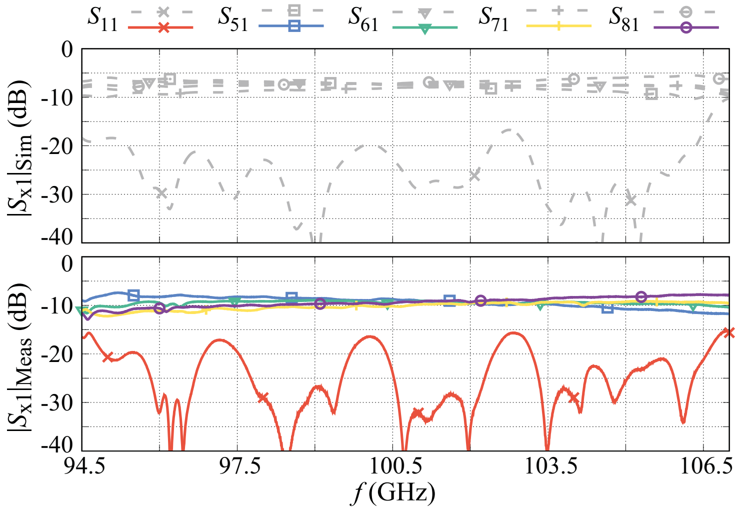

Figure 5.13: Comparison of the (top) simulated and (bottom) measured S-parameter results of the Butler matrix demonstrator, fed at port 1. Simulations are given in dashed and measurements in solid lines.

The progressive phase shift, being the phase difference between two adjacent outputs, is deviating from the simulated results. The frequency of the ideal progressive phase shift is shifted from 102.5 GHz in simulation to 105.5 GHz in measurement. Further, the progressive phase shifts are not overlapping all together at the same frequency, as simulated. It is assumed that those deviations are based on possible fabrication tolerances of the dielectric stars. Especially for the progressive phase shift, it is obvious that the deviations compared to simulation are arising from the different numbers of passed crossovers of both signals. For example, the signal measured at port 6 has to pass 2 crossovers, while the signal measured at port 5 is not passing any crossover. Therefore, the deviation of the progressive phase shift between port 5 and 6 is comparatively high, while the measured progressive phase shift between the ports 7 and 8 is matching the simulation well, since both signals are passing one crossover. Hence, the phase is very sensitive to fabrication tolerances at the dielectric stars. The same tolerances can also cause a shift in frequency.

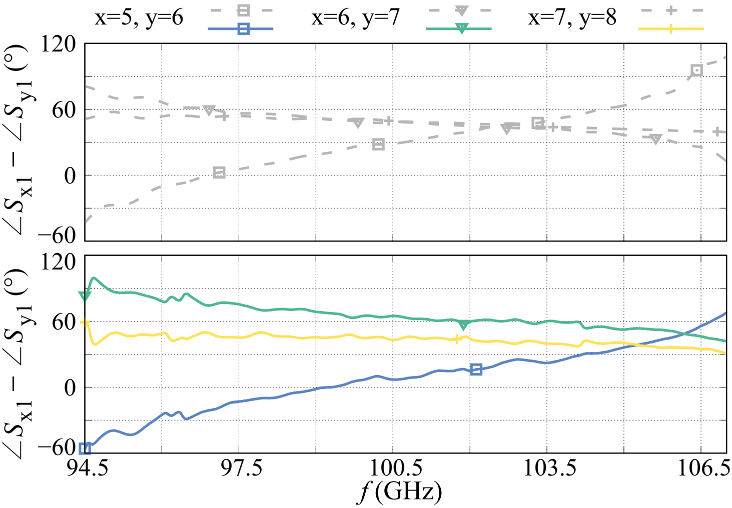

Figure 5.14: Comparison of the (top) simulated and (bottom) measured progressive phase shift of the Butler matrix demonstrator, fed at port 1. Simulations are given in dashed and measurements in solid lines.

However, this effect can also be used for replacing the fixed phase shifters by precisely adapt the length of the star's tip lengths. In Fig. 5.15 the phase of a wave propagating along a straight waveguide is compared to the one of a wave crossing the dielectric star. The tip length l_{tip} of the star is varied for this from 4.4 mm to 5.4 mm. There it can be seen that a change in length of 0.1 mm causes a phase change of 12.5°, being directly linked to a frequency shift of around 0.5 GHz. Even small frequency shifts for single signals can cause a higher frequency shift for the overall component, since all four phases need to have a specific relation to each other.

The simulated and measured results for an excitation of port 2 are compared in Fig. 5.16 and Fig. 5.17. Also, for port 2, the matching is better than −15.0 dB from 95.0 GHz on. The forward transmission is a bit worse compared to port 1 with values between −9.0 dB to −10.0 dB at 102.0 GHz. The frequency of the ideal/theoretical progressive phase shift is shifted in frequency as well and the same tendency between measurement and simulation as for the excitation at port 1 can be made out. It is also based on fabrication tolerances of the dielectric stars.

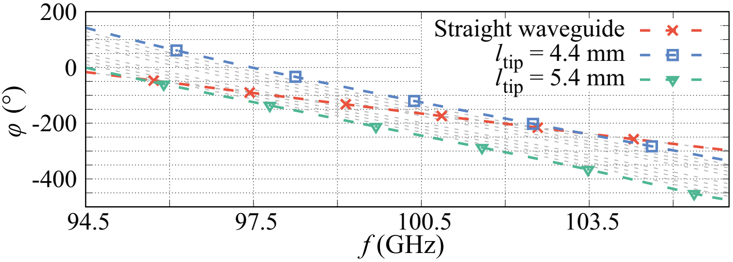

Figure 5.15: Simulated phase change depending on the length l_{tip} of the dielectric star's tip. The length is increased from 4.4 mm to 5.4 mm in 0.1 mm steps. It is compared with the phase of a wave propagating through a straight waveguide with fixed length.

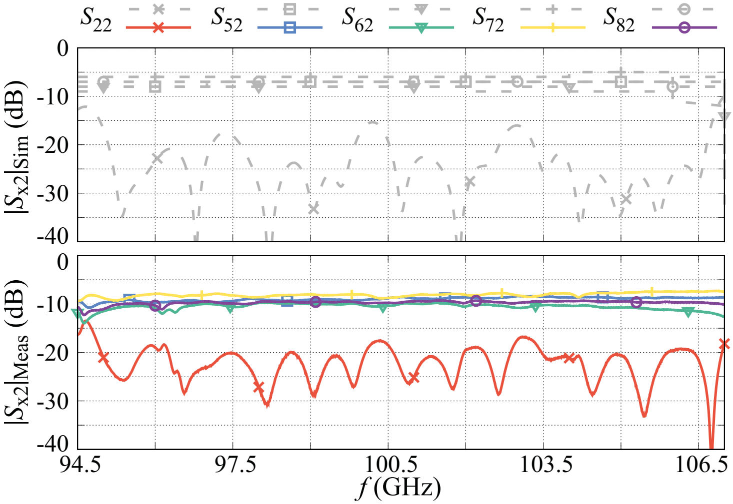

Figure 5.16: Comparison of the (top) simulated and (bottom) measured S-parameter results of the Butler matrix demonstrator, fed at port 2. Simulations are given in dashed and measurements in solid lines.

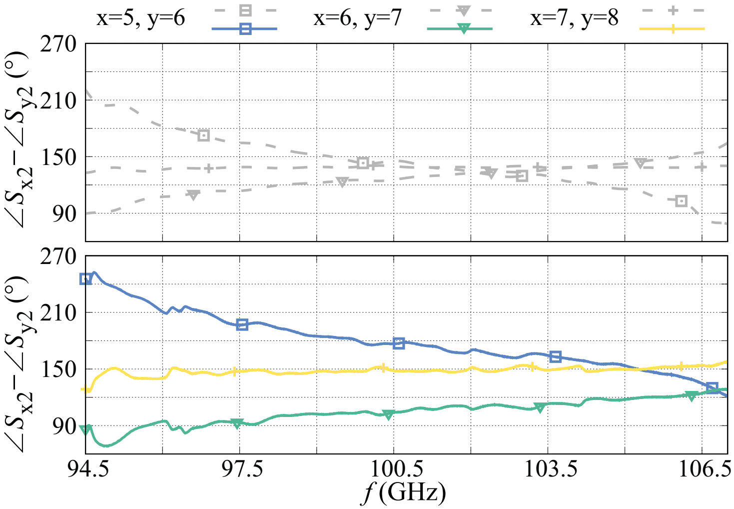

Figure 5.17: Comparison of the (top) simulated and (bottom) measured progressive phase shift of the Butler matrix demonstrator, fed at port 2. Simulations are given in dashed and measurements in solid lines.

However, these are very promising results for the later realisation of an in-plane tuneable Butler matrix. When the complete waveguide structure is fabricated in a single piece/step, the design of the Butler matrix can be reduced significantly, as shown in Fig. 5.18. The fixed 45°-phase shifters can be left out by slightly changing the tip length of the first dielectric star. Also, the WR10 flanges had only been needed for a separate characterisation of the Butler matrix and can be left out in the final network. The size of this compact Butler matrix is nearly 13 times reduced compared with the initial design, and therefore, as small as a matchbox. According to the simulation, the losses of the transmitted signals will reduce from average 6.6 dB down to 6.2 dB, and thus, by 66 % at the equal power split, since they only have to propagate through a much shorter waveguide. Further, the compact demonstrator will be better sealable, which will also reduce the loss compared with the presented demonstrator.

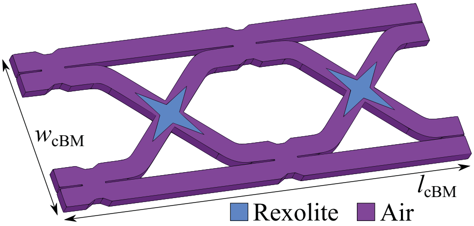

Figure 5.18: Simulation model of a compact Butler matrix design without WR10 flanges as well as fixed phase shifters. The overall dimensions can be reduced down to $w_{\text{cBM}} = 21.4\,\text{mm}$ and $l_{\text{cBM}} = 53.8\,\text{mm}$.

5.2 Tuneable Low-Loss Phase Shifter

The aforementioned Butler matrix represents the non-tuneable core of the aimed mixed beam-switching and beam-steering network. Now, tuneable components have to be investigated. As proof-of-concept for the usability of tuneable LC devices at W-band frequencies, a waveguide-based phase shifter has been investigated in detail. Simultaneously, the challenges of the tuneable LC technology at these high frequencies were supposed to be determined. The basic concept had been oriented to the preliminary demonstrators realised in the Ka-band [Gae+09; Wei+13b].

5.2.1 Magnetically Biased Phase Shifter

Design & Realisation

For this phase shifter demonstrator, an asymmetric split-block design was chosen, simplifying the exchange of LC cavities for characterisation. The split-block is made of brass and the waveguide itself has an u-shape with a cover, which is pressed on top by screwing. Although the joining walls are at the upper corners of the waveguide where the wall currents are flowing perpendicular to the propagation directions, it is the best trade-off for a press-fit sealing of the LC cavity. Due to the dielectric filling of the waveguide, it is tapered to the dimensions of $1.6\,\text{mm} \times 0.8\,\text{mm}$. The waveguide shows two metallic steps at each side of the tapered section, acting as $\lambda/4$-transformer, as can be seen in Fig. 5.19.

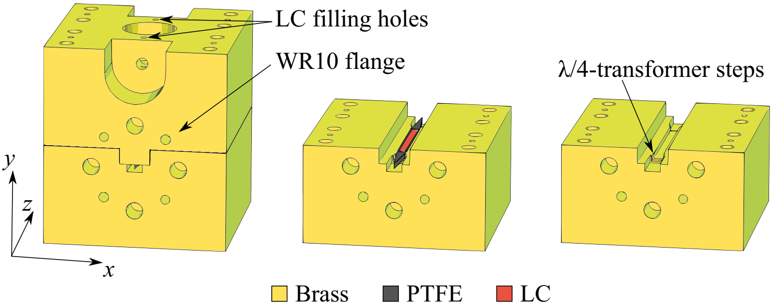

Figure 5.19: Schematic of the waveguide phase shifter design. It is designed in an asymmetric split-block technology with an PTFE container acting as LC cavity. Quarter-wave transformer have been included to the metallic tapering for a better matching.

The LC cavity is made of polytetrafluoroethylene (PTFE), since its elasticity allows a press-fit dielectric filling of the waveguide. Further, it shows a very low dielectric loss with $2.2 \cdot 10^{-4}$ at 100 GHz [Hir+96]. The container has a dielectric taper with a length of 8.3 mm on each side. Based on the investigations made in the Ka-band, LC is only filled in the centre part of the container, since the major part of the RF field is focussing there, which is why the outer regions are not significantly contributing to the tuneability [Gae15], and therefore, the FoM. Hence, to keep the losses on a low level, the side parts of the waveguide are filled with the low-loss PTFE instead of LC.

The container is placed in the waveguide before being filled with LC. After closing the split-block, the filling process is done under normal conditions with the help of a syringe. By using this filling system shown in Fig. 5.20, LC can be "flushed" through the cavity, reducing the possibility of air bubbles inside the cavity. The holes from the filling system to the inside of the waveguide are designed with a diameter of 0.6 mm. The cut-off frequency of these holes is above the measured frequency range, avoiding any RF leakage towards the filling system. Register pins are used as cross stopper for sealing the filling system at the top.

The phase shifting section is designed with a width of 1.0 mm and a length of 14.6 mm. Assuming an ideal alignment of LC, the length is supposed to be sufficient for providing a phase shift of more than 360°.

The realised demonstrator is shown in Fig. 5.21. All components have been pro-

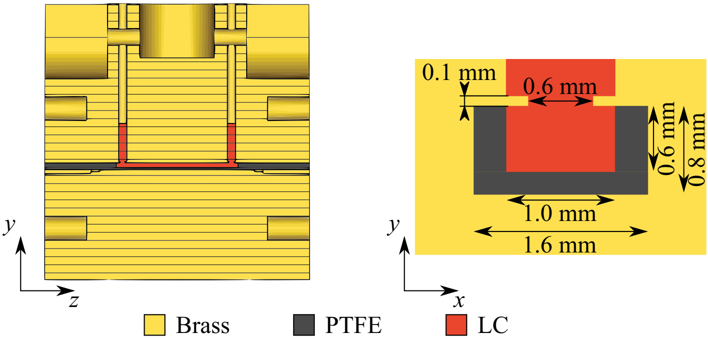

Figure 5.20: Schematic cross-section of the filling system as well as the LC cavity. The cavity is filled after closing the split-block through the filling holes. Due to the press-fit sealing of the PTFE container, LC cannot leak.

cessed by milling. Due to the flexibility of PTFE, the triangular taper are slightly varying in length. However, the cavity length as well as the container height could be controlled precisely. Also, the metallic taper steps are accurately realised. The only difference to the design is the small radii of the corners, due to the finite dimensions and circular shape of the used milling head.

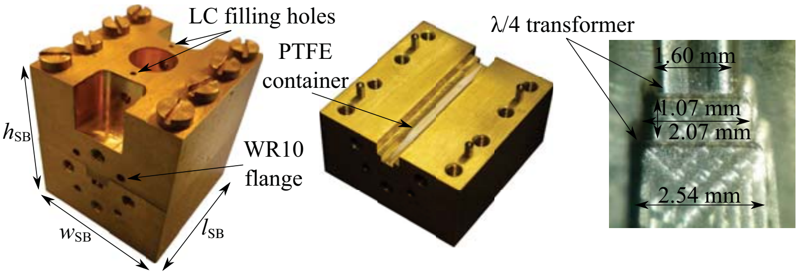

Figure 5.21: Photographs of (left) the assembled waveguide-based LC phase shifter, (middle) the split-block bottom including the PTFE container as well as (right) the metallic taper of the split-block bottom. The split-block dimensions are h_{SB} = 33.0 mm, w_{SB} = 30.0 mm and l_{SB} = 31.6 mm.

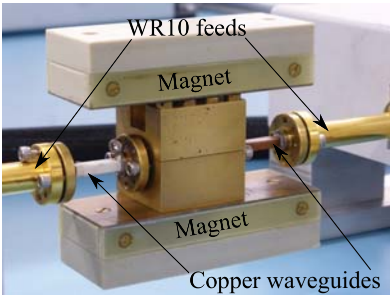

Figure 5.22: Measurement setup of the waveguide-based LC phase shifter. The phase shifter is magnetically biased and fed by mixer modules with WR10 extensions.

Characterisation

For a fast first proof-of-concept procedure, the phase shifter is only magnetically biased. The realisation of an electrical biasing system will be subsequently discussed. The measurement setup, including the WR10 feeds as well as the biasing magnets is shown in Fig. 5.22. The measurements were carried out by an Anritsu 37397C VNA combined with two 3740A-EW mixer modules with WR10 extensions. The comparison of the simulated and measured S-parameter results for both extreme orientations of the LC is given in Fig. 5.23. For preventing the VNA of any LC leakage, additional standard copper waveguides with a length of 30 mm have been added to each side of the phase shifter.

The phase shifter is only matched in a narrow band around the design frequency with values of around -10 dB over a bandwidth of 8 %, due to the utilised quarter-wave transformer steps. According to the simulation, the matching should be 3 dB to 5 dB lower.

The measurements are also deviating from the simulation for the transmission. There, the values of $|S_{21}|$ are about 1 dB worse than simulated. Further, the overall transmission is very rippled in the measured frequency range for both orientations, being a hint for standing waves inside the phase shifter. Moreover, at around 108 GHz a resonance is visible. However, $|S_{21}|$ is higher than -3 dB over a bandwidth of 13 %. Compared to the simulated results, these increased losses comprise mainly from the slit of the split-block, interrupting the flow of current at the upper

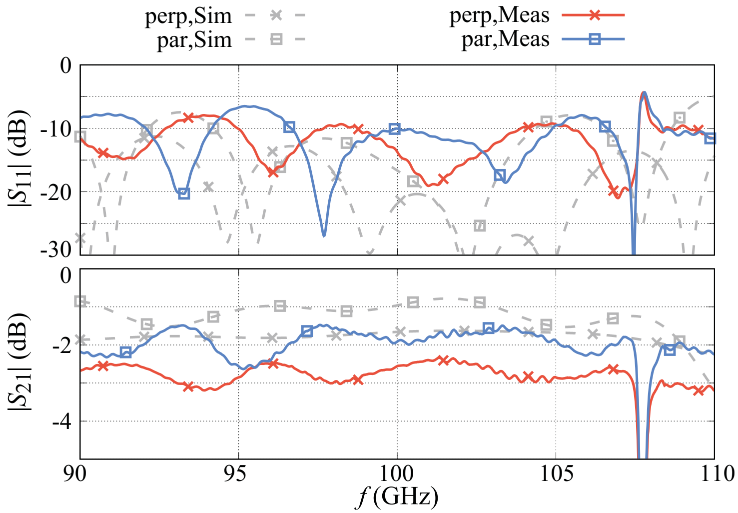

Figure 5.23: Simulated and measured S-parameter results of the magnetically biased waveguide-based LC phase shifter. The simulations were carried out with CST Studio Suite.

edges, if it is not perfectly sealed. The resulting phase shift as well as the FoM are shown in Fig. 5.24.

The provided phase shift also has a rippled shape, due to the standing wave propagation inside. Nevertheless, the overall trend is increasing with frequency. It reaches values from around 290° around 92 GHz to 330° at 110 GHz, being 60° to 90° less than simulated. This deviation arises from the ideal conditions in the simulation with CST Studio Suite, where a perfectly parallel and perpendicular alignment of the LC was assumed. This cannot be reached, even not by magnetic biasing, since surface anchoring acts contrary to the magnetic force. Further, the press-fit sealing of the PTFE causes a bending of the container walls to the inside, decreasing the volume of the cavity, and therefore, the amount of LC inside.

Despite all these deviations, the phase shifter reaches an FoM between 105 °/dB to 148 °/dB from 90 GHz to 107 GHz, being an outstanding value for phase shifters in this frequency range, as can be seen from Table 3.1. Although only magnetic biasing was used, these values reveal the high potential of this low-loss technology for the

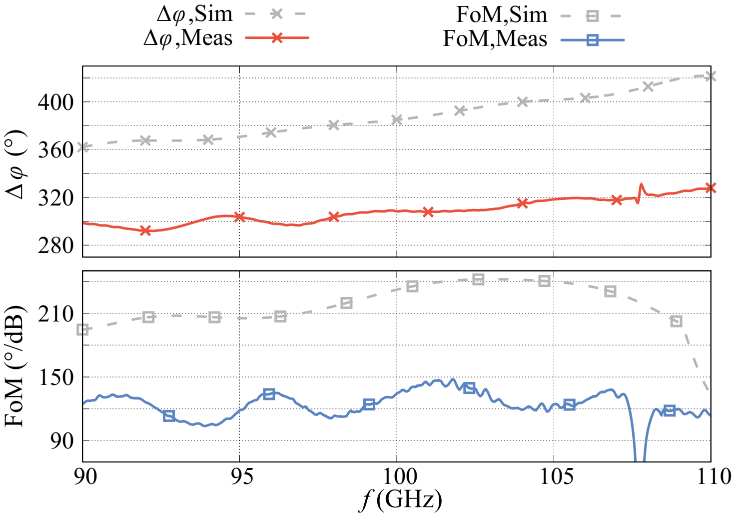

Figure 5.24: Simulated and measured phase shift and FoM of the magnetically biased waveguide-based LC phase shifter. The simulations were carried out with CST Studio Suite.

realisation of tuneable components in the millimetre wave regime.

5.2.2 Biasing Electrode Design

The implementation of an electrical biasing network is very challenging at W-band. Not only that the high frequency entails small dimensions of the waveguide, they are further decreasing due to the dielectric filling. Within this work, the realisation of biasing electrodes on PET films, similar to the Ka-band approach in [Gae+09] or [Wei+13b], has been investigated. First simulations with the director dynamics simulation tool *SimLCwg* were carried out to determine an electrode design for a sufficient LC alignment. Because of the used filling system no electrode is allowed to be in the centre of the top substrate. Thus, only an even number of electrodes is allowed. The limited width of 1.6 mm is constraining the number electrodes. Four pairs of electrodes are too challenging for the realisation, since stepped impedance

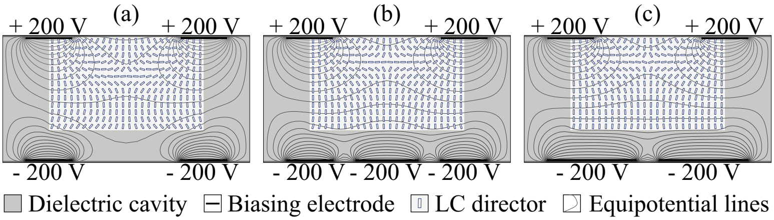

Figure 5.25: Comparison of three different biasing electrode configurations simulated for the parallel state by *SimLCwg*. (a) Two pair of electrodes are used, while (b) an additional electrode was added to the bottom substrate. (c) The two-pair electrode simulation has been carried out with wide bottom electrodes.

structures are needed as described later. A comparison of different configurations of biasing electrodes is given in Fig. 5.25.

The parallel case for each electrode configuration is shown, since it is the more critical case due to the missing pair of electrodes in the centre. All configurations provide a sufficient quadrupole field, however, there is an area where the LC is aligned rather perpendicular than parallel for each configuration. For the two equal pairs of electrodes this part is in the centre of the LC cavity, while it is shifted to the top of the cavity by using 3 or 2 wide bottom electrodes. The calculated propagation constants for both orientations are given in Table 5.2.

Topology (a) provides the highest differential phase constant $\Delta\beta$, although the perpendicularly aligned LC is in the centre of the cavity. Furthermore, this topology is also best suited for the complete perpendicular alignment of the LC. Thus, the differential phase shift of it was calculated to 13 928 °/m, resulting in a length of 25.8 mm for a phase shift of 360°. However, with the ideal LC alignment assumed by CST Studio Suite a differential phase shift of 26 369 °/m is possible, by which only

Table 5.2: Simulated propagation constants for the topologies shown in Fig. 5.25. The simulations were carried out with *SimLCwg*.

Topology	$\beta_{\parallel}(1/\mathrm{m})$	$\beta_{\perp}(1/\mathrm{m})$	$\Delta\beta(1/\mathrm{m})$
(a)	2872.9	2629.8	243.1
(b)	2833.5	2632.8	200.7
(c)	2843.3	2641.3	202.0

a length of 13.7 mm is required for a 360° phase shift. Hence, the relative steering efficiency of the proposed electrically biased phase shifter is only about 53 %, being based on the limited number of realisable electrodes within the limited width of 1.6 mm.

The response time of topology (a) was calculated for an applied biasing voltage of ±200 V (see Fig. 5.26). Due to the decreased waveguide dimensions compared to Ka-band, the response times are comparatively fast for waveguide-based LC phase shifters. For the case from perpendicular to parallel alignment it was simulated to $\tau_{90\,\%}^{10\,\%} = 1.6\,\mathrm{s}$. From parallel to perpendicular alignment a marginally longer time is needed with $\tau_{10\,\%}^{90\,\%} = 1.8\,\mathrm{s}$, being due to the bigger distance between the electrodes compared to the parallel case.

To be able to suppress a possible propagation of stripline modes between the biasing electrodes and the waveguide wall, the substrate material needs to be chosen as thin as possible to decrease the impedance of this microstrip line, while the biasing electrodes need to be mismatched by means of stepped impedances [Wei+13b]. In this work, a 20 µm thick PET film was chosen as substrate material with different metallisations. The result for chromium electrodes, designed according to the above-mentioned design criteria, are given in Fig. 5.27. According to the simulation, this thin substrate in combination with the stepped impedance structure is sufficient for the suppression of the stripline mode. However, it can be seen that the substrate material is very sensitive to the process steps of metal evaporation and photolithography, which is the reason for the visible microscopic cracks. They originate in the high vacuum melting temperature of 1920 °C of the chromium, which makes the

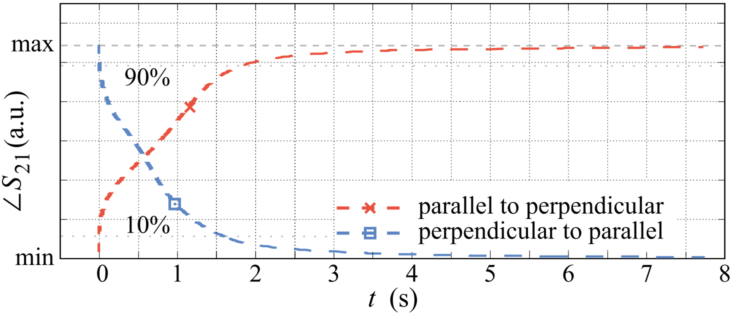

Figure 5.26: Simulated response time of topology (a) of Fig. 5.25, carried out with *SimLCwg*. A voltage of ±200° was assumed for biasing.

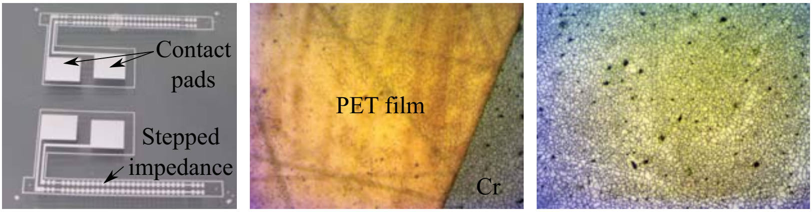

Figure 5.27: Photograph and microscopy of the first realised biasing electrodes for the use in a waveguide phase shifter based on LC. The electrodes are made of chromium and processed on a 20 µm thin PET film.

PET film expand during evaporation and shrink while cooling. Further, the thin PET film cannot withstand the contacting with spring probe pins.

Due to all these challenges, a new technology for the realisation of electrically tuneable low-loss LC components for W-band frequencies needs to be investigated. However, in the next section, a magnetically biased proof-of-concept waveguide SPDT is introduced first, to prove the high potential of the interference-based SPDT at W-band. Further, it will serve as reference for the new technology to be investigated.

5.3 Low-Loss Single-Pole Double-Throw

To prove the high potential of tuneable waveguide components at W-band, a magnetically tuneable SPDT has been realised as being needed for the port selection at the input of a Butler matrix. The design is as well based on the interference principle and the general concept is shown in Fig. 5.28. There, completely sealed LC cavities need to be included to both separated branches.

Design & Realisation

The lab demonstrator of this SPDT is designed in symmetric split-block topology. However, to keep the loss of the split-block on a low level, it is cut across the H-plane with the cut in the E-plane. By this, the joining walls are in the centre of the broad wall where the wall currents are flowing in propagation direction. Hence, the loss due to a small slit between the joining walls is nearly negligible at this point of the

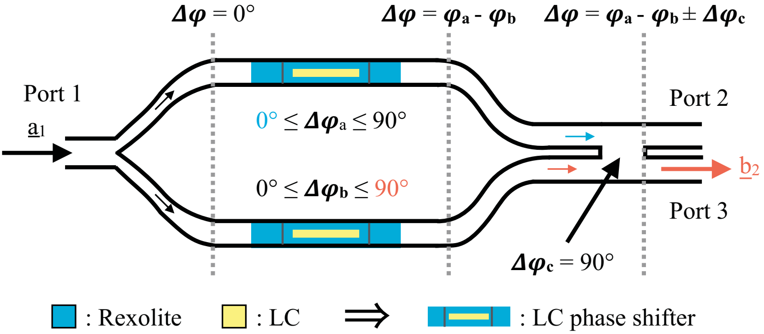

Figure 5.28: Schematic concept of the interference-based waveguide SPDT. A cavity filled with LC is included to each of the two waveguide branches.

waveguide. Based on this design criterion, an E-plane power divider as well as coupled line combiner are designed.

For reasons of integration and the fact that the split-block slit is placed in the centre of the broad waveguide wall, the filling system of the preceding phase shifter has been left out, also for reducing the number of discontinuities at the inner waveguide walls. Therefore, a completely sealable LC cavity needs to be designed based on another material than PTFE, since it cannot be glued for sealing. Hence, Rexolite is chosen as the new LC cavity material, which can be easily glued.

The Rexolite containers are designed in two pieces, where the LC cavity is drilled inside the main body. Prevention of LC leakage as well as mechanical stability were the main focus areas of the container design. For sealing, the second taper section is glued on top of the main body after the filling. For this, a commercially available cyanoacrylate adhesive was used. Afterwards, the containers can be put inside the waveguides, where they are kept in position by two alignment pins with diameters of 0.6 mm, also made of Rexolite.

Since this demonstrator is solely magnetically biased in the first step, the branches need to be separated sufficiently after power division to provide enough space in between for placing the biasing magnets. A simulation model from CST Studio Suite can be seen in Fig. 5.29.

It is obvious from this schematic that the waveguide sections in the dielectrically filled branches have not been tapered to smaller dimensions, although this is caus-

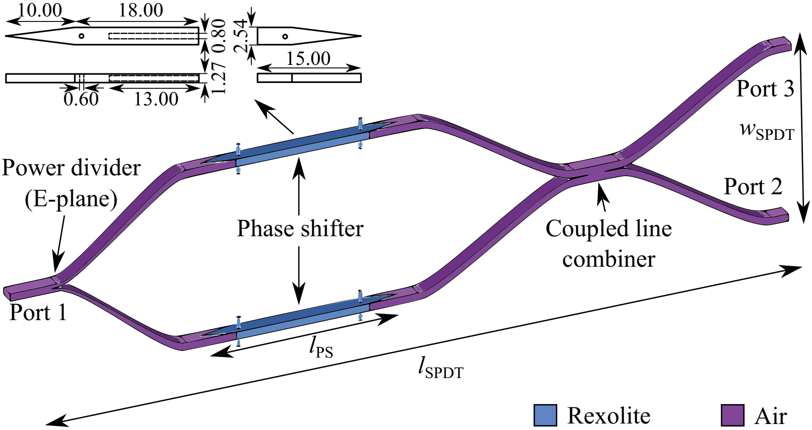

Figure 5.29: Simulation design of the tuneable waveguide SPDT in CST Studio Suite. As background material brass was chosen. The most important dimensions are w_{SPDT} = 31.27 mm, l_{SPDT} = 135.00 mm and l_{PS} = 34.00 mm. Dimensions given in the figure are in mm.

ing higher order mode propagation. The reason for this had been that standing waves occurred in the simulations when these metallic taper sections were included. These standing waves have a higher impact on the overall performance than the higher order mode propagation inside the dielectric filled sections, especially because these modes are not propagable outside the dielectric anymore. Hence, the marginally increased dielectric loss due to the missing metallic taper is accepted. For visualisation of the working principle, a field distribution of the best biasing configuration, where the phase shifters are de-tuned by 90° to each other, is given in Fig. 5.30.

The realised split-block as well as the Rexolite containers in Fig. 5.31 were processed by milling. Only the LC cavities inside the Rexolite's main bodies were drilled. Current walls were included to the split-block design to ensure a proper sealing of the inner waveguide. Due to the very precisely realised walls of the power divider and combiner, the split-block halves need to be held in position by means of alignment pins.

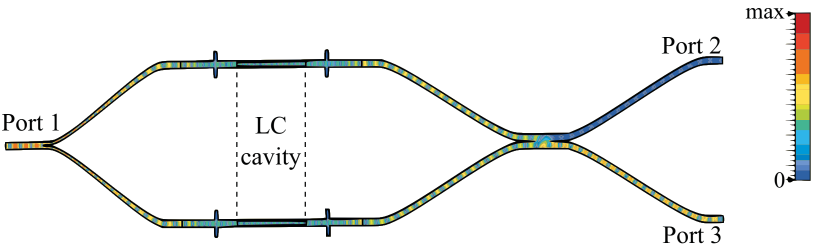

Figure 5.30: Simulated field distribution of the tuneable waveguide SPDT for the best biasing configuration at 95 GHz. The phase shifters are de-tuned by 90°.

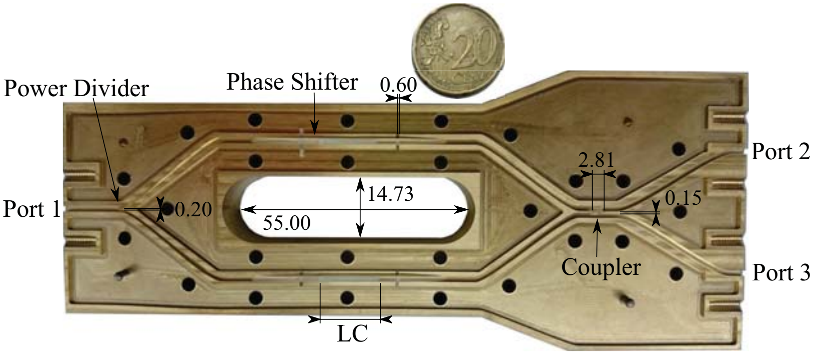

Figure 5.31: Realised demonstrator of the tuneable waveguide SPDT. The already filled and sealed phase shifters have been included to the bottom part of the split-block. All given dimensions are in mm.

Characterisation

Not only the tuneable SPDTs but also the phase shifters as well as the empty SPDT were separately characterised. A phase shift supply of 90° is mandatory for the use of the phase shifters in the SPDT. For this purpose, a second split-block bottom half for the setup in Fig. 5.22 was designed, which basically stays with the WR10 dimensions. The holes of the filling system might influence the measurement results but, however, only the applied phase shift is of interest for the later application. The measurements for the phase shifter as well as SPDT demonstrators are carried

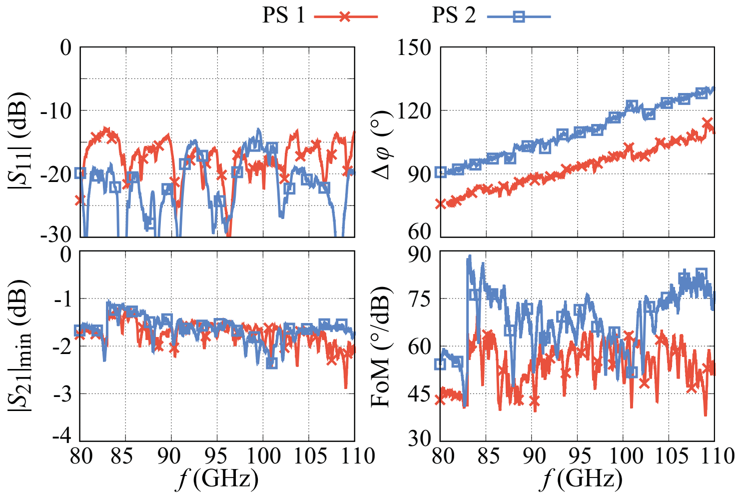

Figure 5.32: S-parameter measurement results, applied phase shift as well as phase shifter FoM for both phase shifters used in the tuneable waveguide SPDT.

out using a Keysight PNA with two Anritsu 3740A-EW extension. The measured phase shifter results are presented in Fig. 5.32. Magnets have been used for the LC orientation.

While both phase shifters show a good matching with $|S_{11}| < -13\,\mathrm{dB}$ over the complete frequency range, they exhibit minimum transmission coefficients $|S_{21}|_{\min}$ between $-1\,\mathrm{dB}$ to $-2\,\mathrm{dB}$ in average. The very rippled shape of these results is due to the higher order modes. Such phase shifters would not preferably be used in communication systems, due to their non-constant group delay. Nevertheless, both phase shifters exceed the needed phase shift of 90°. Phase shifter 2 (PS 2) applies a sufficient phase shift all over the measured frequency range, while phase shifter 1 (PS 1), exceeds the phase shift of 90° from 94 GHz on. Despite the increased loss due to the higher order mode propagation, these phase shifters still have an average FoM between 50 °/dB to 70 °/dB. These decreased performances compared with the phase shifter presented in the section before had been expected due to the missing metallic taper.

The measurement setup of the tuneable waveguide SPDT is given in Fig. 5.33. First,

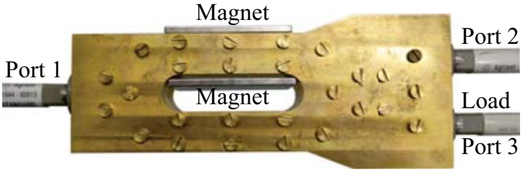

Figure 5.33: Measurement setup of the tuneable waveguide SPDT. Two pairs of rare earth permanent magnets were used for biasing, while the unused port was terminated with a matched load.

the split-block was measured completely empty for the evaluation of the milling as well as assembly process. The results are given in Fig. 5.34. The measured matching fits nearly perfectly to the expected values from simulation. Compared to the simulation an equal power split of −4.2 dB was only achieved at 80.0 GHz, while the difference in transmission coefficients $|S_{21}|$ and $|S_{31}|$ are about 0.5 dB at higher frequencies. These deviations can occur if the thin walls of the power divider or combiner are slightly bended to one side due to the milling process or if the split-block halves are slightly shifted to each other.

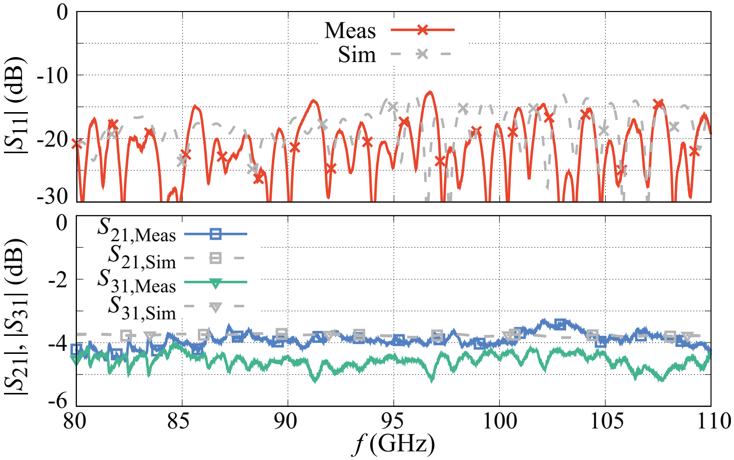

Figure 5.34: Simulation and measurement results of the empty SPDT split-block.

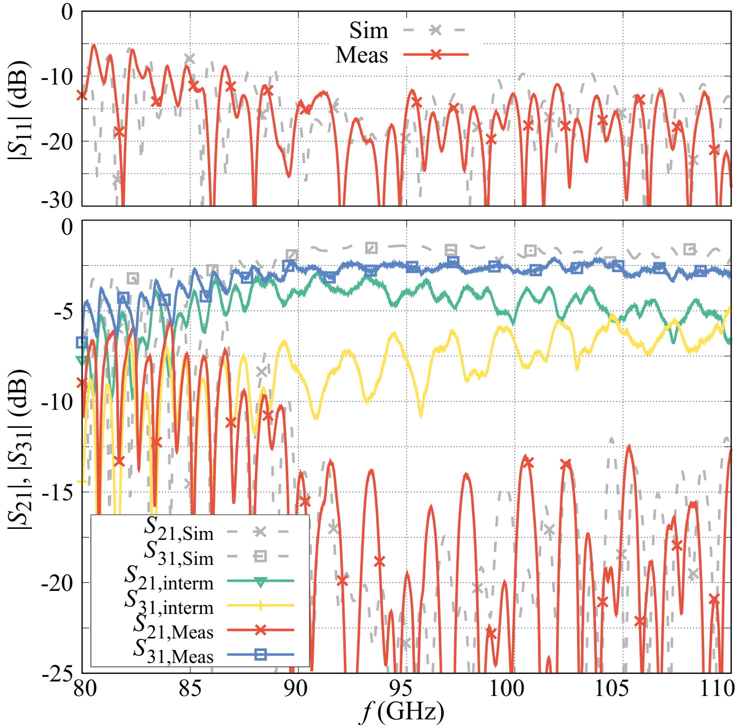

Figure 5.35: Simulation and measurement results of the tuneable waveguide SPDT. For the measurements two pairs of magnets were used for biasing.

A comparison of the simulated and measured results for the tuneable waveguide SPDT are given in Fig. 5.35. One of the two best biasing configurations is shown, where the SPDT was tuned to the state of the maximally achievable isolation and transmission at port 2 and 3, respectively. For this, the LC in PS 1 needs to be oriented parallel, while PS 2 is oriented in between the parallel and perpendicular orientation, since this phase shifter provides more than enough phase shift. For this, the magnets were tilted slightly. Also, for the tuneable version, the matching perfectly fits the simulation with values better than $-12.0\,\mathrm{dB}$ from $88.0\,\mathrm{GHz}$ on. Further, it can be seen that this best biasing configuration shows a transmission coefficient $|S_{31}| > -3.0$ dB, being around 1.0 dB worse than simulated. Port 2 shows a transmission $|S_{21}|$ below -12.5 dB in the design frequency range above 89.0 GHz and even down to -20 dB between 94.0 GHz to 96.0 GHz. This results in an output-to-output isolation of 9.5 dB to 17.0 dB, being in a good agreement with the simulations. The output-to-output transmission $|S_{32}|$ has also been measured with values always below -10.0 dB in the design frequency range from 90.0 GHz to 110.0 GHz.

To show the high potential of a continuously LC-tuned SPDT even for the magnetically biased demonstrator, an intermediate state has been measured, resulting in an equal power split of about -6.0 dB between 105.0 GHz to 110.0 GHz. Nevertheless, the continuously adjustable power splitting ratio can only be achieved by means of biasing electrodes or continuously rotatable magnets.

Therefore, the aforementioned phase shifter as well as the SPDT demonstrator proved the high potential of the tuneable LC-waveguide technology for beam-steering and RF-switching. However, especially for the realisation of fully electrically tuneable components at W-band frequencies and above, the waveguide topology has its major challenge in the implementation of an electrical biasing network, because of the limited space inside the waveguide. Because of all the challenges from the biasing electrode realisation as well as the fact that a multilayer approach for an electrode design at 240 GHz had also not been successful [Wei17], a new class of low-loss tuneable waveguide topology needs to be established for W-band frequencies and above.

6 Tuneable Dielectric Waveguides and SPDT at W-Band

In the lower millimetre wave range, mostly metal based structures are used for guiding. However, since ohmic losses are steadily increasing with frequency, there is a demand for low-loss non-metallic-based, and therefore, purely dielectric waveguide structures at higher frequencies, in particular above 100 GHz.

The origins of dielectric waveguides are based on Sommerfeld's investigations on circularly symmetric TM waves traveling along a conductive wire [Som99]. Although this novel waveguide mechanism only had a very limited importance for practical applications, it inspired Hondros and Debye to theoretically investigate the possible propagation of a TM mode within a dielectric fibre in 1910 [Hon+10], which was experimentally confirmed by Zahn in 1916 [Zah16]. An important milestone, from which RF engineers are greatly benefiting [Spo+17; Ree+17a], was the discovery that dielectric rods, in contrast to waveguides, can be used as directive radiators [Mal43].

However, the main focus on the research of dielectric waveguides in the 1960s and ’70s was set on the optical domain, for which the solid core single-mode fibre is worldwide accepted for long-distance data transmission. Although the concepts of linear dielectric waveguides have mainly been investigated and understood up to the 1970s, research is still focussing on dielectric waveguides, since they are routinely used for high-bandwidth communication links and are currently under immense investigation for low-loss propagation in the THz regime [Ata+13]. The facts that the typically used optical fibres as well as metallic waveguides cannot be used at THz frequencies anymore as well as the lack of suitable low-loss dielectric waveguide materials, not only in the THz but also in the millimetre wave range, lead to an increased interest of dielectric waveguides in today‘s research.

Therefore, connected with the fact of a challenging implementation of an electrical biasing network specifically for tuneable LC metallic waveguide components at millimetre wave frequencies and above, this chapter deals with the investigation and realisation of low-loss tuneable and non-tuneable dielectric waveguides for application in beam-steering networks in general. At the same time, this represents an important step for the realisation of tuneable low-loss waveguides for the THz regime, since this technology is easily scalable to higher frequencies in the future, due to the unique properties of LC, also at THz.

6.1 Design Criteria

To be able to assess the correct dimension of the dielectric waveguides for W-band, analytical solutions for the different waveguide topologies are required. In comparison to metallic waveguides where well-defined electrical boundaries ensure an analytical solution, only circular and elliptical dielectric cylinders have an analytical solution [Yeh+08]. Hence, for the design of dielectric waveguides with other shapes, e.g. quadratic, approximation methods are required. Therefore, two approximation methods are introduced in the following, the geometrical optics approach as well as the approximation method by Marcatili from 1969 [Mar69].

6.1.1 Geometrical Optics Approach

Let us assume a planar dielectric slab waveguide, where the core material has a refraction index of $n_1 = \sqrt{\varepsilon_1}$ and the cladding material has a refraction index of $n_2 = \sqrt{\varepsilon_2}$, with $n_1 > n_2$ (see Fig. 6.1). Total internal reflections are occurring at the

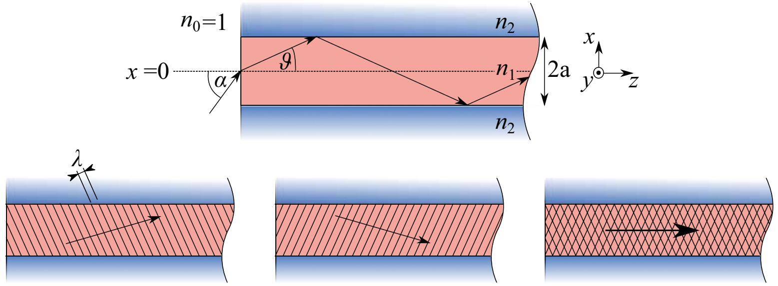

Figure 6.1: Schematic of the wave-guiding principle in a dielectric slab waveguide.

interface from core to cladding according to Snell's law, if the incident angle ϑ is always below the critical angle

$$\cos\vartheta_{\mathrm{crit}} = \frac{n_2}{n_1} \,. \tag{6.1}$$

Similarly, the coupling from a free space wave (n =1) into the waveguide is possible if $\sin\alpha \;<\; n_1 \;\sin\vartheta_{\mathrm{crit}}$, which can be re-written as

$$\sin\alpha \approx \alpha < n_1\sqrt{1-\cos^2\vartheta_{\mathrm{crit}}} = \sqrt{n_1^2 - n_2^2} =: \mathrm{NA}\,, \tag{6.2}$$

with α being the incident angle of the free space wave and NA being the numerical aperture. Not only that the dielectric waveguides support several incident angles, and therefore, several ways for the wave to travel through the waveguide, the wave also undergoes a phase shift between $0 \leq \Delta\varphi(\vartheta) \leq \pi$ during a total internal reflection at the interface. Therefore, it is mandatory that the phase shift of the wave is a multiple integer of 2π after two total internal reflections and two times transversally passing of the core with cross-section $2a$. The mode conditions can be expressed by [Kne+08]

$$\varphi_{\mathrm{transv.}} + 2\cdot\varphi_{\mathrm{refl.}}(\vartheta) = -4an_1k_0\sin\vartheta + 2\cdot\varphi_{\mathrm{refl.}}(\vartheta) = -2\pi m\,, \quad m = 0,1,2,... \tag{6.3}$$

The transverse profile of the field distribution remains unchanged along the propagation direction. While the superposition represents a standing wave in x-direction, it propagates in z-direction as shown in Fig. 6.1.

By defining the normalised frequency according to [Yeh+08] to

$$V := k_0a\sqrt{n_1^2 - n_2^2} = k_0a\mathrm{NA} \tag{6.4}$$

as well as dimensionless core and cladding-parameter

$$u := a\sqrt{k_0^2n_1^2 - \beta^2} \quad \& \quad w := a\sqrt{\beta^2 - k_0^2n_2^2}\,, \tag{6.5}$$

fulfilling the condition $u^2 + w^2 = V^2$, one can determine the number M of guided TE modes by

$$M = \left\lfloor \frac{V}{\pi/2} \right\rfloor + 1 \, , \tag{6.6}$$

where "$\lfloor ... \rfloor$" represents the biggest integer number contained in the argument [Rei05]. Therefore, a single-mode propagation is ensured in the dielectric core, if $V < V_\mathrm{c} = \pi/2$, with V_c being the normalised cut-off frequency. By expressing it in dependence of the wavelength

$$\lambda_0 > \lambda_{0,\mathrm{c}} = 4a\mathrm{NA} \, , \tag{6.7}$$

the cross-section $2a$ of the dielectric core can be determined for given frequency and material properties. With this cross-section it is now possible to determine the field distribution within the dielectric waveguide [Rei05]. Coming back to the assumption of the propagating wave being a superposition of two plane waves with wave vectors $\vec{k} = (\pm u/a, 0, \beta)$, the field distribution of the mode is

$$E \sim \left(e^{j(u/a)x} + e^{-j(u/a)x} e^{-jm\pi} \right) e^{-j\beta z} \, . \tag{6.8}$$

There, it is included that the two plane waves have a phase shift of $m\pi$ to each other in the centre of the core. The E-field distribution for different modes within the core ($|x| \leq a$) is given by

$$E_\mathrm{core} = E_\mathrm{core,0} \cos(ux') e^{-j\beta z} \, , \quad m = 0, 2, 4, ... \tag{6.9}$$

$$= E_\mathrm{core,0} \sin(ux') e^{-j\beta z} \, , \quad m = 1, 3, 5, ... \tag{6.10}$$

where $x' = x/a$ is the normalised transversal component. For the cladding ($|x| > a$), the normal component of the wave vector $\vec{k} = (\pm jw/a, 0, \beta)$ is getting imaginary and is depending on n_2, while the tangential component stays the same. Hence, the field distribution inside the cladding is described by

$$E_\mathrm{cladding} = E_\mathrm{cladding,0} e^{-w|x'|} e^{-j\beta z} \, . \tag{6.11}$$

Therefore, the evanescent electric field of a given mode is exponentially decaying with w, as shown for the first three modes in Fig. 6.2.

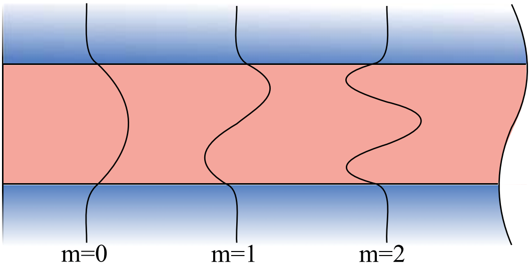

Figure 6.2: Schematic of the field distribution for the first order mode as well as for two higher order modes. The mode order m gives the number of zeros within the transversal field distribution.

6.1.2 Approximation Method of Marcatili

Since no analytical solutions can be found for rectangular dielectric waveguide shapes, Marcatili introduced his approximation method in 1969. Especially the solutions of the corner regions can only be found numerically if not approximated. Therefore, several assumptions are made, simplifying the rectangular dielectric waveguide problem to an analytically solvable scenario:

1. Based on the results of the geometrical optics approach, the main amount of the propagating wave is confined in the rectangular core of the waveguide.
2. The evanescent fields are decaying exponentially in the cladding region.
3. Due to a main orientation of the modes in x- and y-direction, only negligible parts of the field are propagating in the corner areas of the cladding.

Hence, the matching of the field components at the corner region is neglected by Marcatili. This breaks down the complex problem of a rectangular dielectric waveguide into two orthogonal dielectric slab waveguides, which is shown in Fig. 6.3. In the core region 1, a simple field distribution is assumed, varying sinusoidally in x- and y-direction. The evanescent fields of regions 2 and 4 are varying sinusoidally in x- and exponentially in y-direction, while being vice versa for the regions 3 and 5. The fundamental modes of interest have their electric field lines polarised either in x- or y-direction, where z is the propagation direction. Thus, depending in which of both directions the electric field lines are polarised, the modes are named E^x_{nm} or E^y_{nm}, respectively, with $n(m)$ being the number of field

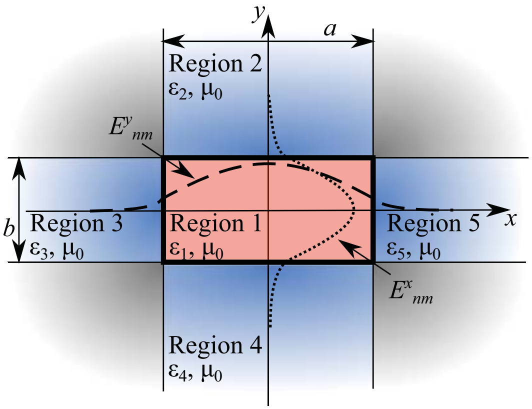

Figure 6.3: Schematic of the simplified rectangular dielectric waveguide scenario from Marcatili. Since only negligible parts of the field are propagating in the corner regions, they are left out from the mathematical calculations.

extrema in the x-(y-)direction. Further, all modal fields are supposed to form closed loops, which is why the field components E_x and H_y (E_y and H_x) can be neglected for E^y_{nm} (E^x_{nm}). In the following, the E^y_{nm} mode will be discussed in more detail, according to [Yeh+08].

Fulfilling the Helmholtz equations

$$\nabla^2 E_{x,y,z} + k^2 E_{x,y,z} = 0\,, \tag{6.12}$$

$$\nabla^2 H_{x,y,z} + k^2 H_{x,y,z} = 0\,, \tag{6.13}$$

with $k^2 = \omega^2 \mu \varepsilon$, the field components can all be expressed in terms of E_y to

$$E_x = \frac{1}{k^2 - k_y^2} \frac{\partial^2 E_y}{\partial x \partial y}\,, \quad E_z = \frac{\beta}{j(k^2 - k_y^2)} \frac{\partial E_y}{\partial y} \tag{6.14}$$

$$H_x = -\frac{\beta k^2}{\omega \mu (k^2 - k_y^2)} E_y\,, \quad H_z = -\frac{k^2}{j\omega\mu(k^2 - k_y^2)} \frac{\partial E_y}{\partial x}\,, \quad H_y = 0\,. \tag{6.15}$$

Restricting the excitation of the mode to small incident angles only results in $k_{x,y} \ll k_z$, by which $E_x \approx 0$ can be assumed, since E_x is of the order of $k_x k_y$, and therefore, negligible. The solutions for the E^y_{nm} modes's y-component in the different regions can be derived from the corresponding Helmholtz equation to

$$E_y^{(1)} = A_1 \cos(k_{x1}x + \zeta)\cos(k_{y1}y + \xi) \ , \tag{6.16}$$

$$E_y^{(2)} = A_2 \cos(k_{x2}x + \zeta)e^{-jk_{y2}y} \ , \tag{6.17}$$

$$E_y^{(3)} = A_3 \cos(k_{y3}y + \xi)e^{jk_{x3}x} \ , \tag{6.18}$$

$$E_y^{(4)} = A_4 \cos(k_{x4}x + \zeta)e^{jk_{y4}y} \ , \tag{6.19}$$

$$E_y^{(5)} = A_5 \cos(k_{y5}y + \xi)e^{-jk_{x5}x} \ , \tag{6.20}$$

where $k_\nu = \omega^2\mu\varepsilon_\nu = k^2_{x,\nu} + k^2_{y,\nu} + \beta^2$ with $\nu = 1, 2, 3, 4, 5$, A_ν being constant and ζ and ξ defining the location of the field maxima and minima within region 1. Matching the electric and magnetic field at the boundaries leads after small simplification to the transcendental equations

$$k_x a = n\pi - 2\tan^{-1}\left(\frac{k_x}{\sqrt{k_1^2 - k_2^2 - k_x^2}}\right) \tag{6.21}$$

and

$$k_y b = m\pi - 2\tan^{-1}\left(\frac{\varepsilon_2}{\varepsilon_1}\frac{k_y}{\sqrt{k_1^2 - k_2^2 - k_y^2}}\right) \ . \tag{6.22}$$

Here, it was assumed, that the complete cladding material consists of the same dielectric material with permittivity ε_2 and wave number k_2.With the help of these equations, the propagation constant of the E^y_{nm} mode can be calculated to

$$\beta = \sqrt{k_1^2 - k_x^2 - k_y^2} \ . \tag{6.23}$$

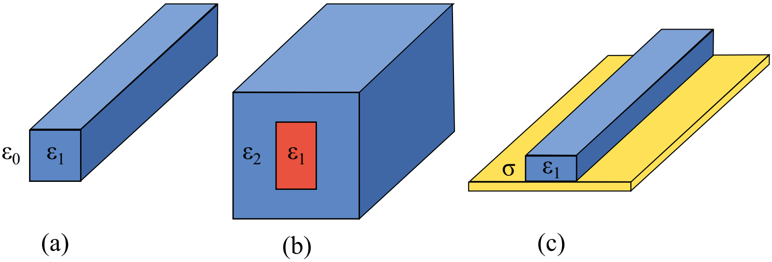

Figure 6.4: Schematic of the most important dielectric waveguide topologies with (a) the subwavelength fibre, (b) the step-index fibre as well as (c) the dielectric image waveguide.

Therefore, for given material properties and frequency it is possible with this approximation to make first calculations for the waveguide dimensions a and b. Unfortunately, such approximations are only the first step and the resulting dimensions need to be optimised with modern 3D simulation tools, since a dielectric waveguide of a given cross-section is not only supporting a finite number of guided modes, but also a continuous spectrum of radiation modes. Due to the open waveguide structure, a certain amount of the guided wave can already escape as radiated wave, if the waveguides are bent too sharp or obstacles/discontinuities are present.

A selection of the most important dielectric waveguides with rectangular shape is given in Fig. 6.4. The subwavelength (sWL) fibre is the simplest dielectric waveguide, since it only consists of one dielectric material with a cross-section of approximately $\lambda_0/2$. The evanescent fields are propagating in the air outside

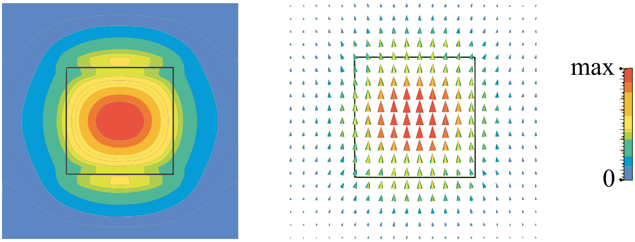

Figure 6.5: Simulated field distribution of the E^y_{11} mode of an sWL fibre at 100 GHz.

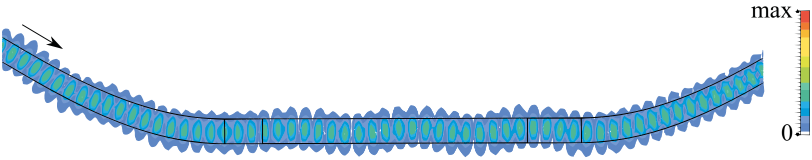

Figure 6.6: Simulated field distribution within an sWL fibre. If the radii of the bends are too small, multiple reflections/bouncing is occurring due to the loose field confinement.

the fibre, as shown in Fig. 6.5, providing a comparatively low-loss propagation compared to the one in a dielectric material with finite dielectric loss. However, this is also a disadvantage for tuneable dielectric waveguides, where biasing electrodes need to be implemented. The electrodes need to be kept in a certain distance that the presence of the biasing electrodes is not influencing the propagating field.

The step-index fibre is the most commonly known dielectric waveguide topology. It comprises of two dielectric materials, with different refraction indices/permittivities. The propagating field is mainly focussed in the core material, while the evanescent fields are propagating in the cladding. Compared to the sWL fibre, it has the advantages of a higher mechanical stability as well as the shielding of the propagating field from outside influences. Therefore, a realisation of the biasing electrodes directly on the cladding material is possible.

However, due to the missing boundary conditions, the propagating wave in an sWL or step-index fibre is only weakly confined inside the dielectric material. If the radius of an upcoming bend is too small, multiple reflections or even radiation can occur. One example is given in Fig. 6.6 for the sWL fibre. Also, the sWL fibre cannot be mechanically supported without influencing the evanescent fields. This problem can be remedied using a dielectric image waveguide, being a planar version of a dielectric waveguide [Kin+57; Kin+58]. It is based on an sWL fibre with only half of the original height, being directly placed on a conducting sheet. According to the image theory, this waveguide is acting as a dielectric waveguide with full cross-section. At the same time, the dielectric fibre itself is supported by the metal without any field disturbances [Yeh+08].

In the following, however, the main focus will be on the realisation of (non-)tuneable dielectric waveguide components in sWL and step-index fibre topology. Before the specific components can be designed, a material evaluation needs to be conducted first, for identifying well-suitable dielectric materials for W-band frequencies.

6.2 Material Evaluation

The choice of dielectric materials is directly linked to the premise that LC can be used as tuneable core material in a step-index fibre. Thus, additionally to the fact that the materials should be low-loss in W-band, the dielectric materials should fulfil the following requirements for the design of tuneable dielectric waveguide components:

- The cladding material for a tuneable step-index fibre needs a permittivity below 2.4 to ensure total internal reflection
- The materials for the sWL fibre as well as for the non-tuneable core material for the step-index fibre need a permittivity around 2.8 to be well matched to the mean permittivity of LC
- The materials need to be well processable (drilling, milling and gluing) to be able to implement a hermetically sealed LC cavity

Where polymethyl methacrylate is revealing a comparatively high dielectric loss towards THz frequencies ($\tan\delta = 2.7 \cdot 10^{-3}$ at $f = 100\,\mathrm{GHz}$), the dielectric properties of PTFE ($\tan\delta = 2.2 \cdot 10^{-4}$ at $f = 100\,\mathrm{GHz}$), high-density polyethylene ($\tan\delta = 3.1 \cdot 10^{-4}$ at $f = 160\,\mathrm{GHz}$) and Rexolite ($\tan\delta = 6.6 \cdot 10^{-4}$ at $f = 100\,\mathrm{GHz}$) are very good at W-band frequencies [Ata+13; Hof+03; Fri+97; Hir+96; Lam96]. PTFE ($\varepsilon_r = 2.1$) and high-density polyethylene ($\varepsilon_r = 2.3$) are very promising choices in terms of permittivity for being the cladding material of the tuneable step-index fibre. However, both are very flexible, making the processing of precise structures difficult. Furthermore, gluing is very challenging.

The best trade-off for the cladding material is met by the use of Rexolite. Its hard plastic properties allow an excellent processing of the designed components, which can also be glued. But, this rigidity is also a disadvantage, since already small mechanical forces can lead to cracks inside the fibre. The permittivity of Rexolite is with 2.53 close to the lowest permittivity of LC. As a result, Rexolite is not only chosen for the cladding material of the step-index fibre, but also for the material of the sWL fibre.

The evaluation of suitable core materials and adhesives was done in a qualitative way. For this, different step-index fibres with different core materials and adhesives are realised, characterised and compared with each other. The used measurement system will be described in the following before the results are presented.

6.2.1 WR10-to-sWL fibre transition

First, an efficient excitation of the dielectric waveguides needs to be provided. The best solution for this is a metallic to dielectric waveguide transition, which is why a WR10-to-sWL fibre transition was designed. The sWL fibre was chosen to be the excited dielectric waveguide, since its excitation is simpler as for the step-index fibre. The cross-section of the sWL fibre made of Rexolite was determined both by the geometrical optics and Marcatili approaches to be 1.88 mm. After optimisation in CST Studio Suite, the cross-section was finally set to 1.8 mm.

Starting with the TE_{10} mode propagating in a WR10 rectangular waveguide, a tapered dielectric is inserted for matching and to smoothly focus the mode inside the dielectric. Together with a metallic taper, which decreases to the width of the dielectrically filled waveguide, it results in a wave propagating in a fully dielectrically filled rectangular waveguide. If the waveguide is now simply cut as shown in Fig. 6.7, the wave will bend around the metallic corners, causing radiation. Therefore, a horn-like extension of the waveguide is designed, that the evanescent fields of the excited E_{11}^{y} mode of the dielectric waveguide can be gently guided out of the waveguide and vice versa. By this, the simulated loss caused by radiation could already be decreased from 30 % to 1 %. A detailed schematic of the taper sections is given in Fig. 6.8.

In section (A), the dielectric shows a triangular taper up to the sWL fibre width of $w_{\mathrm{sWL}} = 1.8$ mm. The metallic waveguide is starting with the WR10 dimensions and is decreasing in width down to the size of the dielectric fibre from section (A) to (B), to suppress higher order modes. This results in a completely dielectrically filled metallic waveguide with dimensions 1.80 mm × 1.27 mm in section (B). There, an additional register pin made of Rexolite with a diameter of 0.6 mm is keeping the taper in its place. In section (C) the height of the dielectric material is increasing,

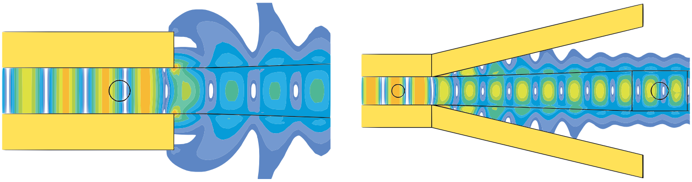

Figure 6.7: Simulated field distribution of the WR10-to-sWL fibre transition with (left) an abrupt cut or (right) horn-like extension of the metallic waveguide at 100 GHz.

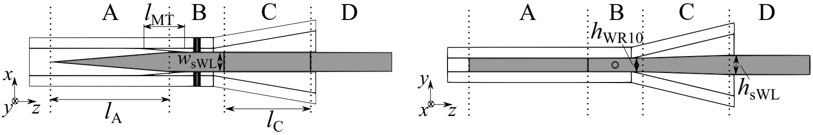

Figure 6.8: Schematics of the dielectric and metallic tapering inside the WR10-to-sWL fibre transition. In section (A) the triangular tapering to a width of 1.8 mm is shown. While in (B) the dielectric dimensions stay constant, in (C) the height is increasing to 1.8 mm. Further, from (A) to (B) the metallic waveguide is tapered in width down to 1.8 mm, while the height is kept constant. The most important dimensions are $l_{\mathrm{A}} = 10\,\mathrm{mm}$, $l_{\mathrm{MT}} = 4.5\,\mathrm{mm}$, $l_{\mathrm{C}} = 8\,\mathrm{mm}$, $w_{\mathrm{sWL}} = 1.8\,\mathrm{mm}$, $h_{\mathrm{WR10}} = 1.27\,\mathrm{mm}$, and $h_{\mathrm{sWL}} = 1.8\,\mathrm{mm}$.

ending up in the final dimensions of the sWL fibre of 1.80 mm × 1.80 mm. A photograph of this transition as well as first measurement results with sWL fibres of different lengths made of Rexolite are presented in Fig. 6.9. The transition was realised as symmetric split-block made of brass, being cut in the E-plane.

While matching $|S_{11}|$ is better than $-15\,\mathrm{dB}$ between 85 GHz to 110 GHz, transmission coefficients from $-0.5\,\mathrm{dB}$ to $-2.0\,\mathrm{dB}$ were revealed for the sWL fibres of different lengths. The radiation losses due to discontinuities could not be reliably determined within the simulations. For the first measurement, only two taper sections of the sWL fibre are connected to each other, leading to a distance of 1.5 mm between the horns of the WR10-to-sWL fibre transitions. Due to the vicinity of the horns, radiation is not an issue which leads to a good match of measurement and simulation. The same setup was measured again after including a Rexolite segment of 10 mm length between the taper. This setup is later on referred to as the reference line of the sWL phase shifter, introduced in subsection 6.3.1, since it is the same setup as the phase shifter, just that the LC-filled segment is left out. There, the measurement results are 0.5 dB worse than the simulation results. The same trend can be observed for the measurement results with a Rexolite segment of 36 mm length. These deviations of 0.5 dB can be attributed to the insufficient representation of radiation losses in the simulation of the WR10-to-sWL fibre transitions, due to fabrication tolerances as well as possible air inclusions at the connection points of the sWL taper. They are represented in the results as a systematic error, not depending on the fibre's length as long as a critical length has been overcome. This is visible in the big difference between the measurement of the taper and the reference line with respect to their corresponding simulation results. The reference line and the 26 mm longer version show with $-0.25\,\mathrm{dB}$ at 100 GHz less difference in

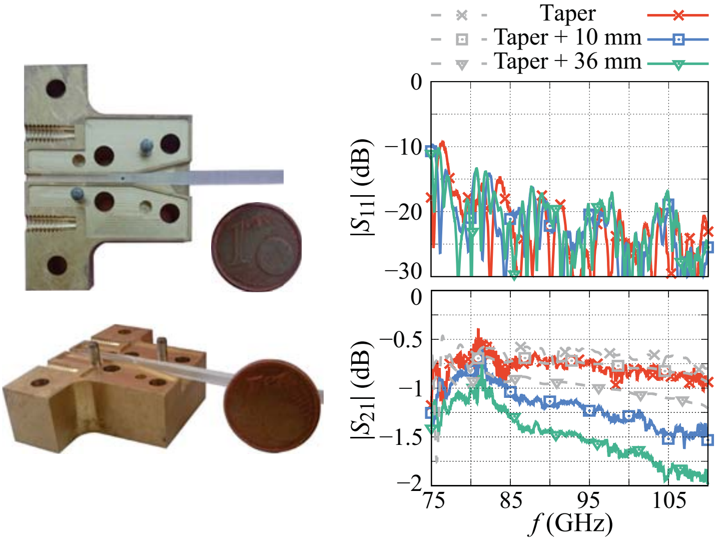

Figure 6.9: (left) Realised WR10-to-sWL fibre transition with Rexolite fibre. (right) Simulation and measurement results of back-to-back measurements of the transitions with different fibre lengths. First, the two taper sections have been connected to each other (Taper), where the horns are separated 1.5 mm from each other. Additionally, Rexolite segments of 10 mm and 36 mm length were connected between the taper. Simulation results are given in dashed, measurement results in solid line.

$|S_{21}|$, although the increase in dielectric length is 2.6 times larger than between the first two measurements, where a difference of −0.50 dB at 100 GHz was measured. This discrepancy is even more obvious for linear S-parameter results.

However, a steeper decrease of the measured transmission coefficients $|S_{21}|$ compared to simulation can be observed for the reference line and the 26 mm longer version. This might be based on a slightly increased dielectric loss of Rexolite as well as a not perfectly sealed split-block, both having a higher impact at higher frequencies. Since this trend is not observed for the taper measurements, it will most probably be based on radiation due to fabrication tolerances.

6.2.2 Qualitative Material Evaluation

After the functional principle of first non-tuneable Rexolite sWL fibres is proven, additional materials need to be qualitatively investigated for a realisation of step-index fibres. For this, core materials as well as adhesives are needed. Different possible core materials have been investigated, where the most promising ones in terms of permittivity and dielectric loss were RO3003 from Rogers Corporation ($\varepsilon_r = 3.0$ & $\tan\delta = 5.0 \cdot 10^{-2}$ at 100 GHz [Tal+15]) and fused silica ($\varepsilon_r = 3.81$ & $\tan\delta = 4.0 \cdot 10^{-4}$ at 40 GHz [Her17]). Although fused silica has the better dielectric properties it turned out that the challenging fabrication leads to considerable tolerances, and therefore, to air inclusions in the core region. This results in an increased radiation. Measurements of non-tuneable step-index fibres with different core materials led to the conclusion, that step-index fibres with Rexolite as cladding and RO3003 as core material reveal the best performance.

Since the step-index fibres were fabricated in multiple single pieces within this work, they needed to be glued together. For this, the performance of several glues was compared by means of transmission coefficient measurements, as shown in Fig. 6.10. Also, for the step-index fibre the WR10-to-sWL fibre transition is used, because it is easier to focus the propagating wave from an sWL fibre into the step-index fibre's core as directly from the rectangular waveguide. The simulation as well as the measured results are presented in Fig. 6.11.

Amongst others, a special Rexolite glue from C-Lec Plastics Inc. (Rexolite Adhesive 12517 Composition) was used, exhibiting the same dielectric properties as the full material. Therefore, this measurement should be close comparable to the ideal simulation without glue. However, the demonstrator showed gas bubbles at the splice, which is due to a non-perfectly outgassing of the glue's solvents. Hence, this glue is not suitable for sealing an LC cavity. Due to this and the fact that the bubbles

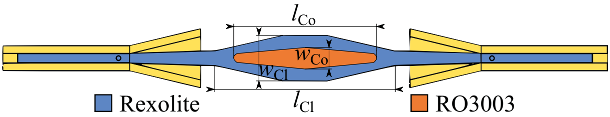

Figure 6.10: Schematic of the used measurement setup for the qualitative evaluation of adhesives. The two halves of the cladding are glued together after the insertion of the RO3003 core, while the taper sections are connected by means of register pins. The most important dimensions are $l_{\mathrm{Cl}} = 24.0\,\mathrm{mm}$, $w_{\mathrm{Cl}} = 6.0\,\mathrm{mm}$, $l_{\mathrm{Co}} = 19.1\,\mathrm{mm}$, $w_{\mathrm{Co}} = 2.8\,\mathrm{mm}$.

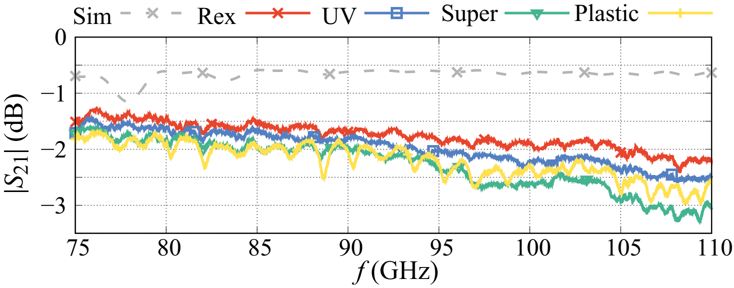

Figure 6.11: Simulation and measurement results of the qualitative glue evaluation. A special Rexolite, UV, plastic and superglue were examined.

are discontinuities, causing radiation, it cannot be used although exhibiting the lowest loss. The plastic glue (UHU Allplast) as well as superglue (Pattex superglue) are both sealing the splice very well, but unfortunately associated with high losses. The most promising adhesive in terms of manageability as well as performance was the UV glue (Norland Products NOA81). It can be precisely applied to the surface, since sticking first starts when the glue is exposed to UV light. Moreover, this glue shows a performance only slightly decreased to the one with Rexolite glue.

To conclude the material evaluation, the sWL fibre based devices within this work

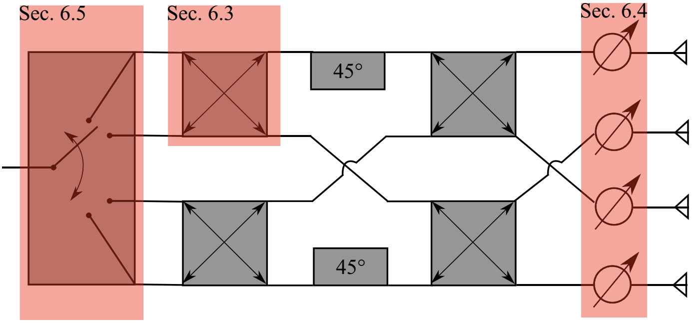

Figure 6.12: Schematic overview of the investigated dielectric waveguide components with corresponding section numbers.

are all made of Rexolite, while the step-index fibre based devices are realised by using Rexolite as cladding and RO3003 as non-tuneable core material, being glued together by the UV adhesive. In the following, the required non-tuneable dielectric waveguide components for beam-steering networks will be investigated first, before the tuneable ones are presented (see Fig. 6.12).

6.3 Non-Tuneable Components

6.3.1 Multimode Interference Power Divider

The wave impedance of dielectric waveguides is difficult to determine, due to the loose field confinement. The field distribution of the E- and H-field, for example, cannot only be significantly influenced by discontinuities along the waveguide, but in case of the sWL fibre also from outside influences. Hence, power dividers based on impedance transformation are not applicable for dielectric waveguides, which is why power dividing topologies known from metallic waveguides, can only partially be adapted to dielectric waveguides. For example, a magic T-junction would lead to enormous radiation, while a Y-branch power divider can be used if the bends are smooth enough [Ogu85; Kuz85]. However, first investigations on dielectric Y-branch power divider showed that they can prove the principle, but either they suffer from increased radiation or the dimensions need to be very large. Therefore, a more promising dielectric power divider topology is investigated being already known from optics, the *multimode interference (MMI) power divider* [Bac+94].

The MMI power divider is based on the self-imaging principle, which was defined by Soldano as follows [Sol+95]:

"*Self-imaging is a property of multimode waveguides by which an input field profile is reproduced in single or multiple images at periodic intervals along the propagation direction of the guide.*"

MMI devices are based on waveguides structures which allow the propagation of multiple modes. In the following, the focus will be on MMI in one plane, where the design of the used structure is transversally single-moded and laterally multi-moded. Hence, the field profile $\Psi(y,0)$ of an incoming wave at $z = 0$ will decompose into the field distribution $\psi_\nu(y)$ of all modes (guided and radiated)

$$\Psi(y,0) = \sum_{\nu} c_\nu \psi_\nu(y) \,, \tag{6.24}$$

with c_ν being the field excitation coefficients. If the incoming wave is confined well and no radiated modes are excited, the superposition of the guided mode fields at a certain distance z can be written as

$$\Psi(y,z) = \sum_{\nu=0}^{m-1} c_\nu \psi_\nu(y) e^{j(\omega t - \beta_\nu z)} \ . \tag{6.25}$$

Assuming the phase of the incoming, fundamental mode to be constant and the time dependency implicit, the field distribution becomes

$$\Psi(y,z) = \sum_{\nu=0}^{m-1} c_\nu \psi_\nu(y) e^{j(\beta_0 - \beta_\nu) z} \ , \tag{6.26}$$

with $(\beta_0 - \beta_\nu)$ being the propagation constant spacing. It is given by

$$(\beta_0 - \beta_\nu) \simeq \frac{\nu(\nu+2)\pi}{3L_\pi} \ , \tag{6.27}$$

with L_π being the beat length of the two fundamental modes

$$L_\pi \simeq \frac{4nw_{\text{eff}}^2}{3\lambda_0} \ , \tag{6.28}$$

where w_{eff} is the effective width of the MMI structure, taking the evanescent fields into account. The field distribution at a certain distance $z = L$ is thus given by

$$\Psi(y,L) = \sum_{\nu=0}^{m-1} c_\nu \psi_\nu(y) e^{j\frac{\nu(\nu+2)\pi}{3L_\pi}L} \ . \tag{6.29}$$

The field distribution at this certain distance is a *self-image* of the incoming field, if the modal phase factor

$$e^{j\frac{\nu(\nu+2)\pi}{3L_\pi}L} = 1 \ , \tag{6.30}$$

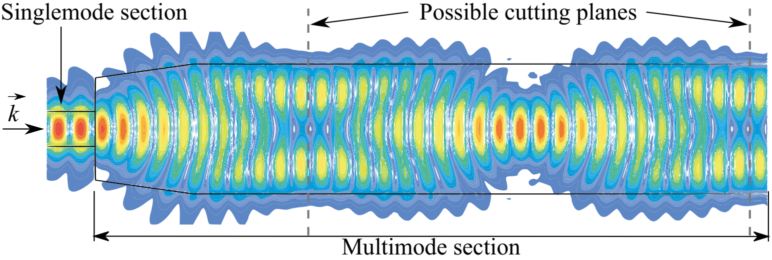

Figure 6.13: Schematic of the self-imaging principle within a dielectric multimode interference structure, fed by a single-moded sWL fibre.

which means that all guided modes interfere with the same relative phases at this point as in $z = 0$. The first N-fold images of the input field $\Psi(y, 0)$ are obtained at the length

$$L = \frac{3L_\pi}{4N} \,. \tag{6.31}$$

A schematic of such a self-image is presented in Fig. 6.13. By carefully choosing the length of the MMI section, as indicated as cutting plane in the figure, an equal power division is obtained without any radiation. This principle is not limited to 2D problems, but also applicable for 3D problems, where the multimode interference is taking place in x- and y-direction. However, the MMI power divider investigated in this work is a 2D 1:2 power divider.

The high potential of MMI power divider compared to Y-branch power divider is illustrated in Fig. 6.14, where the simulated E-field distributions of both power dividers with the same absolute length is shown. While the Y-branch power divider is prone to multiple reflections, and hence, radiation, the MMI power divider shows a homogeneously propagating wave in both branches. To avoid the multiple reflections at the Y-branch power divider, the bends need to be gentler, resulting in an increased total length and dielectric loss. In these simulations, the branches were separated that wide due to the needed WR10 flanges for characterisation.

Exemplarily, the realised MMI power divider demonstrator is shown in Fig. 6.15. It is milled as one single piece out of a Rexolite sheet and connected to the dielectric taper by sticking. Additionally, three WR10-to-sWL fibre transition split-blocks are used for the connection to the VNA. Since the measurements were carried out as

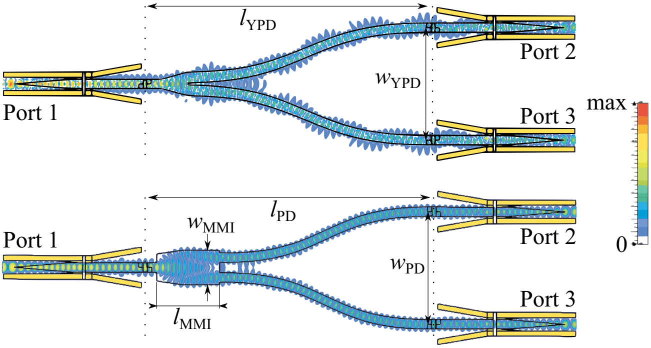

Figure 6.14: Simulation model including the field distribution of the dielectric (top) Y-branch and (bottom) MMI power divider. The MMI section has a width of $w_{\mathrm{MMI}} = 6.6\,\mathrm{mm}$, a length of $l_{\mathrm{MMI}} = 12\,\mathrm{mm}$ and is slightly tapered at the input. The total length and width of both power dividers are the same with $l_{\mathrm{YPD}} = l_{\mathrm{PD}} = 53.0\,\mathrm{mm}$ and $w_{\mathrm{YPD}} = w_{\mathrm{PD}} = 23.4\,\mathrm{mm}$, respectively.

two port measurements, the unused port was terminated by a matched load. The characterisation results for both the MMI and Y-branch power divider are presented in Fig.6.16 and Fig. 6.17, respectively.

For both topologies, the matching $|S_{11}|$ is better than simulated, due to the slightly increased radiation, with values below $-15\,\mathrm{dB}$ between 80 GHz to 110 GHz. Also, the power is split up equally with transmission coefficients $|S_{21}|$ between $-4.5\,\mathrm{dB}$

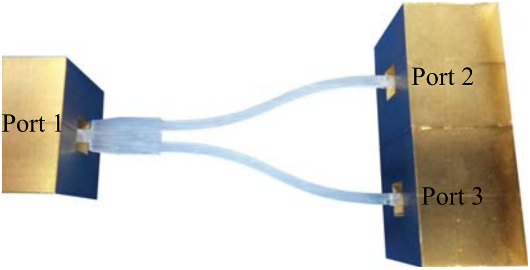

Figure 6.15: Photograph of the dielectric MMI power divider measurement setup.

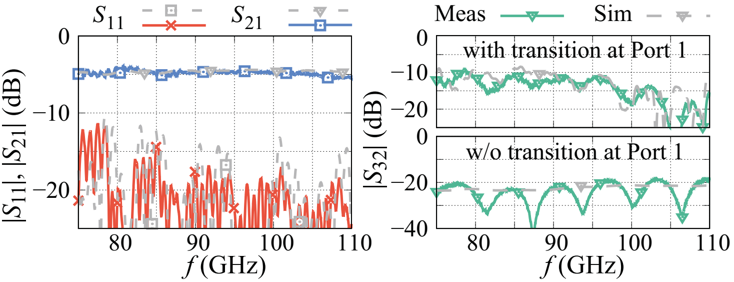

Figure 6.16: S-parameter simulation and measurement results of the dielectric MMI power divider. (left) The insertion as well as return loss are shown, while (right) the output isolation S_{32} is given with and without the WR10-to-sWL fibre transition at port 1. Simulation and measurement results are given in dashed and solid lines, respectively. For the sake of clarity, only $|S_{21}|$ is shown from the transmission coefficients.

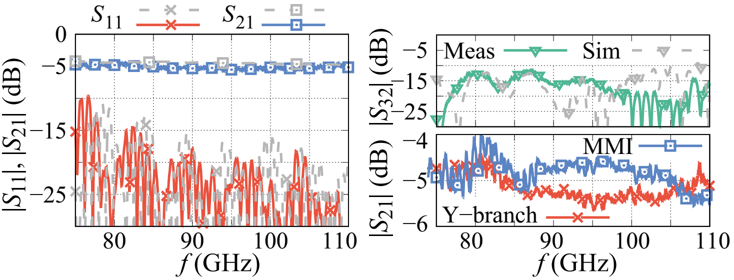

Figure 6.17: S-parameter simulation and measurement results of the dielectric Y-branch power divider. (left) The insertion as well as return loss are shown, while (right) the output isolation S_{32} as well as a comparison of the forward transmission of the Y-branch as well as MMI power divider are given. For the sake of clarity, from the transmission coefficients only $|S_{21}|$ is shown.

to −5.0 dB for the MMI as well as −4.8 dB to −5.5 dB for the Y-branch power divider, being in a good agreement to the simulation. The output isolation $|S_{32}|$ of −10 dB to −20 dB, including the WR10-to-sWL fibre transition at port 1, is matching the simulation well for both topologies. Only at frequencies above 105 GHz the difference to the simulation is around 5 dB, being directly connected to the slightly decreased $|S_{21}|$ compared to the simulation.

The comparatively low isolation is due to radiated field components, being reflected at the metallic WR10-to-sWL fibre transition at port 1. The reflected wave is coupling back to the fibre and contributing to the measured isolation. When this transition is removed and the dielectric fibre at port 1 ends just with a dielectric taper radiating into free space, $|S_{32}|$ is around -20 dB over the measured frequency range, as can be seen for the MMI power divider in Fig. 6.16. The radiated field is propagating into free space instead of being reflected. According to simulation, this improvement can be already achieved if the WR10-to-sWL fibre transition at port 1 is sufficiently separated from the main body of the power divider. This is the case if the sWL fibre at the input is elongated two to three times.

6.3.2 Multimode Interference Coupler

The MMI principle is also adaptable to asymmetrically fed as well as multiply excited MMI structures being required for the realisation of MMI based 4-port coupling structures for the later application in an interference-based SPDT. Similar to the power divider, an MMI coupler has been investigated, being based on the same self-imaging principle of [Sol+95]. The design as well as the field distribution are shown in Fig. 6.18.

The MMI section is designed in two pieces, so that the gap between the branches can be processed as precisely as possible. The halves are fixed to each other with the help of two Rexolite register pins. The total length of the coupler is $l_C = 69.0$ mm and its width is defined by the required WR10 flanges to $w_C = 23.4$ mm, as for the power divider. The realised demonstrator and the characterisation results are shown in Fig. 6.19 and Fig. 6.20, respectively. During characterisation, one branch is left open with the triangular taper radiating into free space, since only three

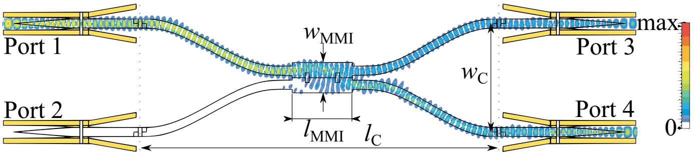

Figure 6.18: Simulation model including the field distribution of the dielectric MMI coupler. The multimode section has the same dimensions as for the power divider, except the tapered part. It has a width of $w_{\mathrm{MMI}} = 6$ mm, a length of $l_{\mathrm{MMI}} = 12$ mm.

Figure 6.19: Photograph of the dielectric MMI coupler demonstrator. The two halves are sticked together by means of two register pins made of Rexolite.

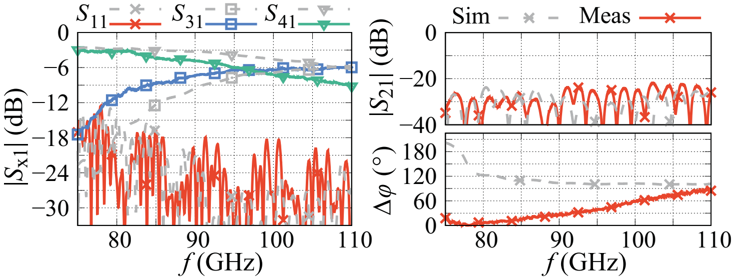

Figure 6.20: S-parameter simulation and measurement results of the dielectric multimode interference coupler. The measurements are given in solid, the simulations in dashed lines.

WR10-to-sWL fibre transitions were available. The transition port which was not connected to the VNA was matched with a load.

$|S_{11}|$ matches the simulation well for frequencies below 90 GHz. Above this frequency, the matching is around 5 dB worse than simulated. Nevertheless, it is always below −12 dB and even below −18 dB above 90 GHz. The input-to-input transmission $|S_{21}|$ is also matching the simulations well with values around −24 dB.

Compared to simulation, the intersection point of the transmission coefficients $|S_{31}|$ and $|S_{41}|$ is shifted in frequency about 10 GHz to lower frequencies. The absolute value of −6.7 dB is on the other hand only 0.5 dB worse than the simulated one.

Further, it can be seen that the measured phase difference between ports 3 and 4 is not matching the simulation. In the simulation, a decreasing trend with increasing frequency can be seen, while the phase difference is nearly constant from 90 GHz to 110 GHz with values between 100° to 103°. The decrease is due to the increased radiation at these frequencies, since the field is not confined sufficiently. The bends are too sharp for the loose field confinement and parts of the radiated wave with a different phase are coupling back to the structure later on.

A small decreasing trend is also observable in the measurement between 75 GHz to 78 GHz. Above these frequencies the phase difference is increasing with frequency, resulting in the theoretically expected phase difference of 90° around 110 GHz. However, for the later application in the SPDT additional phase difference can be provided by the tuneable phase shifters to compensate the decreased phase difference of the coupler.

This reduced phase difference compared to theory and simulation can be explained by the imperfections of the fabricated demonstrator. The register pins used for the assembly of the combiner are cut by hand, easily allowing a small gap, and therefore, air inclusions. Despite the two-piece fabrication of the combiner, the gaps between the incoming and outgoing branches as well as at the corners of the dielectric block cannot be realised ideally rectangular. This has a great impact on the overall performance of the combiner, since coupling is already/still taking place before/after the actual dielectric block. This is also explaining the shift in frequency of the intersection point mentioned above.

6.4 Tuneable Phase Shifter Topologies

Since power division and combining is proven, the focus will now be on the key component, the continuously tuneable LC phase shifters. For applications where only less phase shift is needed, e.g. for an SPDT, sWL fibre based phase shifters are investigated. They have the big advantage that the propagating wave is not facing an significant discontinuity, since all needed components are designed in sWL topology and the permittivity of the integrated LC is in the range of the one of the fibre material Rexolite. However, since a certain cavity thickness is needed, the achievable phase shift is more limited as for other topologies. Therefore, step-index fibre phase shifters are investigated for applications where much phase shift is required, e.g. in phased array antennas. There, the complete core section can be replaced by LC, by which a high phase shift can be provided within a comparatively short length.

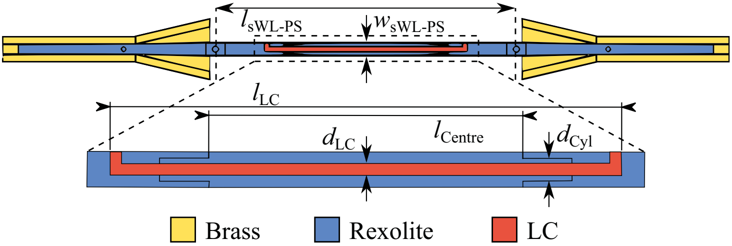

Figure 6.21: Schematic of the sWL phase shifter design. The most important dimensions are $l_{\text{sWL}-\text{PS}} = 38.5\,\text{mm}$, $w_{\text{sWL}-\text{PS}} = 1.8\,\text{mm}$, $l_{\text{LC}} = 26.0\,\text{mm}$, $d_{\text{LC}} = 0.6\,\text{mm}$, $l_{\text{Centre}} = 16.0\,\text{mm}$ and $d_{\text{Cyl}} = 1.2\,\text{mm}$.

6.4.1 Subwavelength Topology

Design & Realisation

A schematic of the sWL phase shifter design is given in Fig. 6.21. The cross-section was chosen to be quadratic, with edge lengths of $w_{\text{sWL}-\text{PS}} = 1.8\,\text{mm}$. Including the taper section it is built up in five pieces, with a drilled LC cavity of $l_{\text{LC}} = 26\,\text{mm}$ length and $d_{\text{LC}} = 0.6\,\text{mm}$ in diameter. To provide such a cavity with additional filling holes, the cavity itself is designed in three pieces, which were glued together. The connection points are designed as tube and cylinder, that the gluing interfaces can be chosen apart from the drilled cavity to avoid a blockage. After gluing, the LC can be filled by the use of a syringe and the cavity can be sealed by means of Rexolite pins.

For tuning, the LC was oriented either magnetically or electrically by using biasing electrodes. A schematic of both biasing methods is shown in Fig. 6.22. While for the magnetic biasing a pair of permanent rare earth magnets were used, as for the waveguide phase shifter, two pairs of copper electrodes surrounding the fibre were forming the electric biasing system. Both, the magnets and the electrodes need to be separated sufficiently from the fibre itself for not disturbing the evanescent field. For the magnetic biasing, PVC plates were used for keeping the magnets on distance to the fibre. For the electric biasing system, Rohacell 31HF, a high-performance structural foam from Evonik Industries, was used to keep the electrodes at a distance of $d_{\text{El}} \approx 3\,\text{mm}$ to the sWL phase shifter. It has a permittivity around 1.05 and a dielectric loss of 0.01 around 27 GHz [Ind17]. However, since most of the material is air and the evanescent fields are only facing very thin membranes of the

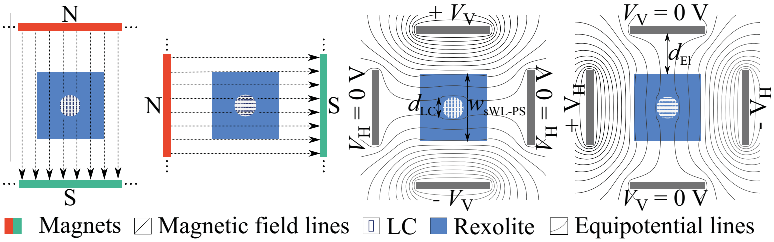

Figure 6.22: Cross section of the sWL phase shifter including (left) the magnetic biasing system consisting of two rare-earth permanent magnets as well as (right) the electric biasing system comprising of two pairs of copper electrodes. Both biasing states, parallel and perpendicular, are given for each method. V_V is the vertical biasing voltage and V_H the horizontal one.

foam, the dielectric loss does not have a significant impact on the phase shifter's performance.

Characterisation

Because of the large electrode distance, maximum biasing voltages of ±550 V were used. The measurement setup including the magnetic as well as half of the electrical biasing system is shown in Fig. 6.23. The simulation and measurement results are presented in Fig. 6.24.

For the sake of clarity, only the results for a perpendicular alignment are presented in Fig. 6.24, since they are exhibiting the highest loss. The reflection coefficient $|S_{11}|$ is matching the simulation very well with a broadband matching better than -10 dB and even -20 dB from 95 GHz to 110 GHz. The transmission coefficients are for both alignment mechanisms around 1 dB lower than simulated with values between -1.5 dB to -2.5 dB. Using magnetic biasing, $|S_{21}|$ is slightly worse compared to electric biasing, since magnetic biasing provides a more homogeneous alignment of the LC.

The phase shift for the magnetic biasing matches the simulation well and is even a bit increased compared to it. This is due to a small possible offset in the drilling process, by which the LC cavity length was slightly increased. The phase shift for the electrical biasing is less than for the magnetic biasing, being due to a not perfectly oriented LC. However, the achieved phase shift is more than 90° above

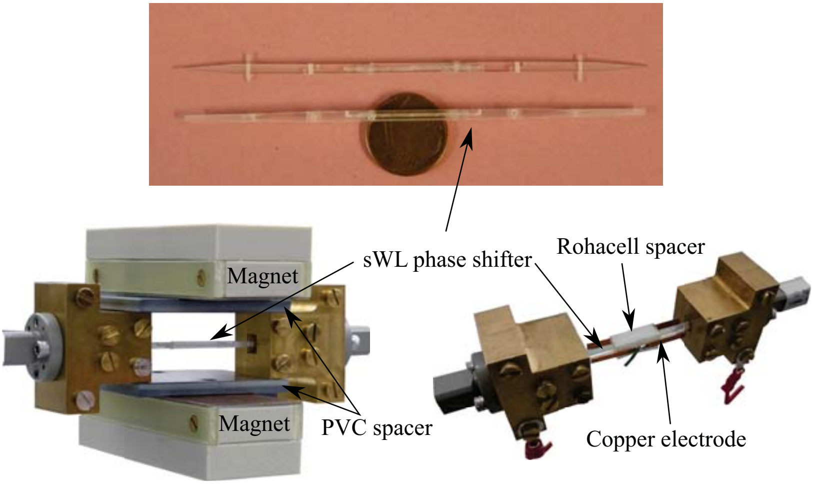

Figure 6.23: Photographs of (top) the realised sWL phase shifter demonstrators as well as (bottom) the measurement setup for both biasing methods.

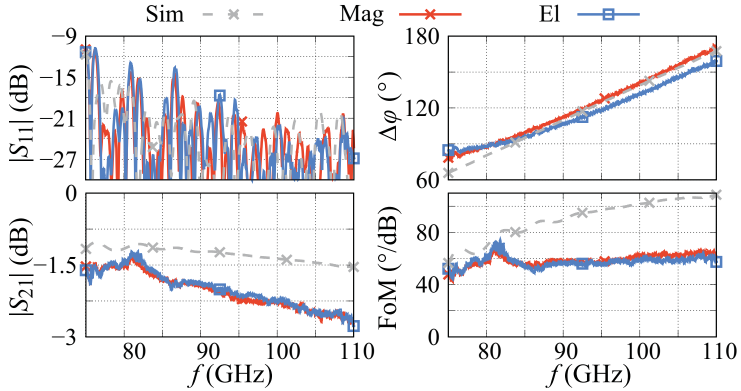

Figure 6.24: Simulated and measured (left) S-parameter, (right) phase shift and FoM results of the tuneable sWL phase shifter.

80 GHz, making the phase shifter suitable for application in an SPDT. Despite the increased insertion loss, the FoM reaches values between 60 °/dB to 66 °/dB for magnetic and 55 °/dB to 62 °/dB for electrical biasing above 100 GHz.

The WR10-to-sWL fibre transitions are still included in these measurement results. Measurements of the reference line in Fig. 6.9, being the same waveguide just without the LC section, resulted in transmission coefficients around −1.2 dB at 100 GHz. Therefore, the actual FoM of the sWL phase shifter in a fully dielectric system is much higher. Further, a measurement of a Rexolite sWL fibre with the same length as the phase shifter, thus being 26 mm longer than the reference line, revealed transmission coefficients around −1.7 dB at 100 GHz. Hence, the influence of the measured transitions is higher as the impact of the dielectric loss of LC. Consequently, the performance of the phase shifter can be improved by increasing the diameter of the LC cavity, by which the increase in phase shift will have a higher impact on the performance as the comparatively small increase in insertion loss.

Fig. 6.25 shows the phase shift provided by the sWL phase shifter, depending on the biasing condition of the electrical biasing system at 100 GHz. There, the unbiased state with $V_V = V_H = 0$ V on all biasing electrodes is chosen to be the state of 0° phase shift, since this is a well reproducible state.

It can be seen, that the main phase shift can be achieved even with lower voltages. 10 % to 90 % of the usable phase shift can already be achieved with $V_H = \pm 75$ V in the perpendicular case and $V_V = \pm 175$ V for the parallel orientation. Nevertheless, almost the complete phase shift, and therefore, the high voltages are needed for

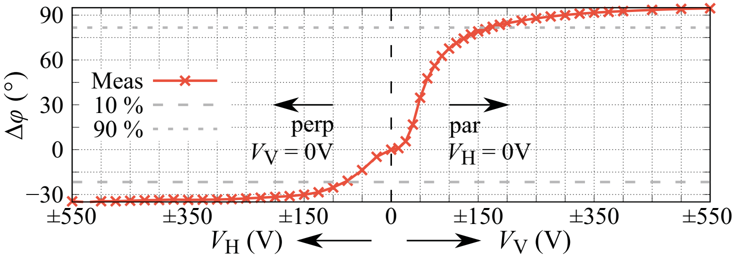

Figure 6.25: Supplied phase shift of the sWL phase shifter, depending on the biasing condition of the electrical biasing system at 100 GHz. On the left, the perpendicular orientation is given with V_H being effective, while the parallel orientation is given on the right where V_V is effective.

the first dielectric proof-of-concept SPDT, since the phase difference of the MMI coupler is less than expected from simulation. In the measurement, a saddle point is observed around the switch-off state of 0 V. There, a certain threshold voltage needs to be reached first, before the weak surface anchoring is overcome.

6.4.2 Step-Index Topology

Design & Realisation

When the application requires a higher phase shift, e.g. $\Delta\varphi \geq 360°$ for phased array antennas, a different dielectric waveguide topology is preferred, in which a bigger LC cavity can be implemented. The best solution is a step-index phase shifter design. There, the complete core material can be replaced by LC. The design of the step-index phase shifter investigated within this work is based on the preliminary design from the material evaluation in Fig. 6.10. As for all previous components, the WR10-to-sWL fibre transitions are used for the conversion of the TE_{10} mode to the E_{11}^{y} mode. After a short sWL fibre section the dielectric waveguide is widening up as cladding material while a tapered core section is included to the dielectric waveguide. After the propagating wave is sufficiently confined within the core material, it needs to be replaced by LC for tuneability.

However, Fig. 6.26 illustrates that the integration of LC as core material requires a further adaption of the step-index phase shifter. In case of a perpendicularly oriented LC, the permittivity of the core material would be with $\varepsilon_{\mathrm{LC},\perp} \approx 2.40$ lower than the one of the cladding material with $\varepsilon_{\mathrm{Rex}} = 2.53$. Total internal reflections cannot occur anymore and the field is not properly confined in the core material, resulting in an increased radiation with a simulated insertion loss of 10 dB to 16 dB

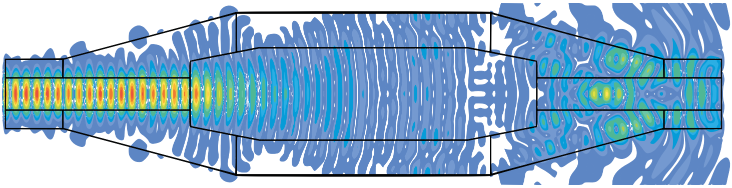

Figure 6.26: Field distribution of a step-index phase shifter design, where the core material was simply exchanged by LC. The simulation was carried out at 100 GHz with a core permittivity of $\varepsilon_{\mathrm{LC},\perp} = 2.40$ and a cladding permittivity of $\varepsilon_{\mathrm{Rex}} = 2.53$,

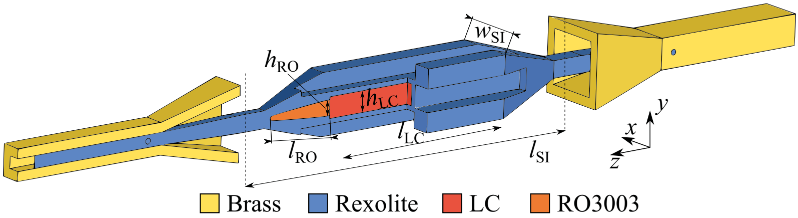

Figure 6.27: Schematic of the step-index phase shifter design. The most important dimensions are l_{SI} = 39.5 mm, w_{SI} = 6.5 mm, l_{LC} = 19.0 mm, h_{LC} = 2.2 mm, l_{RO} = 7.3 mm and h_{RO} = 1.6 mm.

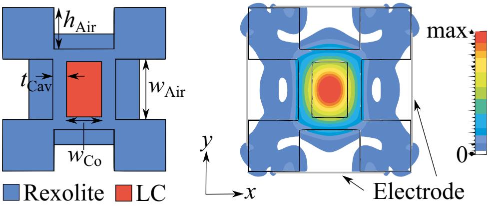

Figure 6.28: Schematic cross-section and field distribution of the step-index phase shifter's centre part in propagation direction. The simulation was carried out at 100 GHz with a core permittivity of $\varepsilon_{LC,\perp} = 2.40$ and a cladding permittivity of $\varepsilon_{Rex} = 2.53$. The most important dimensions are w_{Co} = 1.40 mm, w_{Air} = 2.40 mm, h_{Air} = 2.00 mm and t_{Cav} = 0.55 mm.

from 90 GHz to 110 GHz. To overcome this issue, additional air gaps were included in the cladding design to increase the difference in effective permittivity between the core and cladding material. The improved phase shifter design, its cross-section as well as field distributions are shown in Fig. 6.27, Fig. 6.28 and Fig. 6.29. The field is properly confined in the LC core section. However, a thin layer of Rexolite still needs to surround the core region to seal the LC inside. The layer at the top of the cavity has a filling hole, which will be sealed by glue after the LC filling.

With a length of l_{LC} = 19.0 mm, the length of the LC section was designed that a simulated phase shift of more than 360° can be provided above 90 GHz. The dimensions of the core at the boundary between RO3003 and LC are abruptly changing to always fulfil the propagation condition according to Marcatili's approximation. Furthermore, the complete cladding is designed in two halves only, as indicated in

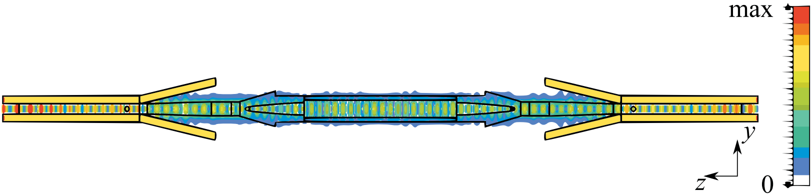

Figure 6.29: Field distribution of the final step-index phase shifter design, where air gaps are included to the cladding for a proper field confinement inside the core region. The simulation was carried out at 100 GHz with a core permittivity of $\varepsilon_{\mathrm{LC},\perp} = 2.40$ and a cladding permittivity of $\varepsilon_{\mathrm{Rex}} = 2.53$.

Fig. 6.27, to reduce the possibility of discontinuities along the dielectric waveguide. The splice will be in the y-z-plane. Compared to the sWL phase shifter this design also has the advantage that biasing electrodes can be directly mounted on the cladding material, since only negligible field components are propagating in these areas of the cladding material, as shown in Fig. 6.28. Thus, the mechanical stability of the biasing system is increased and no additional spacer material is required.

The two Rexolite halves as well as the core taper section made of RO3003 were realised by milling. For RO3003, first the copper coating was completely etched away before the taper was modelled. These taper were then placed in the recess provided in both cladding halves, before the phase shifter was glued. To provide a proper alignment of both cladding halves, four Rexolite alignment pins were added to the design. After the sealing, the LC cavity was filled through the filling

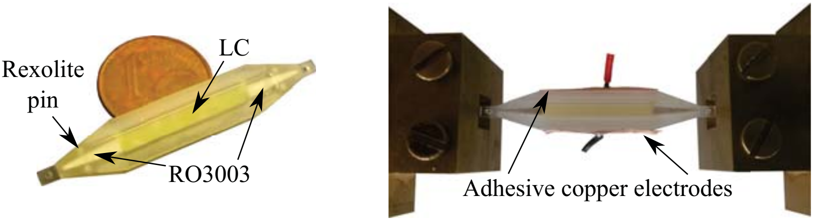

Figure 6.30: Photograph of the step-index phase shifter demonstrator. (left) the LC filled demonstrator is shown, which was measured using a magnetic biasing system as well as (right) an electric biasing system, comprising of 2 pair of adhesive copper electrodes. For the sake of clarity, only one pair of electrodes is shown here.

holes with the help of a syringe. The already LC filled demonstrator as well as the measurement setup including the electric biasing system is shown in Fig. 6.30.

Characterisation

A comparison of the simulated and measured results is given in Fig. 6.31. For the sake of clarity, only the results for the tuning state with highest insertion loss are shown. For magnetic biasing, the permanent magnets shown in Fig. 6.23 were used, while two pair of adhesive copper tape electrodes are functioning as the electric biasing system, being fed with voltages of ±550 V, as for the sWL phase shifter.

The matching $|S_{11}|$ is below -15 dB all over the measured frequency range and in accordance to the simulation. For the transmission coefficients, the measured results are deviating from the simulation about 1 dB to 2 dB. Values between -3.0 dB to -5.5 dB, where the electrically biased results show a slightly increased insertion loss compared with the magnetically biased ones. This is originating from the adhesive copper tape, which has at least a small impact on the evanescent field components in the cladding material. The deviation to the simulation is determined by the used UV glue as well as RO3003 taper, whose dielectric losses are not exactly determined for W-band, and therefore, only approximated in the simulation.

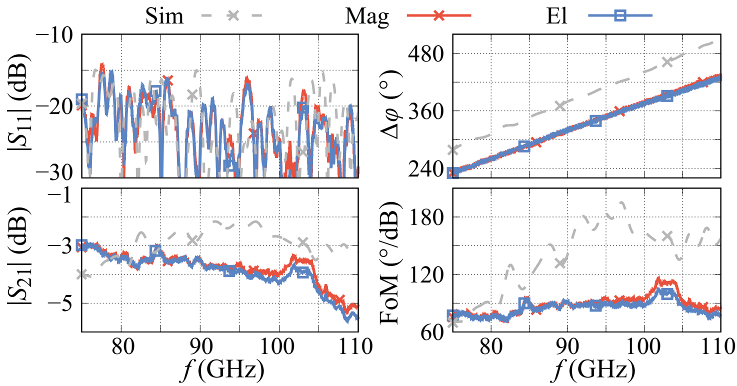

Figure 6.31: Simulated and measured (left) S-parameter, (right) phase shift and FoM results of the tuneable step-index phase shifter. The measurements are given in solid and the simulations in dashed lines.

Although the measured phase shifts are not matching the simulation, due to ideal LC alignment in CST Studio Suite, the measured phase shift for both biasing methods are matching very well to each other with values of 240° to 420° between 75 GHz to 110 GHz. The resulting FoM reaches values between 72 °/dB to 110 °/dB for magnetic and to 100 °/dB for electrical biasing.

These values are beyond the state-of-the-art for passive electrically tuneable phase shifters at W-band. Moreover, it is competitive to the magnetically biased waveguide phase shifter presented before, exhibiting an FoM around 120 °/dB. The tuneable dielectric waveguides are not only predestined for an application in a high-gain phased array antenna for W-band communication, but also for an application in the aimed mixed beam-switching and beam-steering network, where they can be implemented in a shorter version with less phase shift before each antenna element. Hence, the LC dielectric waveguide technology has proven to be promising alternative for the design of tuneable components in the (sub)millimetre wave regime. However, for the tuneable switches only small phase shifts are needed, which is why the focus in the last section will be again on the sWL topology.

6.5 Continuously tuneable SPDT

Design & Realisation

The fully dielectric SPDT comprises of the already investigated MMI power divider, MMI coupler, the sWL phase shifter as well as an additional sWL phase shifter. Because of the needed WR10 flanges for characterisation and the fact that gentle bends are needed for avoiding radiation, this demonstrator has a length of $l_{\mathrm{SPDT}} = 163.4\,\mathrm{mm}$ and a width of $w_{\mathrm{SPDT}} = 23.4\,\mathrm{mm}$, as presented in Fig. 6.32. The

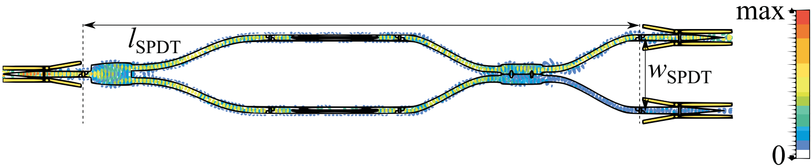

Figure 6.32: Simulation model including the field distribution for one extreme configuration of the tunable SPDT. It has a total length of $l_{\mathrm{SPDT}} = 163.4\,\mathrm{mm}$ and a width of $w_{\mathrm{SPDT}} = 23.4\,\mathrm{mm}$.

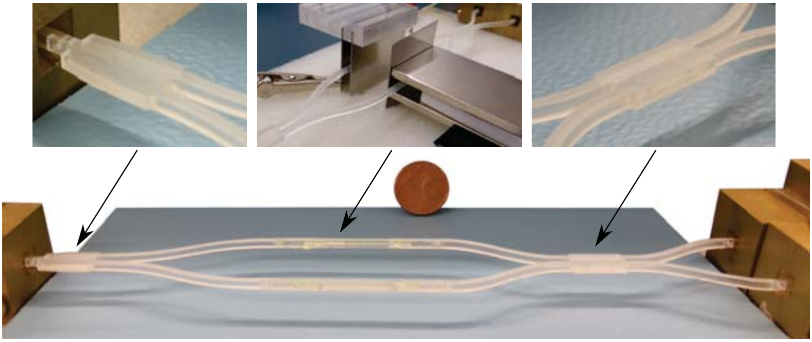

Figure 6.33: Final demonstrator of the continuously tuneable SPDT in dielectric fibre technology, including the biasing system. The unused port is terminated by a load during the measurement.

sub-components are designed with lugs that they can be connected to each other by means of Rexolite pins. By this, the use of lossy glues is reduced to a minimum. The final demonstrator as well as the used biasing system are shown in Fig. 6.33.

For the first proof-of-concept measurements, one of the phase shifters was aligned parallel with the help of permanent magnets, while the second phase shifter was electrically biased, since only one sufficient voltage source was available. By this, the best possible LC alignment was ensured, while at the same time the functional principle was not limited. Thus, one phase shifter was independently tuned by varying the biasing voltage while the second one was fixed. Due to the use of permanent magnets, the phase shifters needed to be sufficiently separated by 23.4 mm, resulting in a symmetric combiner design.

Fig. 6.34 gives the simulation and measurement results for the best performing biasing configurations of the dielectric proof-of-concept SPDT. There, for the optimum frequency of 98 GHz the best performing configurations in terms of highest isolation between both output ports and lowest insertion loss of the thru-port were achieved, when both phase shifters provide the maximum phase shift. This is the case if the LC in one phase shifter is magnetically aligned parallel while the second is electrically aligned in perpendicular orientation, using a biasing voltage of ±550 V. These extreme alignment states are needed to overcome the reduced phase difference of the MMI coupler.

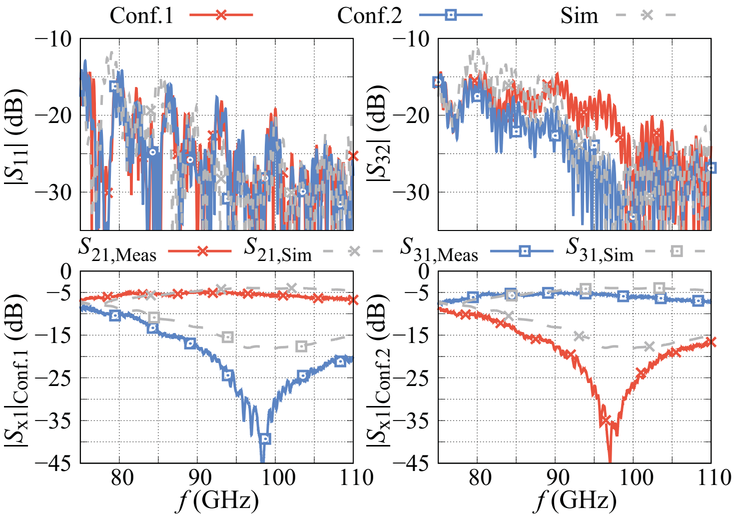

Figure 6.34: S-parameter simulation and measurement results of (top) the matching $|S_{11}|$, the output-to-output isolation $|S_{32}|$ as well as (bottom) the transmission coefficients of the best biasing configurations 1 (signal at port 2) and 2 (signal at port 3) of the continuously tuneable dielectric SPDT. The measurements are given in solid and the simulations in dashed lines.

$|S_{11}|$ matches the simulation well with values of −15 dB nearly over the complete measured frequency range and even below −20 dB above 100 GHz. The output-to-output isolations also match the simulation with values from 15 dB to 25 dB for both configurations. The difference between configuration 1 and 2 comprise from the re-connection of the sub-components.

For the first best biasing configuration, the insertion loss of the thru-port is always below 7 dB, with a minimum of 5 dB between 88 GHz to 95 GHz. This is at lower frequencies in a good agreement with the simulation, while there is a deviation of about 1.0 dB to 1.5 dB at higher frequencies. The isolated port in this configuration is better than simulated, being directly linked to the slightly increased loss of the thru-port. It shows a transmission coefficient below −15 dB above 86 GHz and even down to −30 dB around 100 GHz. This results in an isolation between $|S_{21}|$ and $|S_{31}|$ better than 15 dB over a bandwidth of 15 % and better than 25 dB over a bandwidth of 5 % from 96 GHz to 101 GHz.

For the second best biasing configuration, the thru-port results could be reproduced well. However, there is a small deviation in the isolation between $|S_{21}|$ and $|S_{31}|$ compared to configuration 1. The 15 dB bandwidth is around 10 %, while the 25 dB bandwidth reduces to 4 %. Nevertheless, these small deviations can already occur due to tolerances in the assembly process of the VNA extensions to the SPDT.

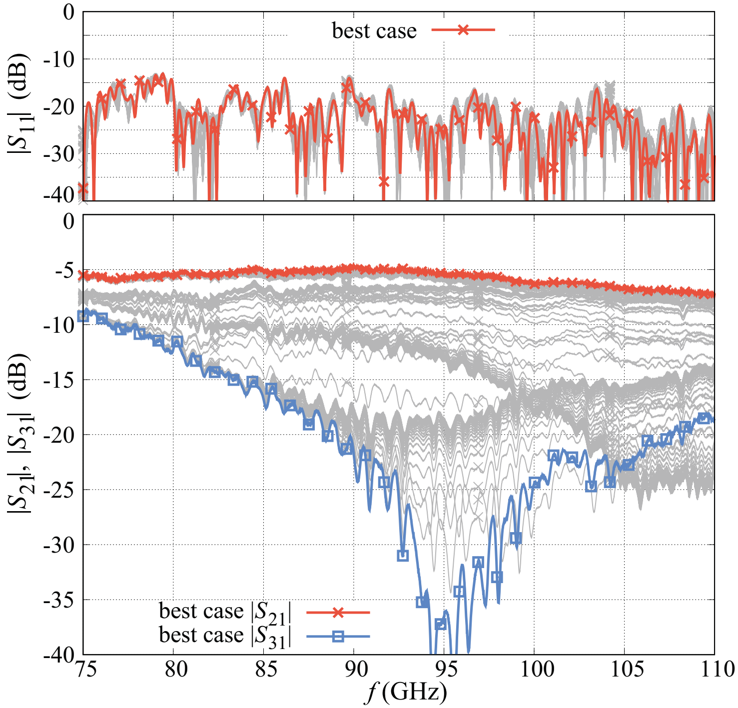

Figure 6.35: Measurement results of (top) the matching $|S_{11}|$ and (bottom) the transmission coefficients $|S_{21}|$ and $|S_{31}|$ for a complete sweep of one phase shifter of the tuneable SPDT. The second phase shifter was constantly kept in the parallel orientation by means of permanent magnets.

Also, for this SPDT the power splitting ratio can be adjusted to each preferred value between these two best biasing configurations. This continuous-state agility is a novelty for SPDTs in this frequency range, where most of the state of the art SPDTs are based on semiconductor or MEMS technology, being just switchable from on- to off-state. Moreover, the optimum configurations can also be shifted in frequency, at least in the range where enough phase shift can be provided.

Both, the frequency tuneability as well as the adjustable power splitting ratio can be observed from Fig. 6.35, where a voltage sweep for one phase shifter was carried out, while the second one was kept in parallel orientation by means of permanent magnets. The complete area is not homogeneously covered with measurement curves, since only 22 equidistant voltage steps were chosen for the measurement. By this, the changes in phase can be up to 15° between two measurements in the range where the phase shifters have their steepest slope (see Fig. 6.25), leading to a big change in $|S_{21}|$ and $|S_{31}|$ of the SPDT.

For these measurements, a new setup of the SPDT was used, which shows the reliability of this technology compared with the results from Fig. 6.34. The frequency shift leads to an isolation of at least 25 dB from 93 GHz to 110 GHz. Further, the input matching is only changing marginally over all tuning states. However, the difference in $|S_{21}|$ is not as significant as for $|S_{31}|$, since with increasing frequency less of the evanescent field components are propagating in air, which is why dielectric losses increase. This can be seen in Fig. 6.36 for an example of two different states.

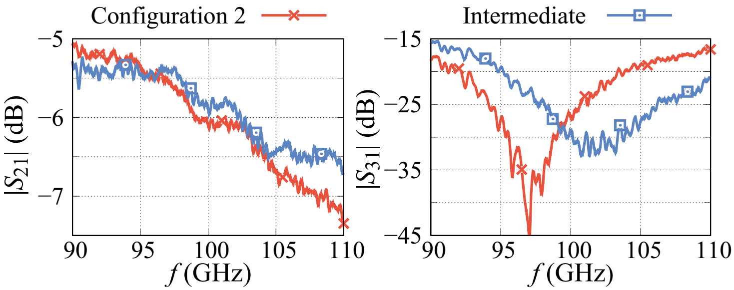

Figure 6.36: Measurement results for the frequency shift of the thru $|S_{21}|$ and isolation $|S_{31}|$ of the tuneable dielectric SPDT. The results of configuration 2 of Fig. 6.34 are compared with an intermediate state, where the biasing voltage of the electrically biased phase shifter was decreased, causing a shift of the centre frequency towards higher frequencies.

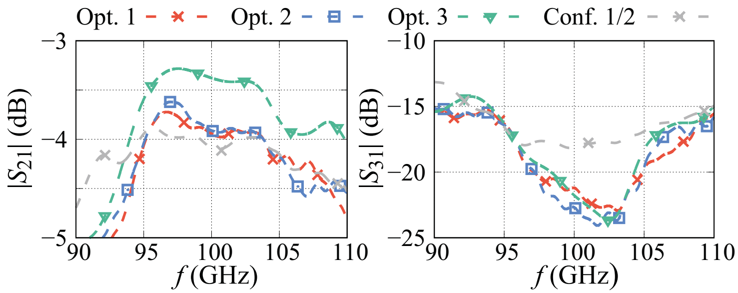

Figure 6.37: Simulation results of several optimisation steps of the dielectric fibre SPDT. Starting from the best biasing configuration (Conf.1/ 2), the first optimisation step (Opt. 1) was to adapt the width to a fully electrically biased SPDT. The second optimisation step (Opt. 2) was to increase the diameter of the LC cavity, resulting in a decreased total length of the phase shifters. The last optimisation step (Opt. 3) was to remove the WR10-to-sWL fibre transitions to give an impression of the performance of a fully dielectric system.

Small improvements of $|S_{21}|$ can be made out, but they are in average only around 0.2 dB and in maximum around 0.5 dB.

All the components used for the SPDT are radiation hard and very cost efficient. Additionally, the SPDT is very lightweight with an overall weight of less than 5 g without the WR10-to-sWL fibre transitions. The total size can be reduced for future applications where no magnetic biasing is needed anymore. Simulations have been carried out to visualize the effect of these optimisation steps. The results are given in Fig. 6.37.

In the first optimisation step, the separation of the branches was reduced to 10 mm, also reducing the length of the power divider/coupler branches by a factor of two. In the second step, the diameter of the LC cavity is increased from 0.6 mm to 0.8 mm. By this, the total length of the LC cavity can be decreased from 26.0 mm down to 15.3 mm. According to the simulations, these optimisations lead to an improvement in $|S_{21}|$ of around 0.2 dB to 0.3 dB. However, the biggest impact on the transmission coefficients have the WR10-to-sWL fibre transitions. By excluding them from the simulation, $|S_{21}|$ can be improved by 0.5 dB. Further, the isolation $|S_{31}|$ can be improved by these optimisations about 5 dB as well. Moreover, the space needed for the demonstrator is nearly reducing by a factor of four to 11.6 cm^3.

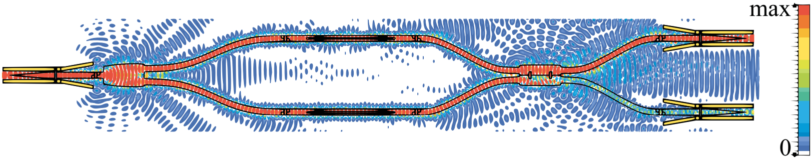

Figure 6.38: Simulated field distribution of the dielectric SPDT at 100 GHz. Compared to the field distribution presented in Fig. 6.32, lower field strengths are examined.

However, the influence of the WR10-to-sWL fibre transitions is expected to be higher than shown by these simulations, since the radiation caused by discontinuities is not taken into account during the simulations. This was already validated by the back-to-back measurements shown in Fig. 6.9, including the phase shifter's reference line, showing an insertion loss of about 1.0 dB to 1.6 dB.

Hence, the LC dielectric waveguide technology has proven to be well suitable for the realisation of tuneable W-band components. However, the SPDT showed a comparatively high insertion loss with up to 7 dB, originating from radiation due to bends. Especially at the MMI coupler section an increased radiation can be made out, originating from the asymmetrical feeding of the MMI main body, as can be seen in Fig. 6.38. Its length is not long enough to sufficiently form a MMI pattern when being asymmetrically excited. In this SPDT it is more acting as a coupled line combiner. According to the simulation at 100 GHz, 18 % of the stimulated field is radiated, while 42 % is detected at all output ports. Additionally, 37 % are lost due to dielectric and 3 % due to ohmic loss.

Therefore, for the realisation of complex tuneable *high-performance* W-band components, such as the mixed beam-switching and beam-steering network, a hybrid implementation of LC-tuned dielectric waveguide and non-tuneable low-loss metallic waveguide structures is the most promising solution, since radiation can be significantly reduced. By this, the advantages of both technologies can be combined.

6.6 SPDT in Hybrid Metallic and Dielectric Waveguide Topology

As a proof-of-concept for the hybrid implementation of LC-tuned dielectric and non-tuneable metallic waveguide structures, a tuneable SPDT demonstrator was designed, being directly comparable to the fully dielectric SPDT introduced before. For the power divider and coupler designs, the subcomponents from the metallic waveguide SPDT presented in section 5.3 were merged with the WR10-to-sWL fibre transitions introduced in sub-section 6.2.1. The design of the new split-blocks is shown in Fig. 6.39. As phase shifters, two sWL phase shifter as shown in sub-section 6.4.1 were used.

For each phase shifter, two WR10-to-sWL fibre transitions are needed, being the only possibility left for radiation to occur. The split-blocks are symmetrically designed as for the metallic waveguide SPDT with a cut in the E-plane. Compared to the fully dielectric SPDT, the total length of the hybrid demonstrator is decreasing from $l_{\mathrm{SPDT,Diel}} = 220.0\,\mathrm{mm}$ to $l_{\mathrm{SPDT,Hyb}} = 170.5\,\mathrm{mm}$, including the sWL phase shifters. The simulated field distribution of the hybrid SPDT is shown in Fig. 6.40.

It is obvious that radiation is not an issue anymore. This is also confirmed by the simulation results, predicting a radiation loss of only 0.4 %, while the dielectric and ohmic losses are at 20.2 % and 12.0 %, respectively. The complete power outgoing

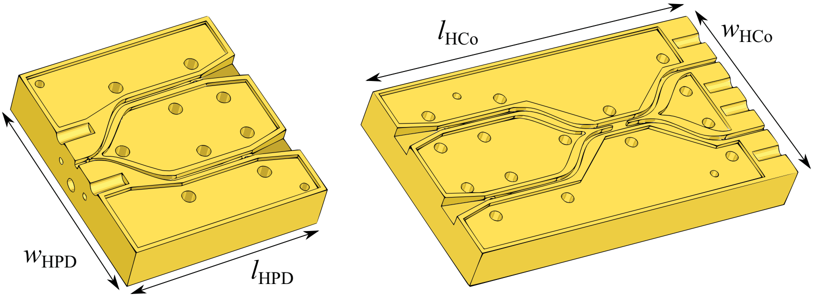

Figure 6.39: Design of the (left) power divider and (right) coupled line combiner split-blocks for the hybrid SPDT, including the WR10-to-sWL fibre transitions. The most important dimensions are $l_{\mathrm{HPD}} = 45.5\,\mathrm{mm}$, $w_{\mathrm{HPD}} = w_{\mathrm{HCo}} = 50.0\,\mathrm{mm}$ and $l_{\mathrm{HPD}} = 85.0\,\mathrm{mm}$.

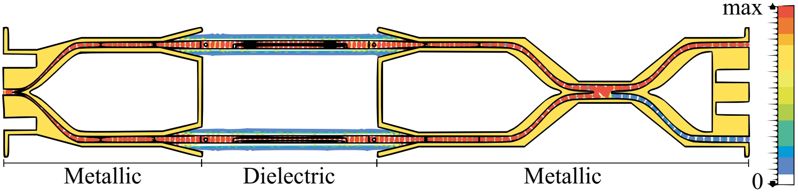

Figure 6.40: Simulated field distribution of the hybrid SPDT at 100 GHz. As in Fig. 6.38, low field strengths are examined.

at all ports was simulated to 67.4 %. A photograph of the realised demonstrator is given in Fig. 6.41.

In Fig. 6.42, the measurement results of the hybrid SPDT are directly compared with the one from the fully dielectric SPDT. The phase shifters were filled with the LC mixture GT5-26001. The matching $|S_{11}|$ of the hybrid SPDT is below -10 dB from 80 GHz to 110 GHz and except a small resonance at 90 GHz even around -15 dB,

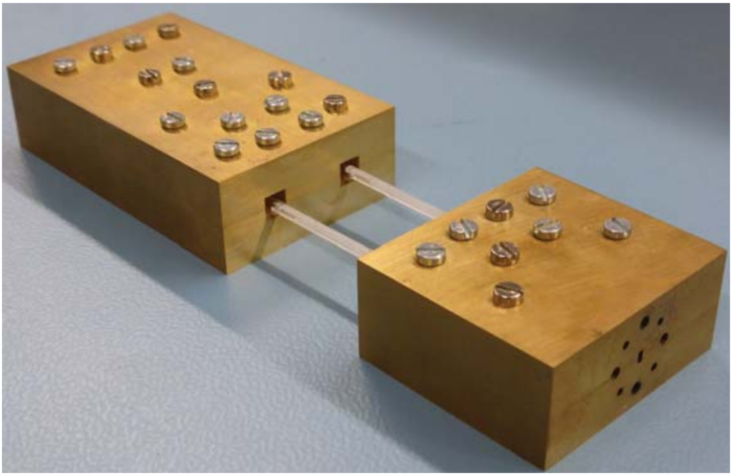

Figure 6.41: Final demonstrator of the hybrid SPDT in metallic and dielectric waveguide topology.

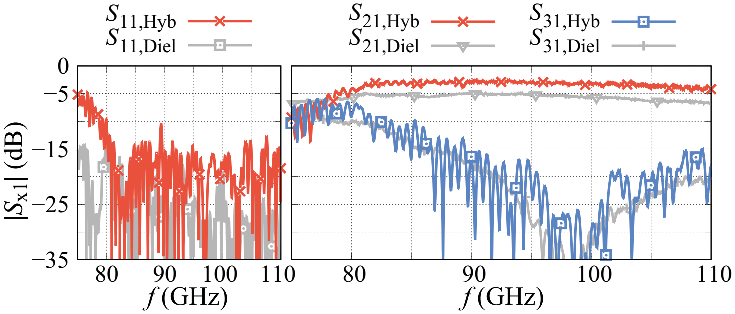

Figure 6.42: Measurement results of (left) the reflection and (right) the transmission coefficients of the hybrid SPDT in comparison with the measured results of configuration 1 from the fully dielectric SPDT shown in Fig. 6.34.

being in an excellent agreement with the simulations (not shown in the plot). With these values it is not as ideally matched as the dielectric SPDT, but better matched as the fully metallic SPDT. This originates from the partially possible radiation at the WR10-to-sWL fibre transitions.

The biggest advantage of this hybrid implementation is revealed by the transmission coefficients. The hybrid SPDT shows an insertion loss of 3 dB to 4 dB between 80 GHz to 110 GHz, being an improvement of 2 dB to 3 dB compared to the fully dielectric SPDT. At the same time, the isolation $|S_{31}|$ for both SPDTs is comparable except the rippled shape of the hybrid SPDT's results. Compared to the simulation, the insertion loss is increased about 0.7 dB in average, while the isolation is matching the simulation nearly perfectly. A detailed comparison of the hybrid SPDT also to the simulation and waveguide SPDT results is given in appendix A.3. Furthermore, the continuously adjustable power splitting ratio as well as the frequency tuneability are also applicable with this demonstrator.

6.7 Comparison of Tuneable SPDTs at W-Band

In literature, SPDTs are mostly evaluated by the difference between the insertion loss as well as the isolation. Since this difference is only expressive in connection with the insertion loss, a figure of merit for SPDTs ($\mathrm{FoM}_{\mathrm{SPDT}}$) is defined at this point as the difference between the isolation ($|S_{31}|$ in dB) and the insertion loss ($|S_{21}|$ in dB), divided by the insertion loss

$$\mathrm{FoM}_{\mathrm{SPDT}} = \frac{|S_{31}| - |S_{21}|}{|S_{21}|} . \tag{6.32}$$

By this, the importance of the insertion loss on the overall performance is sufficiently taken into account. Especially in logarithmic scale, a high isolation can be easily achieved when the insertion loss is already high. The FoMs of the SPDTs investigated in this work are presented in Fig. 6.43. Further, Table 6.1 and Table 6.2 are giving selections of state-of-the-art SPDTs for Ka- and W-band, respectively.

It is obvious that the LC-tuned LTCC SPDTs investigated in this work are not competitive with state-of-the-art SPDTs in the Ka-band, although an isolation between thru and isolated port of more than 35 dB was achieved. The interference-based principle in combination with the LTCC technology is too lossy compared to conventional approaches in this frequency range. However, this is different for W-band frequencies, where the competing technologies face increasing losses, resulting in decreased SPDT FoMs. The hybrid SPDT shows the best results of all investigated SPDT implementations within this work. Although it is not reaching the FoM of the tuneable SiGe SPDTs, it is, nevertheless, competitive with the state-of-the-art SPDTs. Exemplarily, they revealed a higher FoM than the commercially available

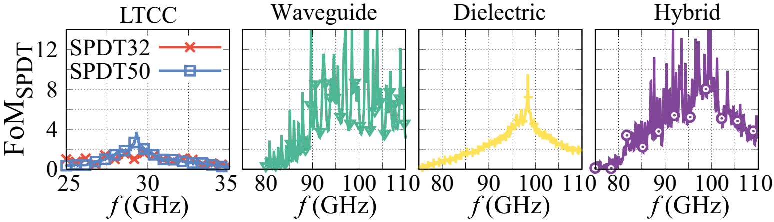

Figure 6.43: FoM for the SPDTs investigated within this work. The values are calculated out of the measured results discussed before.

Table 6.1: Performance summary of state of the art Ka-band SPDTs.

Reference	Technology	*f* (GHz)	IL (dB)	Isol. (dB)	FoM_{SPDT}
[Zhe+13]	GaN	30	1.2	27.0	21.5
[Guo+15]	GaN	35	1.9	27.7	13.6
[Poh+12]	SiGe	30	3.0	25.0	7.3
[Che+16]	SiGe	32	3.3	21.8	5.6
[Min+08]	CMOS	35	2.2	32.0	13.6
[Liu+14]	CMOS	30	2.7	33.0	11.2
[Zah+15]	MEMS	30	0.8	40.0	49.0
[Kum+12]	PIN Diode	36	1.0	39.0	38.0
This work	**LC LTCC (32)**	**30**	**9.4**	**26.5**	**1.8**
This work	**LC LTCC (50)**	**29**	**11.0**	**48.0**	**3.4**

Table 6.2: Performance summary of state of the art W-band SPDTs.

Reference	Technology	*f* (GHz)	IL (dB)	Isol. (dB)	FoM_{SPDT}
[Sch+14]	SiGe	100	1.4	19.0	12.6
[Ulu+15]	SiGe	100	2.1	26.0	12.4
[Tom+10]	CMOS	100	4.0	25.0	5.5
[Cha+07]	CMOS	90	3.5	28.0	7.0
[May+10]	CMOS	100	2.5	21.0	7,4
[Rey+12]	MEMS	70	4.0	14.0	2.5
[Inc17c]	PIN Diode	95	5.5	40.0	6.3
[Inc17b]	PIN Diode	100	5.5	21.0	2.8
This work	**LC Waveguide**	**95**	**2.6**	**19.6**	**6.5**
This work	**LC Dielectric**	**98**	**5.5***	**35.0**	**5.4**
This work	**LC Hybrid**	**100**	**3.0**	**27.0**	**8.0**

*: including the metallic WR10-to-sWL fibre transitions

waveguide based PIN diode SPDTs. Further, the size and performance are still improvable and the complete technology is easily scalable to higher frequencies.

These facts and the perspective of an in-plane realisation of the network, comprising of a miniaturised low-loss metallic Butler matrix, high-performance dielectric phase shifters as well as an SPnT in hybrid metallic and dielectric waveguide technology, represent the most promising solution for the realisation of complex electrically controlled LC beam-switching and beam-steering networks at W-band.

7 Conclusion and Outlook

The ever-increasing demand for higher data rates requires RF communication systems to operate at higher frequencies, where larger bandwidths can be exploited. For that reason, a tuneable high gain mixed discrete beam-switching and continuous beam-steering network based on microwave liquid crystal (LC) technology has been systematically investigated for millimetre wave, and especially, W-band frequencies in this work, since they are insufficiently used for communication up to now. Due to the increasing atmospheric impairments as well as free-space path loss with increasing frequency, antenna systems with highly directional pencil beams are preferred. An adaptive beam-steering is required (i) for compensating possible shifts of these narrow beams, but in particular (ii) for portable and slow tracking applications, which is realisable by the use of tuneable LC components. By changing the orientation of the LC molecules with respect to the applied RF field, the effective permittivity of the transmission line or waveguide changes, resulting in a tuneable delay line. This technology has the advantage of being fully electrically tuneable, by which wear-out failures are negligible. Further advantages are the continuous tuneability, the high linearity of LC components, its low power consumption as well as the material-specific low dielectric loss, making the LC technology even suitable for future wideband applications at higher frequencies up to several THz. While former investigations have always been focussed on the common phased array approach, e.g. [Kar14; Gae15; Wei17], this work is dealing with an innovative approach based on a Butler matrix combined with tuneable phase shifters. The loss from phase shifting are kept on a low level, since only about 1/3 of the phase shift compared with conventional phased array antennas is required, originating from the combination of *discrete beam-switching* and *continuously beam-steering*. For beam-switching, different input ports of the Butler matrix need to be selected, for which a new type of switch is introduced in this work: an interference-based SPnT with continuously adjustable power-splitting ratio. The adjustable power-splitting ratio allows not only the selection of different inputs, but also the excitation of more than one input at the same time, resulting in multiple beams. Additionally, the tuneability allows the operational frequency to be shifted, making this SPDT applicable in a broad frequency range.

With screen-printed low temperature co-fired ceramic (LTCC) multilayer components as well as milled metallic and dielectric waveguide components, different implementations had been investigated for Ka- and W-band, respectively. The demonstrators in LTCC technology within the research project *Liquida K*, funded by the German Aerospace Center, were designed for Ka-band frequencies around 30 GHz for a first proof-of-concept. With the presented designs for the tuneable LC-tuned LTCC single-pole double throws (SPDTs), all components being required in a mixed beam-switching and beam-steering network had been discussed. Hybrid couplers, tuneable and static phase shifters as well as DC blocking structures, which are suitable for an easy crossover realisation, are already implemented within the tuneable SPDTs, with which the concept was proven. Although tuneable LC components can be easily integrated into LTCC multilayer structures, the applicability of the used LTCC routine at W-band is difficult, because of screen-printing limitations as well as a high insertion loss, e.g. 10 dB at 30 GHz. While the screen-printing limitations are arising from the high permittivity of the green tape, the high insertion loss originates from the bad conductivity of the available gold paste.

Therefore, for the provision of a high gain mixed beam-switching and beam-steering network at W-band frequencies, the usability of low-loss metallic waveguide components was examined. The presented in-plane realisation of a Butler matrix is based on a novel waveguide crossover with dielectric star inset. This crossover not only allows a simple but also a very compact design for future Butler matrix realisations, due to the combined applicability as crossover and fixed phase shifter. Further, a tuneable phase shifter was introduced with an outstanding FoM around 135 °/dB at 100 GHz. The SPDT exhibits an insertion loss of 2.6 dB and an isolation of 19.6 dB around 95 GHz. However, both tuneable demonstrators were solely magnetically biased. The implementation of an electric biasing system within the limited space of a dielectrically filled waveguide at W-band occurred to be very challenging, for which a new type of low-loss tuneable LC waveguide has to be investigated.

Dielectric waveguides have pointed out as an excellent alternative to metallic waveguides. They are low-loss waveguides, which are not limiting the electrode design by any metallic boundaries. A qualitative material study was conducted and two major dielectric waveguide topologies have been investigated: the subwavelength fibre and the step-index dielectric waveguide. Where the subwavelength topology allows an easy realisation of tuneable LC phase shifter, the step-index topology reveals a higher performance of up to 100 °/dB at 102 GHz, being beyond the state-of-the-art for passive electrically biased phase shifters at W-band. For the fully dielectric SPDT design in subwavelength topology, specifically adapted multimode interference power divider and coupler have been combined with subwavelength phase shifters. The SPDT performed well with an insertion loss around 5.5 dB and an isolation of

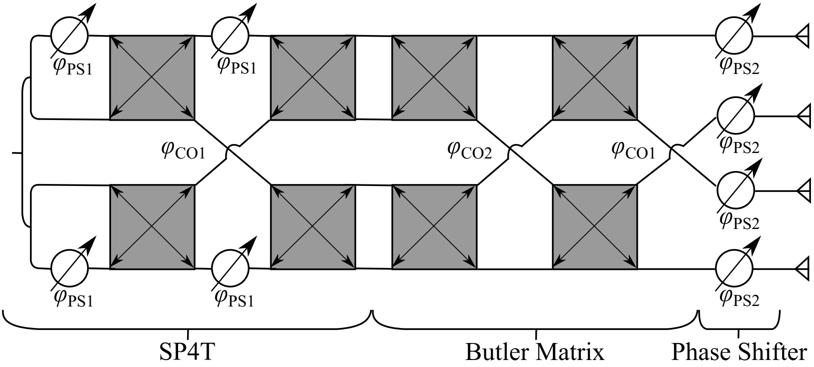

Figure 7.1: Final schematic design of the investigated mixed beam-switching and beam-steering network in LC hybrid metallic and dielectric waveguide technology. In this design, the phase shifters need to provide a phase shift of $-90° \leq \varphi_{\mathrm{PS1}} \leq 90°$ and $0° \leq \varphi_{\mathrm{PS2}} \leq 135°$, while the crossover need to provide a phase difference of $\varphi_{\mathrm{CO1}} = 0°$ and $\varphi_{\mathrm{CO2}} = 45°$ compared to the adjacent waveguides.

35.0 dB at 98 GHz. Nevertheless, an increased unintended radiation was made out at the power divider and especially the coupler section.

To allow an in-plane realisation of the overall mixed network on the same technology platform and to prove the high potential of the hybrid metallic and dielectric waveguide technology, a hybrid SPDT implementation was introduced, combining the advantages of low-loss metallic power dividing/combing structures as well as electrically tuneable low-loss dielectric phase shifters. In this implementation, radiation is not an issue anymore and the SPDT demonstrator showed an insertion loss of only 3 dB and an isolation of 27 dB at 100 GHz. This is an excellent result for W-band frequencies, with which it is competitive to the state-of-the-art SPDTs at W-band.

The final schematic design of the W-band mixed beam-switching and beam-steering network is introduced in Fig. 7.1. A hybrid implementation is chosen, where non-tuneable and tuneable components will be realised in metallic and dielectric waveguide technology, respectively. The main novelty is that this design allows an in-plane realisation of the complete mixed beam-switching and beam-steering network on one single technology platform. While the novel multifunctional crossover design presented in section 5.1 allows a miniaturised low-loss realisation of the beam-switching Butler matrix, the dielectric step-index phase shifters, whose performance is exceeding the state-of-the-art performances for passive electrically tuneable phase shifters at W-band, provide a low-loss continuous beam-steering. Further, an innovative SP4T design is included to the final design. Instead of cascading SPDTs, which would require six independently tuneable phase shifters as well as a lot of space, this design only requires four phase shifters due to the implementation of the novel crossover design. These phase shifters are only placed in the outer branches, which allows a small-volume, and therefore, low-loss realisation of the SP4T. According to the first investigations on a hybrid SPDT in section 6.6, this SP4T will at least be competitive with state-of-the-art SP4Ts, e.g. in semiconductor or MEMS technology, and will allow the in-plane realisation of the complete 1×4 mixed beam-switching and beam-steering network. As antenna elements, dielectric tapered rod antennas as introduced in [Kob+82] will be used subsequent to the dielectric phase shifters.

Hence, due to the novel crossover design the size can be reduced to a minimum and is mainly depending on the phase shifter sizes. Also, the width of this mixed beam-switching and beam-steering network is reduced, since only one WR10 flange is needed. The presented phase shifter topologies will be further optimised, e.g. by increasing the diameter of the LC cavity in the subwavelength phase shifter for size reduction. Further, new topologies as well as sophisticated biasing concepts are recently under investigation within a research project[1] funded by the German Research Foundation (Deutsche Forschungsgemeinschaft, DFG). In addition, the realisation of mixed beam-switching and beam-steering networks for millimetre wave applications is recently under further investigations on three different level:

- On the **component level**, high-performance waveguides with almost no radiation, the parallel plate dielectric waveguide (PPDW) and non-radiative waveguide (NRD), have recently come into focus. Both topologies are based on a dielectric waveguide, being extended by a pair of parallel metal plates. Where the plates of the PPDW are added in the H-plane, they are added in the E-plane for the NRD. Therefore, modes are better confined due to the additional boundary, and especially for the NRD, the mode is not propagable outside the dielectric core of the waveguide. The simulated field distributions for both waveguides are given in Fig. 7.2. First electrically biased V-band demonstrators are exhibiting FoMs around 75 °/dB and 110 °/dB [Ree+17b] for the NRD and PPDW, respectively. Also, the response times are decreased

---

[1] JA 921/68-1

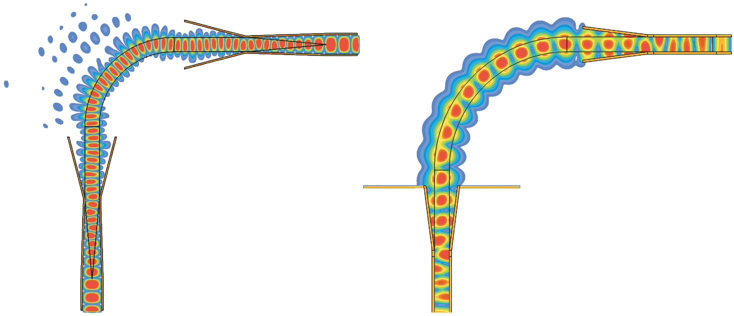

Figure 7.2: Simulation and field distribution of a bended (left) parallel plate dielectric and (right) non-radiative waveguide at 70 GHz. The radius of the bending was chosen to $r = 16\,\mathrm{mm}$.

compared with the presented dielectric waveguides, since the biasing electrodes can be directly placed on the metallic plates. Due to their hybrid metallic and dielectric design, they are very well suited for the in-plane realisation of the mixed beam-switching and beam-steering network in hybrid metallic and dielectric waveguide technology.

- On the **fabrication level**, the realisation of beam-steering networks can be even simplified by the use of additive manufacturing techniques. While 3D printed metallic waveguides are frequently discussed for millimetre wave applications [Zha+17; She+17; Bon+17], first attempts of 3D printed (non-)

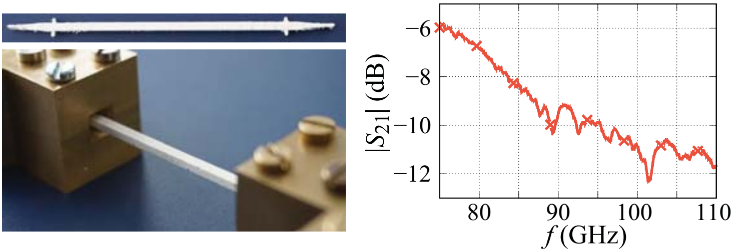

Figure 7.3: (left) Demonstrator and (right) measured results of the insertion loss for a 3D printed sWL fibre.

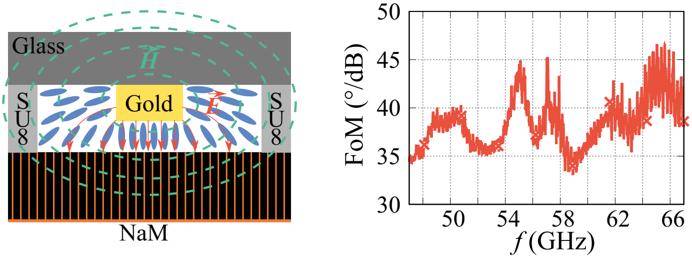

Figure 7.4: (left) Schematic principle and (right) measured FoM results of the slow-wave phase shifter. The NaM is comprising of a porous alumina membrane with nanowires made of copper as well as a copper ground at the backside.

tuneable sWL fibres were recently conducted (see Fig. 7.3). The big advantage of this technique is that only one single fabrication step and no additional glue would be needed. However, the accuracy of the milling process cannot be met and the implementation of an LC channel to the fibre design is challenging. First non-tuneable sWL fibres were realised out of a commercial ABS plastic using a Prusa i3 printer with 100 µm nozzle. Measured transmission coefficients between −6 dB to −12 dB from 75 GHz to 110 GHz reveal the actual disadvantage of this technique: missing printable low-loss dielectric materials.

- On the **technology level**, one could think of implementing the tuneable SPnT in semiconductor technology. As shown in table 6.2, they are exhibiting the highest FoM for SPDTs. However, it must first be determined that the additional transition from semiconductor devices to waveguides is not too lossy to lose the benefit from a low-loss SPnT.
  Further, a very promising alternative for the miniaturised realisation of beam-steering networks with low response times is under investigation by means of the *liquid crystal - nanowire filled membrane* (LC-NaM) technology. A microstrip line topology in combination with the NaM reveals a slow-wave effect, resulting in a decrease of the phase velocity. By this, a higher phase shift is achieved over the same physical length. Further, the increase of the transmission line's effective permittivity allows a realisation of LC cavities with heights in the range of a few µm, only. This results in very low response times according to equation (2.31), making this LC-NaM technology applicable for on-the-move applications. First demonstrators, investigated within a research

project[2] funded by the German Research Foundation, exhibited a measured phase shifter FoM of up to 45 °/dB at V-band (see Fig. 7.4), accompanied with response times in the range of ms. The planar topology also allows a very cost-efficient realisation, since the fabrication methods of the LC display technology can be directly adapted. In the upcoming *BESTSHIFT*[3] project, also funded by the German Research Foundation, beam-steering systems based on the LC-NaM technology will be investigated for 140 GHz communication systems.

---

[2] JA 921/58-1

[3] JA 921/65-1

A Appendix

A.1 Dimensions of the LC-tuned LTCC Components

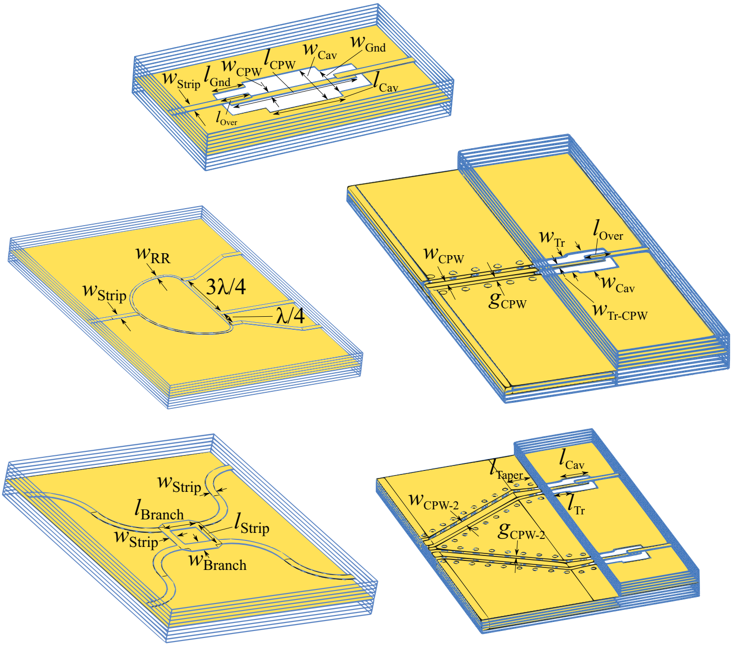

Figure A.1: Schematic of all single components used for the design of the LC-tuned LTCC SPDTs.

Table A.1: Most important dimensions of the above components shown in Fig. A.1. All dimensions are given in mm.

Embedded		Open	
w_{Strip}	0.211	w_{CPW}	0.220
w_{RR}	0.100	g_{CPW}	0.170
l_{Over}	0.780	$w_{\text{CPW-2}}$	0.400
w_{GND}	1.100	$g_{\text{CPW-2}}$	0.200
l_{GND}	0.950	l_{Taper}	1.000
w_{CPW}	0.200	l_{Over}	0.700
l_{CPW}	3.600	w_{Tr}	0.870
w_{Cav}	1.552	l_{Tr}	0.950
l_{Cav}	1.900	$w_{\text{Tr-CPW}}$	0.160
w_{Branch}	0.368	w_{Cav}	1.133
l_{Branch}	1.019	l_{Cav}	1.050
l_{Strip}	0.954		

A.2 Roughness Parameter

- The **arithmetical mean deviation** R_a gives the average difference to the centre line. The centre line is defined in the way that the sum of the overall profile is minimal ($\sum_{i=1}^{n} y_i = 0$).

$$R_\mathrm{a} = \frac{1}{n} \sum_{i=1}^{n} |y_i| \tag{A.1}$$

- The **root-mean-squared (rms) roughness** R_q gives the square mean value of the profile deviation. It is more sensitive to single peaks and dips as the arithmetical mean deviation.

$$R_\mathrm{q} = \sqrt{\frac{1}{n} \sum_{i=1}^{n} y_i^2} \tag{A.2}$$

- The **mean roughness depth** R_z is the average difference between the highest peak and the lowest dip of five measured sampling lengths. Also R_z is more sensitive to profile changes than R_a

$$R_\mathrm{z} = \frac{1}{5} \sum_{i=1}^{5} R_{\mathrm{z},i} = \frac{1}{5} \sum_{i=1}^{5} \Delta y_{\mathrm{max},i} \tag{A.3}$$

  Further, R_max is the maximum roughness depth of $R_{\mathrm{z},i}$.

- The **total roughness depth** R_t gives the difference between the highest peak and the lowest dip along the overall measured length.

A.3 Hybrid SPDT in Comparison

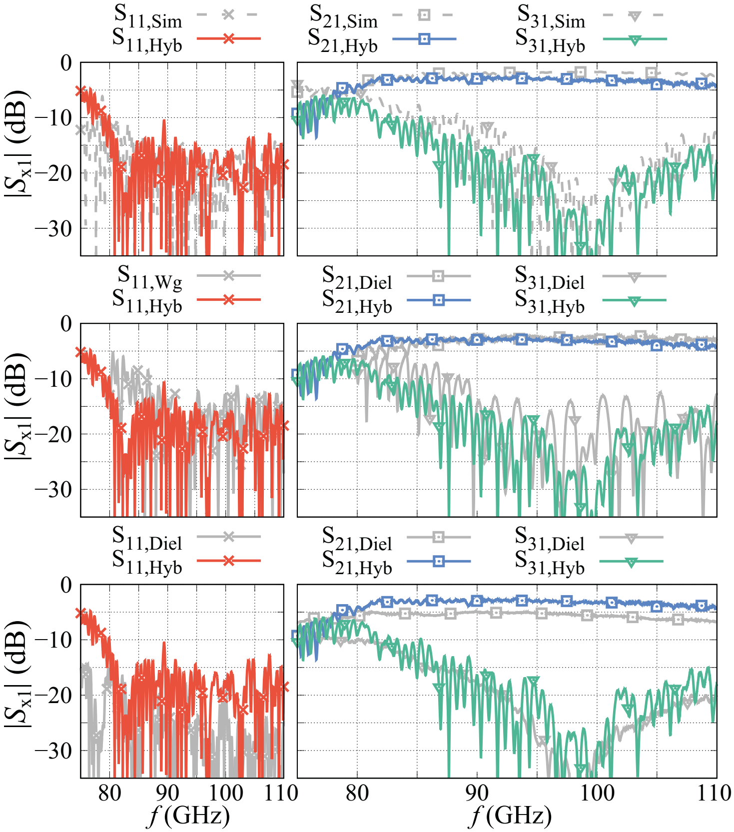

Figure A.2: Comparison of the (top) simulated and measured results of the hybrid SPDT, (middle) measured results of the waveguide and hybrid SPDT as well as (bottom) measured results of the dielectric and hybrid SPDT.

Symbols and Abbreviations

$\vec{a}$	Orientation of a single liquid crystal molecule
$\underline{a}_1$	Incident power wave
α	Attenuation
Au	Gold
$\underline{b}_1$	Reflected power wave
Bandw.	Bandwidth
BST	Barium-strontium-titanate
β	Propagation/phase constant
C	Capacitance per length
CMOS	Complementary metal-oxide-semiconductor
cos	Cosine
$\vec{B}$	Magnetic induction
CPW	Coplanar waveguide
Cu	Copper
d	Distance/diameter
$\vec{D}$	Dielectric displacement
dB	Decibel
DC	Direct current
$\delta_{\alpha\beta}$	Kronecker delta
$\Delta\varphi$	Differential phase shift
$\vec{E}$	Electric field
El	Electric
E_{Th}	Threshold electric field

η_{LC}	Material quality factor of LC
ε	Permittivity
ε_0	Electric constant
eV	Electronvolt
f	Frequency
F	Total free energy
f_{bend}	Bend energy density
f_{el}	Electric energy density
$f_{\mathrm{elast.}}$	Elastic energy density
f_{mag}	Magnetic energy density
f_{splay}	Splay energy density
$f_{\mathrm{surf.}}$	Surface energy density
f_{twist}	Twist energy density
$f(\Theta,\Phi)$	Orientational distribution function
FoM	Figure-of-merit for passive phase shifters
$\mathrm{FoM}_{\mathrm{SPDT}}$	Figure-of-merit for SPDTs
g	Gap width
G	Conductance per length
γ	Complex propagation constant
γ_{rot}	Rotational viscosity
$\Gamma_{\mathrm{diss.}}$	Dissipative torque
$\Gamma_{\mathrm{elast.}}$	Torque induced by elastic deformation
Γ_{field}	Torque induced by external field
GaAs	Gallium arsenide
GaN	Gallium nitride
Gbit	Gigabit
GHz	Giga Hertz
GSG(SG)	Ground-signal-ground(-signal-ground)
h	Height

$\vec{H}$	Magnetic field
$\mathbb{1}$	Identity matrix
IL	Insertion loss
Isol.	Isolation
k_B	Boltzmann constant
K_ii	Frank elastic constants
l	Length
L	Inductance per length
λ	Wavelength
LC	Liquid crystal
LCD	Liquid crystal display
L_π	Beat length
LTCC	Low temperature co-fired ceramic
$\vec{M}$	Magnetisation
μ	Magnetic permeability
μ_0	Magnetic constant
μ_r	Relative permeability
Mag	Magnetic
Meas	Measurement
MEMS	Micro-electro-mechanical systems
MMI	Multimode interference
MMIC	Monolithic microwave integrated circuits
N	Integer number (e.g. of liquid crystal molecules)
n	Refraction index
$\vec{n}$	Director
NA	Numerical aperture
$\vec{\nabla}$	Nabla operator
ν	orientational interaction constant
ω	Angular frequency

$\vec{P}$	Polarisation
φ	Phase
Φ	Azimuthal angle
par	Parallel
perp	Perpendicular
$\perp$	Perpendicular
$P_2(\cos\Theta)$	Second order Legendre-polynomial
$\Psi(...)$	Field distribution
PTFE	Polytetrafluoroethylene
PVC	Polyvinyl chloride
$Q_{\alpha\beta}$	Order parameter tensor
R	Resistivity per length
$R_{...}$	Roughness
RF	Radio frequency
RFIC	Radio frequency integrated circuit
RTPS	Reflection type phase shifter
s	Second
S	Order parameter
$\mathbf{S}$	Scattering matrix
S_{xy}	Scattering parameter
SI	Step-index
SiGe	Silicon-germanium
Sim	Simulation
sin	Sine
SIW	Substrate integrated waveguide
SPDT	Single-pole double-throw
sWL	Subwavelength
T	Temperature
τ_{LC}	Material tuneability of LC

τ_{off}	Switch-off response time
τ_{on}	Switch-on response time
τ_{φ}	Steering efficiency
ϑ	Normalised temperature
Θ	Polar angle
T_{c}	Clearing temperature
$\tan\delta$	Dielectric loss
TDS	Time domain spectroscopy
TE	Transverse electric
TEM	Transverse electromagnetic
THz	Terahertz
TM	Transverse magnetic
T_{m}	Melting temperature
V_{B}	Biasing voltage
V_{Th}	Threshold voltage
$V(\Theta)$	Single molecule potential
VNA	Vector network analyser
w	Width
χ_{e}	Electric susceptibility
χ_{m}	Magnetic susceptibility
Z	Molecule partition function

Bibliography

[AST11] ASTAP. *APT Report on Technology Trends of Telecommunications Above 100GHz*. Edited by Expert Group on Millimeter-Wave Communication System. 2011. URL: `http://www.apt.int/sites/default/files/Upload-files/ASTAP/Rept-4-Technology%20Trends%20above%20100GHz.pdf`.

[Ata+13] S. Atakaramians, S. V. Afshar, T. M. Monro, and D. Abbott. “Terahertz dielectric waveguides”. In: *Adv. Opt. Photon.* 5.2 (June 2013), pages 169–215. DOI: `10.1364/AOP.5.000169`.

[Bac+94] M. Bachmann, P. A. Besse, and H. Melchior. “General self-imaging properties in NxN multimode interference couplers including phase relations”. In: *Appl. Opt.* 33.18 (June 1994), pages 3905–3911. DOI: `10.1364/AO.33.003905`.

[Bal+07] C. A. Balanis and P. I. Ioannides. *Introduction to Smart Antennas*. Morgan & Claypool Publishers, 2007, pages 1–175.

[Bar+06] M. Barba, J. E. Page, J. A. Encinar, and J. R. Montejo-Garai. “A Switchable Multiple Beam Antenna for GSM-UMTS Base Stations in Planar Technology”. In: *IEEE Transactions on Antennas and Propagation* 54.11 (Nov. 2006), pages 3087–3094. DOI: `10.1109/TAP.2006.883991`.

[Bar+98] N. S. Barker and G. M. Rebeiz. “Distributed MEMS true-time delay phase shifters and wide-band switches”. In: *Microwave Theory and Techniques, IEEE Transactions on* 46.11 (Nov. 1998), pages 1881–1890. DOI: `10.1109/22.734503`.

[Bhu+17] A. Bhutani, B. Goettel, T. Thelemann, and T. Zwick. “CPW-to-SL transition in LTCC technology”. In: *Electron. Lett.* 53.9 (2017), pages 609–611. DOI: `10.1049/el.2017.0140`.

[Bon+02] M. Bona, L. Manholm, J. P. Starski, and B. Svensson. “Low-loss compact Butler matrix for a microstrip antenna”. In: *IEEE Transactions on Microwave Theory and Techniques* 50.9 (Sept. 2002), pages 2069–2075. DOI: `10.1109/TMTT.2002.802318`.

[Bon+17] F. Bongard, M. Gimersky, S. Doherty, X. Aubry, and M. Krummen. "3D-printed Ka-band waveguide array antenna for mobile SATCOM applications". In: *2017 11th European Conference on Antennas and Propagation (EUCAP)*. Mar. 2017, pages 579–583. DOI: `10.23919/EuCAP.2017.7928705`.

[Bun16] Bundesnetzagentur. *Frequenzplan*. 2016. URL: `https://www.bundesnetzagentur.de`.

[But+61] J. Butler and R. Lowe. "Beam-Forming Matrix Simplifies Design of Electronically Scanned Antennas". In: *Electronic Design* 9 (Apr. 1961), pages 170–173.

[Cha+07] S. F. Chao, H. Wang, C. Y. Su, and J. G. J. Chern. "A 50 to 94-GHz CMOS SPDT Switch Using Traveling-Wave Concept". In: *IEEE Microwave and Wireless Components Letters* 17.2 (Feb. 2007), pages 130–132. DOI: `10.1109/LMWC.2006.890339`.

[Cha+08] C. C. Chang, T. Y. Chin, J. C. Wu, and S. F. Chang. "Novel Design of a 2.5-GHz Fully Integrated CMOS Butler Matrix for Smart-Antenna Systems". In: *IEEE Transactions on Microwave Theory and Techniques* 56.8 (Aug. 2008), pages 1757–1763. DOI: `10.1109/TMTT.2008.926528`.

[Cha+10] C. C. Chang, R. H. Lee, and T. Y. Shih. "Design of a Beam Switching/Steering Butler Matrix for Phased Array System". In: *IEEE Transactions on Antennas and Propagation* 58.2 (Feb. 2010), pages 367–374. DOI: `10.1109/TAP.2009.2037693`.

[Cha+13] C.-C. Chang, Y.-C. Chen, and S.-C. Hsieh. "A V-Band Three-State Phase Shifter in CMOS-MEMS Technology". In: *Microwave and Wireless Components Letters, IEEE* 23.5 (2013), pages 264–266. DOI: `10.1109/LMWC.2013.2253309`.

[Che+09] P. Chen, W. Hong, Z. Kuai, J. Xu, H. Wang, J. Chen, H. Tang, J. Zhou, and K. Wu. "A Multibeam Antenna Based on Substrate Integrated Waveguide Technology for MIMO Wireless Communications". In: *IEEE Transactions on Antennas and Propagation* 57.6 (June 2009), pages 1813–1821. DOI: `10.1109/TAP.2009.2019868`.

[Che+10] C. J. Chen and T. H. Chu. "Design of a 60-GHz Substrate Integrated Waveguide Butler Matrix - Systematic Approach". In: *IEEE Transactions on Microwave Theory and Techniques* 58.7 (July 2010), pages 1724–1733. DOI: `10.1109/TMTT.2010.2050097`.

[Che+13] N. Chen, J. Zhen, and Q. Pang. “A millimeter-wave GaAs 5-bit MMIC digital phase shifter”. In: *Microwave and Millimeter Wave Circuits and System Technology (MMWCST), 2013 International Workshop on*. Oct. 2013, pages 444–447. DOI: `10.1109/MMWCST.2013.6814546`.

[Che+16] C. Chen, F. Tuo, X. Xu, and T. Yoshimasu. “A 30-GHz band low-insertion loss and high-isolation SPDT switch IC in 120-nm SiGe HBT”. In: *2016 IEEE International Symposium on Radio-Frequency Integration Technology (RFIT)*. Aug. 2016, pages 1–3. DOI: `10.1109/RFIT.2016.7578134`.

[Col+97] P. J. Collings and M. Hird. *Introduction to Liquid Crystals: Chemistry and Physics*. CRC Press, 1997.

[Coo+65] J. W. Cooley and J. W. Tukey. “An Algorithm for the Machine Calculation of Complex Fourier Series”. In: *Math. Comput.* 19.90 (1965), pages 297–301.

[Den+11] X. Deng, Z. He, S. Yuan, Z. Shao, and L. Liu. “W-band high bit passive phase shifter for automotive radar applications in BiCMOS”. In: *International Conference on Computational Problem-Solving (ICCP)*. Oct. 2011, pages 115–119. DOI: `10.1109/ICCPS.2011.6092220`.

[Dje+09] T. Djerafi and K. Wu. “60 GHz substrate integrated waveguide crossover structure”. In: *2009 European Microwave Conference (EuMC)*. Sept. 2009, pages 1014–1017.

[DuP] DuPont. *DuPont™ GreenTape™ low temperature co-fired ceramic system - Design and Layout Guidelines*. Technical report. URL: `http://www.dupont.com/content/dam/dupont/products-and-services/electronic-and-electrical-materials/documents/prodlib/GreenTape_Design_Layout_Guidelines.pdf`.

[Fan+96] L. Fan and K. Chang. “Uniplanar power dividers using coupled CPW and asymmetrical CPS for MICs and MMICs”. In: *IEEE Transactions on Microwave Theory and Techniques* 44.12 (Dec. 1996), pages 2411–2420. DOI: `10.1109/22.554570`.

[Fen+16] W. Feng, T. Zhang, and W. Che. “Compact single-band planar crossover based on coupled lines”. In: *2016 46th European Microwave Conference (EuMC)*. Oct. 2016, pages 975–978. DOI: `10.1109/EuMC.2016.7824508`.

[Fox47] A. G. Fox. “An Adjustable Wave-Guide Phase Changer”. In: *Proc. IRE* 35.12 (Dec. 1947), pages 1489–1498. DOI: `10.1109/JRPROC.1947.234574`.

[Fra+13] A.-L. Franc, O.H. Karabey, G. Rehder, E. Pistono, R. Jakoby, and P. Ferrari. “Compact and Broadband Millimeter-Wave Electrically Tunable Phase Shifter Combining Slow-Wave Effect With Liquid Crystal Technology”. In: *Microwave Theory and Techniques, IEEE Transactions on* 61.11 (2013), pages 3905–3915. DOI: `10.1109/TMTT.2013.2282288`.

[Fra58] F. C. Frank. “I. Liquid crystals. On the theory of liquid crystals”. In: *Discussions of the Faraday Society* 25 (1958), pages 19–28.

[Fri+11] C. Fritzsch, F. Giacomozzi, O. H. Karabey, F. Goelden, A. Moessinger, S. Bildik, S. Colpo, and R. Jakoby. “Continuously tunable W-band phase shifter based on liquid crystals and MEMS technology”. In: *Microwave Conference (EuMC), 2011 41st European*. Oct. 2011, pages 1083–1086.

[Fri+17] C. Fritzsch and M. Wittek. “Recent developments in liquid crystals for microwave applications”. In: *2017 IEEE International Symposium on Antennas and Propagation USNC/URSI National Radio Science Meeting*. July 2017, pages 1217–1218. DOI: `10.1109/APUSNCURSINRSM.2017.8072651`.

[Fri+97] G. L. Friedsam and E. M. Biebl. “Precision free-space measurements of complex permittivity of polymers in the W-band”. In: *Microwave Symposium Digest, 1997., IEEE MTT-S International*. Volume 3. June 1997, pages 1351–1354. DOI: `10.1109/MWSYM.1997.596579`.

[Gae+09] A. Gaebler, F. Goelden, A. Manabe, M. Goebel, S. Mueller, and R. Jakoby. “Investigation of high performance transmission line phase shifters based on liquid crystal”. In: *Microwave Conference, 2009. EuMC 2009. European*. 2009, pages 594–597.

[Gae15] A. Gaebler. “Synthese steuerbarer Hochfrequenzschaltungen und Analyse Flüssigkristall-basierter Leitungsphasenschieber in Gruppenantennen für Satellitenanwendungen im Ka-Band”. PhD thesis. Darmstadt: Technische Universität, 2015.

[Gen+95] P. G. de Gennes and J. Prost. *The Physics of Liquid Crystals*. Clarendon Press, 1995.

[Gun+12] A. B. Guntupalli, T. Djerafi, and K. Wu. “Ultra-compact millimeter-wave substrate integrated waveguide crossover structure utilizing simultaneous electric and magnetic coupling”. In: *2012 IEEE/MTT-S International Microwave Symposium Digest*. June 2012, pages 1–3. DOI: `10.1109/MWSYM.2012.6259540`.

[Guo+15] D. Guo, T. Qiao, Xi. Luo, and M. Li. “Design of a Ka-band broadband SPDT switch MMIC based on GaN HEMTs”. In: *2015 IEEE 16th International Conference on Communication Technology (ICCT)*. Oct. 2015, pages 241–243. DOI: `10.1109/ICCT.2015.7399832`.

[Gö09] F. Gölden. “Liquid Crystal Based Microwave Components with Fast Response Times: Material, Technology, Power Handling Capability”. PhD thesis. Technische Universität Darmstadt, Fachgebiet Mikrowellentechnik, June 2009.

[Han66] R. C. Hansen. *Microwave Scanning Antennas: Array systems*. Academic Press, 1966.

[Her17] Heraeus. *Properties of Fused Silica*. Dec. 18, 2017. URL: `https://www.heraeus.com/en/hqs/fused_silica_quartz_knowledge_base/properties/properties.aspx`.

[Hil00] L. T. Hildebrand. “Results for a simple compact narrow-wall directional coupler”. In: *IEEE Microwave and Guided Wave Letters* 10.6 (June 2000), pages 231–232. DOI: `10.1109/75.852425`.

[Hir+96] T.M. Hirvonen, P. Vainikainen, Andrzej Lozowski, and A.V. Raisanen. “Measurement of dielectrics at 100 GHz with an open resonator connected to a network analyzer”. In: *Instrumentation and Measurement, IEEE Transactions on* 45.4 (Aug. 1996), pages 780–786. DOI: `10.1109/19.516996`.

[Hof+03] A. Hofmann, E. Horster, J. Weinzierl, L. P. Schmidt, and H. Brand. “Flexible Low-Loss Dielectric Waveguides for THz Frequencies with Transitions to Metal Waveguides”. In: *2003 33rd European Microwave Conference*. Oct. 2003, pages 955–958. DOI: `10.1109/EUMA.2003.341121`.

[Hon+10] D. Hondros and P. Debye. “Elektromagnetische Wellen an dielektrischen Drähten”. In: *Ann. Phys.* 337.8 (1910), pages 465–476. DOI: `10.1002/andp.19103370802`.

[Hor89] W. E. Hord. “Microwave and millimeter-wave ferrite phase shifters”. In: *Microwave Journal* 32 (1989), pages 81–89.

[Inc17a] C-Lec Plastics Inc. *Rexolite data sheet*. July 16, 2017. URL: `http://www.rexolite.com/specifications/`.

[Inc17b] Pasternack Enterprises Inc. *WR-10 PIN Diode SPDT Waveguide Switch (Data sheet - PE71S9004)*. May 20, 2017. URL: `https://www.pasternack.com/images/ProductPDF/PE71S9004.pdf`.

[Inc17c] SAGE Millimeter Inc. *90 to 100 GHz PIN Diode Switch*. May 20, 2017. URL: `http://www.sagemillimeter.com/_p/prd3/4468418341/product/90-to-100-ghz-spdt-pin-diode-switch`.

[Ind17] Evonik Industries. *Rohacell HF Datasheet*. Dec. 18, 2017. URL: `http://www.rohacell.com/sites/lists/RE/DocumentsHP/ROHACELL%20HF%20Product%20Information.pdf`.

[Isk+16] Z. Iskandar, J. Lugo-Alvarez, A. Bautista, E. Pistono, F. Podevin, V. Puyal, A. Siligaris, and P. Ferrari. "A 30–50 GHz reflection-type phase shifter based on slow-wave coupled lines in BiCMOS 55 nm technology". In: *European Microwave Conference (EuMC)*. Oct. 2016, pages 1413–1416. DOI: `10.1109/EuMC.2016.7824618`.

[Kam+14] P. Kaminski, K. Wincza, and S. Gruszczynski. "Switched-beam antenna array with broadside beam fed by modified butler matrix for radar receiver application". In: *Microwave and Optical Technology Letters* 56.3 (2014), pages 732–735. DOI: `10.1002/mop.28131`.

[Kan+09] D.-W. Kang, J.-G. Kim, B.-W. Min, and G. M. Rebeiz. "Single and Four-Element Ka -Band Transmit/Receive Phased-Array Silicon RFICs With 5-bit Amplitude and Phase Control". In: *Microwave Theory and Techniques, IEEE Transactions on* 57.12 (Dec. 2009), pages 3534–3543. DOI: `10.1109/TMTT.2009.2033302`.

[Kar14] O. H. Karabey. "Electronic beam steering and polarization agile planar antennas in liquid crystal technology". Zugl. Darmstadt, Techn. Univ., Diss., 2013. PhD thesis. Cham: TU Darmstadt, 2014. ISBN: 978-3-319-01423-4.

[Kim+02] H.-T. Kim, J.-H. Park, S. Lee, S. Kim, J.-M. Kim, Y.-K. Kim, and Y. Kwon. "V-band 2-b and 4-b low-loss and low-voltage distributed MEMS digital phase shifter using metal-air-metal capacitors". In: *Microwave Theory and Techniques, IEEE Transactions on* 50.12 (Dec. 2002), pages 2918–2923. DOI: `10.1109/TMTT.2002.805285`.

[Kin+57] D. D. King and S. P. Schlesinger. "Losses in Dielectric Image Lines". In: *IRE Transactions on Microwave Theory and Techniques* 5.1 (Jan. 1957), pages 31–35. DOI: `10.1109/TMTT.1957.1125087`.

[Kin+58] D. D. King and S. P. Schlesinger. "Dielectric Image Lines". In: *IRE Transactions on Microwave Theory and Techniques* 6.3 (July 1958), pages 291–299. DOI: `10.1109/TMTT.1958.1124560`.

[Kle+11] T. Klein, C. Günner, J. Kassner, R. Kulke, and H. Wolf. "Multiple Feed per Beam networks for Ka-band satellite communication systems in LTCC technology". In: *Microwave Symposium Digest (MTT), 2011 IEEE MTT-S International*. June 2011, pages 1–4. DOI: `10.1109/MWSYM.2011.5972590`.

[Kne+08] F. K. Kneubühl and M. W. Sigrist. *Laser*. Vieweg+Teubner Verlag, 2008.

[Kob+82] S. Kobayashi, R. Mittra, and R. Lampe. "Dielectric tapered rod antennas for millimeter-wave applications". In: *IEEE Transactions on Antennas and Propagation* 30.1 (Jan. 1982), pages 54–58. DOI: `10.1109/TAP.1982.1142758`.

[Kou+05] M. Koubeissi, C. Decroze, T. Monediere, and B. Jecko. "Switched-beam antenna based on novel design of Butler matrices with broadside beam". In: *Electronics Letters* 41.20 (Sept. 2005), pages 1097–1098. DOI: `10.1049/el:20052676`.

[Kou91] B. B. S. K. Koul. *Microwave and Millimeter Wave Phase Shifters: Dielectric and ferrite phase shifters*. Artech House, 1991.

[Koz+01] A. B. Kozyrev, A. V. Ivanov, O. I. Soldatenkov, A. V. Tumarkin, S. V. Razumov, and S. Yu. Aigunova. "Ferroelectric (Ba,Sr)TiO3 thin-film 60-GHz phase shifter". In: *Tech. Phys. Lett.* 27.12 (2001), pages 1032–1034. DOI: `10.1134/1.1432340`.

[Kuk+02] T. Kuki, H. Fujikake, and T. Nomoto. "Microwave variable delay line using dual-frequency switching-mode liquid crystal". In: *IEEE Transactions on Microwave Theory and Techniques* 50.11 (Nov. 2002), pages 2604–2609. DOI: `10.1109/TMTT.2002.804510`.

[Kum+12] G. A. Kumar and A. Kumar. "Low loss and high isolation Ka-band SPDT switch". In: *2012 5th International Conference on Computers and Devices for Communication (CODEC)*. Dec. 2012, pages 1–3. DOI: `10.1109/CODEC.2012.6509280`.

[Kum00] S. Kumar. *Liquid Crystals: Experimental Study of Physical Properties and Phase Transition*. Cambridge University Press, 2000.

[Kuz85] M. Kuznetsov. "Radiation loss in dielectric waveguide Y-branch structures". In: *Journal of Lightwave Technology* 3.3 (June 1985), pages 674–677. DOI: `10.1109/JLT.1985.1074216`.

[Lam+08] A. E. I. Lamminen, J. Saily, and A. R. Vimpari. "60-GHz Patch Antennas and Arrays on LTCC With Embedded-Cavity Substrates". In: *IEEE Transactions on Antennas and Propagation* 56.9 (Sept. 2008), pages 2865–2874. DOI: `10.1109/TAP.2008.927560`.

[Lam96] J. W. Lamb. “Miscellaneous data on materials for millimetre and submillimetre optics”. In: *Int. J. Infrared Millimeter Waves* 17.12 (Dec. 1996), pages 1997–2034. DOI: `10.1007/BF02069487`.

[Leh89] O. Lehmann. “Über fliessende Krystalle”. In: *Zeitschrift für physikalische Chemie* 4.1 (1889), pages 462–472.

[Lei+05] S. Lei, Y. X. Guo, and L. C. Ong. “CPW to stripline transitions in LTCC for millimeter-wave applications”. In: *2005 Asia-Pacific Microwave Conference Proceedings*. Volume 2. Dec. 2005. DOI: `10.1109/APMC.2005.1606430`.

[Liu+05] A.-S. Liu, C. K. C. Tzuang, R.-B. Wu, and H.-S. Wu. “Ka-band 32-GHz planar integrated switched-beam smart antenna”. In: *IEEE MTT-S International Microwave Symposium Digest, 2005.* June 2005. DOI: `10.1109/MWSYM.2005.1516661`.

[Liu+12] W. Liu, Z. Zhang, Z. Feng, and M. F. Iskander. “A Compact Wideband Microstrip Crossover”. In: *IEEE Microwave and Wireless Components Letters* 22.5 (May 2012), pages 254–256. DOI: `10.1109/LMWC.2012.2190270`.

[Liu+14] C. Liu, Q. Li, and Y. Z. Xiong. “A compact Ka-band SPDT switch with high isolation”. In: *2014 International Symposium on Integrated Circuits (ISIC)*. Dec. 2014, pages 304–307. DOI: `10.1109/ISICIR.2014.7029563`.

[Mal43] P. Mallach. “Dielektrische Richtstrahler für dm-und cm-Wellen”. In: *ZWB Berlin Adlershof* (1943), pages 132–168.

[Mar+14] A. Margomenos, A. Kurdoghlian, M. Micovic, K. Shinohara, H. Moyer, D. C. Regan, R. M. Grabar, C. McGuire, M. D. Wetzel, and D. H. Chow. “W-Band GaN Receiver Components Utilizing Highly Scaled, Next Generation GaN Device Technology”. In: *2014 IEEE Compound Semiconductor Integrated Circuit Symposium (CSICS)*. Oct. 2014, pages 1–4. DOI: `10.1109/CSICS.2014.6978585`.

[Mar69] E. A. J. Marcatili. “Dielectric rectangular waveguide and directional coupler for integrated optics”. In: *The Bell System Technical Journal* 48.7 (Sept. 1969), pages 2071–2102. DOI: `10.1002/j.1538-7305.1969.tb01166.x`.

[May+10] J. W. May and G. M. Rebeiz. “Design and Characterization of W-Band SiGe RFICs for Passive Millimeter-Wave Imaging”. In: *IEEE Transactions on Microwave Theory and Techniques* 58.5 (May 2010), pages 1420–1430. DOI: `10.1109/TMTT.2010.2042857`.

[Min+08] B. W. Min and G. M. Rebeiz. “Ka -Band Low-Loss and High-Isolation Switch Design in 0.13-um CMOS”. In: *IEEE Transactions on Microwave Theory and Techniques* 56.6 (June 2008), pages 1364–1371. DOI: `10.1109/TMTT.2008.921749`.

[Mue+05] S. Mueller, C. Felber, P. Scheele, M. Wittek, C. Hock, and R. Jakoby. “Passive tunable liquid crystal finline phase shifter for millimeter waves”. In: *Microwave Conference, 2005 European*. Volume 1. Oct. 2005. DOI: `10.1109/EUMC.2005.1608852`.

[Mue+06] S. Mueller, F. Goelden, P. Scheele, M. Wittek, C. Hock, and R. Jakoby. “Passive Phase Shifter for W-Band Applications using Liquid Crystals”. In: *2006 European Microwave Conference*. Sept. 2006, pages 306–309. DOI: `10.1109/EUMC.2006.281317`.

[Mue07] S. Mueller. “Grundlegende Untersuchungen steuerbarer passiver Flüssigkristall-Komponenten für die Mikrowellentechnik”. PhD thesis. Technische Universität Darmstadt, 2007.

[Nai+13] D. M. Nair, W. E. McKinzie, B. A. Thrasher, M. A. Smith, E. D. Hughes, and J. M. Parisi. “A 10 MHz to 100 GHz LTCC CPW-to-stripline vertical transition”. In: *2013 IEEE MTT-S International Microwave Symposium Digest (MTT)*. June 2013, pages 1–4. DOI: `10.1109/MWSYM.2013.6697612`.

[Nes68] W. Nester. “The fast Fourier transform and the Butler matrix”. In: *IEEE Transactions on Antennas and Propagation* 16.3 (May 1968), pages 360–360. DOI: `10.1109/TAP.1968.1139175`.

[New05] R. E. Newnham. *Properties of Materials: Anisotropy, Symmetry, Structure*. Oxford University Press, 2005.

[Nik+14] M. Nikfalazar, C. Kohler, A. Friederich, M. Sazegar, Yuliang Zheng, A. Wiens, J.R. Binder, and R. Jakoby. “Fully printed tunable phase shifter for L/S-band phased array application”. In: *Microwave Symposium (IMS), 2014 IEEE MTT-S International*. June 2014, pages 1–4. DOI: `10.1109/MWSYM.2014.6848295`.

[Ogu85] K. Ogusu. “Experimental Study of Dielectric Waveguide Y-Junctions for Millimeter-Wave Integrated Circuits”. In: *IEEE Transactions on Microwave Theory and Techniques* 33.6 (June 1985), pages 506–509. DOI: `10.1109/TMTT.1985.1133106`.

[Ozt+14] E. Ozturk, M. H. Nemati, M. Kaynak, B. Tillack, and I. Tekin. "SiGe process integrated full-360° microelectromechanical systems-based active phase shifter for W-band automotive radar". In: *IET Microwaves, Antennas Propagation* 8.11 (Aug. 2014), pages 835–841. DOI: `10.1049/iet-map.2013.0594`.

[Pao+14] R. De Paolis, F. Coccetti, S. Payan, M. Maglione, and G. Guegan. "Characterization of ferroelectric BST MIM capacitors up to 65 GHz for a compact phase shifter at 60 GHz". In: *European Microwave Conference (EuMC*. Oct. 2014, pages 492–495. DOI: `10.1109/EuMC.2014.6986478`.

[Pei+04] M. Peichl, S. Dill, M. Jirousek, and H. Suess. "Microwave Radiometry - Imaging Technologies and Applications". In: *Proceedings of WFMN07*. Chemnitz, Germany, 2004.

[Pen+04] A. Penirschke, S. Mueller, P. Scheele, C. Weil, M. Wittek, C. Hock, and R. Jakoby. "Cavity perturbation method for characterization of liquid crystals up to 35 GHz". In: *Microwave Conference, 2004. 34th European*. Volume 2. Oct. 2004, pages 545–548.

[Pio+93] B. Piovano, L. Accatino, A. Angelucci, T. Jones, P. Capece, and M. Votta. "Design And Breadboarding Of Wideband Nxn Butler Matrices For Multiport Amplifiers". In: *Microwave Conference/Brazil, 1993., SBMO International*. Volume 1. Aug. 1993, pages 175–180. DOI: `10.1109/SBMO.1993.589533`.

[Poh+12] C. H. J. Poh, R. L. Schmid, J. D. Cressler, and J. Papapolymerou. "An X-band to Ka-band SPDT switch using 200 nm SiGe HBTs". In: *2012 IEEE 12th Topical Meeting on Silicon Monolithic Integrated Circuits in RF Systems*. Jan. 2012, pages 183–186. DOI: `10.1109/SiRF.2012.6160118`.

[Pra+17] A. E. Prasetiadi, M. Jost, B. Schulz, M. Quibeldey, T. Rabe, R. Follmann, and R. Jakoby. "Liquid-crystal-based amplitude tuner fabricated in LTCC technology". In: *2017 47th European Microwave Conference (EuMC)*. Oct. 2017, pages 1085–1088. DOI: `10.23919/EuMC.2017.8231035`.

[Psy+13] D. Psychogiou, Y. Li, J. Hesselbarth, S. Kuehne, D. Peroulis, C. Hierold, and C. Hafner. "Millimeter-wave phase shifter based on waveguide-mounted RF-MEMS". In: *Microwave Opt. Technol. Lett.* 55.3 (2013), pages 465–468. DOI: `10.1002/mop.27390`.

[R16] International Telecommunication Union R, editor. *Rec. ITU-R P.676-11 - Attenuation by atmospheric gases*. Sept. 30, 2016. URL: `https://www.itu.int/dms_pubrec/itu-r/rec/p/R-REC-P.676-11-201609-I!!PDF-S.pdf`.

[RC+07] J. A. Ruiz-Cruz, J. R. Montejo-Garai, J. M. Rebollar, A. I. Daganzo, and I. Hidalgo-Carpintero. "Design of Riblet-type couplers for Ka band applications". In: *2007 IEEE Antennas and Propagation Society International Symposium*. June 2007, pages 4276–4279. DOI: `10.1109/APS.2007.4396486`.

[Ree+17a] R. Reese, M. Jost, M. Nickel, E. Polat, R. Jakoby, and H. Maune. "A Fully Dielectric Lightweight Antenna Array Using a Multimode Interference Power Divider at W-Band". In: *IEEE Antennas and Wireless Propagation Letters* 16 (2017), pages 3236–3239. DOI: `10.1109/LAWP.2017.2771385`.

[Ree+17b] R. Reese, E. Polat, M. Jost, M. Nickel, R. Jakoby, and H. Maune. "Liquid crystal based phase shifter in a parallel-plate dielectric waveguide topology at V-band". In: *European Microwave Conference (EuMC)*. Oct. 2017, pages 353–356. DOI: `10.23919/EuMIC.2017.8230731`.

[Reg+57] F. Reggia and E.G. Spencer. "A New Technique in Ferrite Phase Shifting for Beam Scanning of Microwave Antennas". In: *Proc. IRE* 45.11 (Nov. 1957), pages 1510–1517. DOI: `10.1109/JRPROC.1957.278344`.

[Rei05] G. A. Reider. *Photonik - Eine Einführung in die Grundlagen*. Springer Vienna, 2005.

[Rei88] F. Reinitzer. "Beiträge zur Kenntniss des Cholesterins". German. In: *Monatshefte für Chemie und verwandte Teile anderer Wissenschaften* 9.1 (1888), pages 421–441. DOI: `10.1007/BF01516710`.

[Rem+06] J. Remez and R. Carmon. "Compact Designs of Waveguide Butler Matrices". In: *IEEE Antennas and Wireless Propagation Letters* 5.1 (Dec. 2006), pages 27–31. DOI: `10.1109/LAWP.2005.863615`.

[Rey+12] S. Reyaz, C. Samuelsson, R. Malmqvist, M. Kaynak, and A. Rydberg. "Millimeter-wave RF-MEMS SPDT switch networks in a SiGe BiCMOS process technology". In: *Microwave Integrated Circuits Conference (EuMIC), 2012 7th European*. Oct. 2012, pages 691–694.

[Rib52] H. J. Riblet. "The Short-Slot Hybrid Junction". In: *Proc. IRE* 40.2 (Feb. 1952), pages 180–184. DOI: `10.1109/JRPROC.1952.274021`.

[Riv+14] C. Riva, C. Capsoni, L. Luini, M. Luccini, R. Nebuloni, and A. Martellucci. “The challenge of using the W band in satellite communication”. In: *Int. J. Satell. Commun. Networking* 32.3 (2014), pages 187–200. DOI: `10.1002/sat.1050`.

[Saz+11a] M. Sazegar, Y. Zheng, H. Maune, C. Damm, X. Zhou, and R. Jakoby. “Compact Tunable Phase Shifters on Screen-Printed BST for Balanced Phased Arrays”. In: *IEEE Transactions on Microwave Theory and Techniques* 59.12 (Dec. 2011), pages 3331–3337. DOI: `10.1109/TMTT.2011.2171985`.

[Saz+11b] M. Sazegar, Yuliang Zheng, H. Maune, C. Damm, Xianghui Zhou, J. Binder, and R. Jakoby. “Low-Cost Phased-Array Antenna Using Compact Tunable Phase Shifters Based on Ferroelectric Ceramics”. In: *Microwave Theory and Techniques, IEEE Transactions on* 59.5 (May 2011), pages 1265–1273. DOI: `10.1109/TMTT.2010.2103092`.

[Sca+02] M. C. Scardelletti, G. E. Ponchak, and N. C. Varaljay. “MEMS, Ka-band single-pole double-throw (SPDT) switch for switched line phase shifters”. In: *IEEE Antennas and Propagation Society International Symposium (IEEE Cat. No.02CH37313)*. Volume 2. 2002, pages 2–5. DOI: `10.1109/APS.2002.1016014`.

[Sch+10] M. Schneider, C. Hartwanger, E. Sommer, and H. Wolf. “Test results for the multiple spot beam antenna project 'Medusa'”. In: *Proceedings of the Fourth European Conference on Antennas and Propagation*. Apr. 2010, pages 1–4.

[Sch+11] M. Schneider, C. Hartwanger, and H. Wolf. “Antennas for multiple spot beam satellites”. English. In: *CEAS Space Journal* 2.1-4 (2011), pages 59–66. DOI: `10.1007/s12567-011-0012-z`.

[Sch+14] R. L. Schmid, P. Song, C. T. Coen, A. C. Ulusoy, and J. D. Cressler. “On the Analysis and Design of Low-Loss Single-Pole Double-Throw W-Band Switches Utilizing Saturated SiGe HBTs”. In: *IEEE Transactions on Microwave Theory and Techniques* 62.11 (Nov. 2014), pages 2755–2767. DOI: `10.1109/TMTT.2014.2354017`.

[Sch+98] H.W. Schuessler and P. Steffen. “Halfband filters and Hilbert transformers”. English. In: *Circuits, Systems and Signal Processing* 17.2 (1998), pages 137–164. DOI: `10.1007/BF01202851`.

[She+17] J. Shen, M. W. Aiken, M. Abbasi, D. P. Parekh, X. Zhao, M. D. Dickey, and D. S. Ricketts. “Rapid prototyping of low loss 3D printed waveguides for millimeter-wave applications”. In: *2017 IEEE MTT-S International Microwave Symposium (IMS)*. June 2017, pages 41–44. DOI: `10.1109/MWSYM.2017.8058593`.

[She68] J. P. Shelton. “Fast Fourier transforms and Butler matrices”. In: *Proceedings of the IEEE* 56.3 (Mar. 1968), pages 350–350. DOI: `10.1109/PROC.1968.6302`.

[Shi+07] S. E. Shih, D. W. Duan, O. Fordham, M. Parmar, K. Tornquist, X. Zeng, P. Chang-Chien, and R. Tsai. “A W-Band 4-Bit Phase Shifter in Multilayer Scalable Array Systems”. In: *2007 IEEE Compound Semiconductor Integrated Circuits Symposium*. Oct. 2007, pages 1–4. DOI: `10.1109/CSICS07.2007.20`.

[Sol+95] L. B. Soldano and E. C. M. Pennings. “Optical multi-mode interference devices based on self-imaging: principles and applications”. In: *Journal of Lightwave Technology* 13.4 (Apr. 1995), pages 615–627. DOI: `10.1109/50.372474`.

[Som+12] N. Somjit, G. Stemme, and J. Oberhammer. “Performance optimization of multi-stage MEMS W-band dielectric-block phase-shifters”. In: *Microwave Integrated Circuits Conference (EuMIC), 2012 7th European*. Oct. 2012, pages 433–436.

[Som99] A. Sommerfeld. “Ueber die Fortpflanzung elektrodynamischer Wellen längs eines Drahtes”. In: *Ann. Phys.* 303.2 (1899), pages 233–290. DOI: `10.1002/andp.18993030202`.

[Spo+17] M. Sporer, R. Weigel, and A. Koelpin. “A 24 GHz Dual-Polarized and Robust Dielectric Rod Antenna”. In: *IEEE Transactions on Antennas and Propagation* 65.12 (Dec. 2017), pages 6952–6959. DOI: `10.1109/tap.2017.2764530`.

[Sta57] L. Stark. “A helical line scanner for beam steering a linear array”. In: *Antennas and Propagation, IRE Transactions on* 5.2 (Apr. 1957), pages 211–216. DOI: `10.1109/TAP.1957.1144490`.

[Ste+08] A. Stehle, G. Georgiev, V. Ziegler, B. Schoenlinner, U. Prechtel, H. Seidel, and U. Schmid. “RF-MEMS Switch and Phase Shifter Optimized for W-Band”. In: *Microwave Conference, 2008. EuMC 2008. 38th European*. Oct. 2008, pages 104–107. DOI: `10.1109/EUMC.2008.4751398`.

[Ste04] I. W. Stewart. *The Static and Dynamic Continuum Theory of Liquid Crystals: A Mathematical Introduction*. Taylor & Francis, 2004.

[Str+14] S. Strunck, A. Gaebler, O. H. Karabey, A. Heunisch, B. Schulz, T. Rabe, R. Follmann, J. Kassner, D. Koether, A. Manabe, and R. Jakoby. “Reliability study of a tunable Ka-band SIW-phase shifter based on liquid crystal in LTCC-technology”. In: *Int. J. Microwave Wireless Technolog.* FirstView (July 2014), pages 1–7. DOI: `10.1017/S175907871400083X`.

[Str15] S. Strunck. “Flüssigkristall-basierte und LTCC-integrierte elektrisch steuerbare Mikrowellenphasenschieber und -polarisatoren”. Zugl.: Darmstadt, Techn. Univ., Diss. 2015. PhD thesis. Aachen: TU Darmstadt, 2015. ISBN: 978-3-8440-3453-0.

[Tal+15] A. Talai, F. Steinhäußer, A. Bittner, U. Schmid, R. Weigel, and A. Koelpin. “A method for the determination of the complex permittivity by detuned ring resonators for bulk materials up to 110 GHz”. In: *Int. J. Microwave Wireless Technolog.* 7.3-4 (2015), pages 251–260. DOI: `10.1017/S1759078715000483`.

[Tom+10] A. Tomkins, P. Garcia, and S. P. Voinigescu. “A Passive W-Band Imaging Receiver in 65-nm Bulk CMOS”. In: *IEEE Journal of Solid-State Circuits* 45.10 (Oct. 2010), pages 1981–1991.

[Ulu+15] A. C. Ulusoy, R. L. Schmid, M. Kaynak, B. Tillack, and J. D. Cressler. “High-performance W-band LNA and SPDT switch in 0.13 µm SiGe HBT technology”. In: *Radio and Wireless Symposium (RWS), 2015 IEEE*. Jan. 2015, pages 162–164. DOI: `10.1109/RWS.2015.7129716`.

[Vel+07] G. Velu, K. Blary, L. Burgnies, A. Marteau, G. Houzet, D. Lippens, and J.-C. Carru. “A 360° BST Phase Shifter With Moderate Bias Voltage at 30 GHz”. In: *Microwave Theory and Techniques, IEEE Transactions on* 55.2 (Feb. 2007), pages 438–444. DOI: `10.1109/TMTT.2006.889319`.

[Vor+82] J. L. Vorhaus, R. A. Pucel, and Y. Tajima. “Monolithic Dual-Gate GaAs FET Digital Phase Shifter”. In: *IEEE Transactions on Microwave Theory and Techniques* 30.7 (July 1982), pages 982–992. DOI: `10.1109/TMTT.1982.1131187`.

[Wan+07] C. W. Wang, T. G. Ma, and C. F. Yang. “A New Planar Artificial Transmission Line and Its Applications to a Miniaturized Butler Matrix”. In: *IEEE Transactions on Microwave Theory and Techniques* 55.12 (Dec. 2007), pages 2792–2801. DOI: `10.1109/TMTT.2007.909474`.

[Wei+03] C. Weil, S. Muller, P. Scheele, P. Best, G. Lussem, and R. Jakoby. “Highly-anisotropic liquid-crystal mixtures for tunable microwave devices”. In: *Electronics Letters* 39.24 (Nov. 2003), pages 1732–1734. DOI: `10.1049/el:20031150`.

[Wei+13a] C. Weickhmann, N. Nathrath, R. Gehring, A. Gaebler, M. Jost, and R. Jakoby. “A light-weight tunable liquid crystal phase shifter for an efficient phased array antenna”. In: *Microwave Conference (EuMC), 2013 European*. 2013, pages 428–431.

[Wei+13b] C. Weickhmann, N. Nathrath, R. Genning, A. Gaebler, M. Jost, and R. Jakoby. “Recent measurements of compact electronically tunable liquid crystal phase shifter in rectangular waveguide topology”. In: *Electron. Lett.* 49.21 (2013), pages 1345–1347. DOI: `10.1049/el.2013.2281`.

[Wei17] C. Weickhmann. “Liquid Crystals Towards Terahertz: Characterisation and Tunable Waveguide Phase Shifters for Millimetre-Wave and Terahertz Beamsteering Antennas”. PhD thesis. Darmstadt: Technische Universität Darmstadt, May 2017.

[Whi65] J. F. White. “High Power, p-i-n Diode Controlled, Microwave Transmission Phase Shifters”. In: *Microwave Theory and Techniques, IEEE Transactions on* 13.2 (Mar. 1965), pages 233–242. DOI: `10.1109/TMTT.1965.1125968`.

[Whi68] J. F. White. “Review of semiconductor microwave phase shifters”. In: *Proceedings of the IEEE* 56.11 (Nov. 1968), pages 1924–1931. DOI: `10.1109/PROC.1968.6767`.

[Win+05] K. Wincza and S. Gruszczynski. “A broadband 4x4 Butler matrix for modern-day antennas”. In: *2005 European Microwave Conference*. Volume 2. Oct. 2005. DOI: `10.1109/EUMC.2005.1610181`.

[Win+06] K. Wincza, S. Gruszczynski, and K. Sachse. “Reduced sidelobe four-beam antenna array fed by modified Butler matrix”. In: *Electron. Lett.* 42.9 (Apr. 2006), pages 508–509. DOI: `10.1049/el:20060313`.

[Win+15] K. Wincza, A. Rydosz, I. Slomian, and S. Gruszczynski. “Reduced sidelobe multibeam antenna array with broadside beam fed by 4x8 Butler matrix”. In: *International Symposium on Antennas and Propagation*. Nov. 2015, pages 1–3.

[Yan+06] D.-K. Yang and S.-T. Wu. *Fundamentals of Liquid Crystal Devices*. John Wiley & Sons Ltd, 2006.

[Yan+11] J. G. Yang and K. Yang. “Ka-Band 5-Bit MMIC Phase Shifter Using InGaAs PIN Switching Diodes”. In: *IEEE Microwave and Wireless Components Letters* 21.3 (Mar. 2011), pages 151–153. DOI: `10.1109/LMWC.2010.2104314`.

[Ye+15] X. F. Ye, S. Y. Zheng, and J. H. Deng. “A compact patch crossover for millimeter-wave applications”. In: *2015 International Workshop on Electromagnetics: Applications and Student Innovation Competition (iWEM)*. Nov. 2015, pages 1–2. DOI: `10.1109/iWEM.2015.7365054`.

[Yeh+08] C. Yeh and F. Shimabukuro. *The Essence of Dielectric Waveguides*. Springer US, 2008.

[Zah+15] A. H. Zahr, P. Blondy, L. Y. Zhang, C. Dorion, R. Stéfanini, F. Courtade, and F. Pressecq. “A DC-30 GHz high performance packaged RF MEMS SPDT switch”. In: *2015 European Microwave Conference (EuMC)*. Sept. 2015, pages 1015–1017. DOI: `10.1109/EuMC.2015.7345938`.

[Zah16] H. Zahn. “Über den Nachweis elektromagnetischer Wellen an dielektrischen Drähten”. In: *Ann. Phys.* 354.8 (1916), pages 907–933. DOI: `10.1002/andp.19163540803`.

[Zha+17] B. Zhang, Y. X. Guo, H. Zirath, and Y. P. Zhang. “Investigation on 3-D-Printing Technologies for Millimeter- Wave and Terahertz Applications”. In: *Proceedings of the IEEE* 105.4 (Apr. 2017), pages 723–736. DOI: `10.1109/JPROC.2016.2639520`.

[Zhe+13] X. Zheng, J. C. Tremblay, S. E. Huettner, K. P. Ip, T. Papale, and K. L. Lange. “Ka-Band High Power GaN SPDT Switch MMIC”. In: *2013 IEEE Compound Semiconductor Integrated Circuit Symposium (CSICS)*. Oct. 2013, pages 1–5. DOI: `10.1109/CSICS.2013.6659234`.

[Zhu+04] Lei Zhu and W. Menzel. “Broad-band microstrip-to-CPW transition via frequency-dependent electromagnetic coupling”. In: *IEEE Transactions on Microwave Theory and Techniques* 52.5 (May 2004), pages 1517–1522. DOI: `10.1109/TMTT.2004.827034`.

[Zhu+14] W. Zhu, Y. Shen, and X. Gong. “Ka-band loaded-line phase shifter design on flexible substrate”. In: *Antennas and Propagation Society International Symposium (APSURSI), 2014 IEEE*. July 2014, pages 1688–1689. DOI: `10.1109/APS.2014.6905170`.

Contributions

First author

Journal

[Jos+13] M. Jost, C. Weickhmann, S. Strunck, A. Gaebler, C. Fritzsch, O.H. Karabey, and R. Jakoby. “Liquid crystal based low-loss phase shifter for W-band frequencies”. In: *Electronics Letters* 49 (Nov. 2013), pages 1460–1462.

[Jos+14c] M. Jost, J. Lingner, M. Letz, and G. Jakob. “Thermoelectric properties of p-type $Bi_2Sr_2Co_2O_9$ glass-ceramics”. In: *Semiconductor Science and Technology* 29.12 (2014), page 124011.

[Jos+15c] M. Jost, A. Gaebler, C. Weickhmann, S. Strunck, W. Hu, O. H. Karabey, and R. Jakoby. “Evolution of Microwave Nematic Liquid Crystal Mixtures and Development of Continuously Tuneable Micro- and Millimetre Wave Components”. In: *Molecular Crystals and Liquid Crystals* 610.1 (2015), pages 173–186.

[Jos+18a] M. Jost, R. Reese, M. Nickel, H. Maune, and R. Jakoby. “Fully Dielectric Interference-Based SPDT With Liquid Crystal Phase Shifters”. In: *IET Microwaves, Antennas & Propagation* 12.6 (May 2018), pages 850–857.

[Jos+18c] M. Jost, J. S. K. Gautam, L. G. Gomes, R. Reese, E. Polat, M. Nickel, J. M. Pinheiro, A. L. C. Serrano, H. Maune, G. P. Rehder, P. Ferrari, and R. Jakoby. “Miniaturized Liquid Crystal Slow-Wave Phase Shifter Based on Nanowire Filled Membranes”. In: *IEEE Microwave and Wireless Components Letters* (accepted) (2018).

Conference

[Jos+14a] M. Jost, C. Weickhmann, S. Strunck, A. Gaebler, W. Hu, T. Franke, A. E. Prasetiadi, O. H. Karabey, and R. Jakoby. “Electrically biased W-band phase shifter based on liquid crystal”. In: *International Conference on Infrared, Millimeter, and Terahertz waves (IRMMW-THz)*. Sept. 2014, pages 1–2.

[Jos+14b] M. Jost, A. Gaebler, C. Weickhmann, S. Strunck, W. Hu, O. H. Karabey, and R. Jakoby. “Evolution of microwave nematic liquid crystal mixtures and development of continuously tunable micro- and millimetre wave components”. In: *25th International Liquid Crystal Conference*. July 2014.

[Jos+15a] M. Jost, C. Weickhmann, and R. Jakoby. “Continuously tuneable, high performance phase shifters based on liquid crystal for applications in phased array Antennas”. In: *DPG-Frühjahrstagung*. 2015.

[Jos+15b] M. Jost, S. Strunck, A. Heunisch, A. Wiens, A. E. Prasetiadi, C. Weickhmann, B. Schulz, M. Quibeldey, O. H. Karabey, T. Rabe, R. Follmann, D. Koether, and R. Jakoby. “Continuously tuneable liquid crystal based stripline phase shifter realised in LTCC technology”. In: *European Microwave Conference (EuMC)*. Sept. 2015, pages 1260–1263.

[Jos+15d] M. Jost, C. Weickhmann, T. Franke, A. E. Prasetiadi, W. Hu, M. Nickel, O. H. Karabey, and R. Jakoby. “Tuneable hollow waveguide devices for space applications based on liquid crystal”. In: *International Microwave and Optoelectronics Conference (IMOC)*. Nov. 2015, pages 1–5.

[Jos+16a] M. Jost, R. Reese, J. Pauls, J. S. K. Gautam, R. Gemble, C. Weickhmann, O. H. Karabey, and R. Jakoby. “Comparison of hollow waveguide and dielectric fibre based SPDT switches for W-band”. In: *German Microwave Conference (GeMiC)*. Mar. 2016, pages 140–143.

[Jos+16c] M. Jost, R. Reese, C. Weickhmann, C. Schuster, O. H. Karabey, H. Maune, and R. Jakoby. “Tunable dielectric delay line phase shifter based on liquid crystal technology for a SPDT in a radiometer calibration scheme at 100 GHz”. In: *IEEE MTT-S International Microwave Symposium (IMS)*. May 2016, pages 1–4.

[Jos+17c] M. Jost, R. Reese, H. Maune, and R. Jakoby. “In-plane hollow waveguide crossover based on dielectric insets for millimeter-wave applications”. In: *IEEE MTT-S International Microwave Symposium (IMS)*. June 2017, pages 188–191.

[Jos+17d] M. Jost, R. Reese, M. Nickel, S. Schmidt, H. Maune, and R. Jakoby. "Interference based W-band single-pole double-throw with tunable liquid crystal based waveguide phase shifters". In: *IEEE MTT-S International Microwave Symposium (IMS)*. 2017, pages 184–187.

[Jos+18b] M. Jost, A. Heunisch, A. E. Prasetiadi, B. Schulz, R. Reese, M. Nickel, E. Polat, M. Quibeldey, H. Maune, T. Rabe, R. Follmann, and R. Jakoby. "Liquid Crystal Based SPDT With Adjustable Power Splitting Ratio in LTCC Technology". In: *European Microwave Conference (accepted)*. Sept. 2018.

Co-author

Journal

[Mau+17c] H. Maune, M. Jost, A. Wiens, C. Weickhmann, R. Reese, M. Nikfalazar, C. Schuster, T. Franke, W. Hu, M. Nickel, D. Kienemund, A. Prasetiadi, and R. Jakoby. "Tunable Microwave Component Technologies for SatCom-Platforms". In: *Frequenz* 71.3-4 (Jan. 2017), pages 129–142.

[Pra+15] A. E. Prasetiadi, O. H. Karabey, C. Weickhmann, T. Franke, W. Hu, M. Jost, M. Nickel, and R. Jakoby. "Continuously tunable substrate integrated waveguide bandpass filter in liquid crystal technology with magnetic biasing". In: *Electronics Letters* 51.20 (2015), pages 1584–1585.

[Ree+16b] R. Reese, M. Jost, and R. Jakoby. "Evaluation of two W-band power dividers in a subwavelength dielectric fibre technology". In: *Electronics Letters* 52.16 (2016), pages 1391–1393.

[Ree+17a] R. Reese, M. Jost, M. Nickel, E. Polat, R. Jakoby, and H. Maune. "A Fully Dielectric Lightweight Antenna Array Using a Multimode Interference Power Divider at W-Band". In: *IEEE Antennas and Wireless Propagation Letters* 16 (Nov. 2017), pages 3236–3239.

[Wei+13b] C. Weickhmann, N. Nathrath, R. Genning, A. Gaebler, M. Jost, and R. Jakoby. "Recent measurements of compact electronically tunable liquid crystal phase shifter in rectangular waveguide topology". In: *Electronics Letters* 49.21 (2013), pages 1345–1347.

[Wie+17] A. Wiens, C. Kohler, M. Hansli, M. Schuessler, M. Jost, H. Maune, J. R. Binder, and R. Jakoby. "CAD-assisted modeling of high dielectric contrast composite materials". In: *Journal of the European Ceramic Society* 37.4 (2017), pages 1487–1494.

Conference

[Hu+14a] W. Hu, O. H. Karabey, A. Gaebler, A. E. Prasetiadi, M. Jost, and R. Jakoby. “Liquid crystal varactor loaded variable phase shifter for integrated, compact, and fast beamsteering antenna systems”. In: *European Microwave Conference (EuMC)*. Oct. 2014, pages 1604–1607.

[Hu+14b] W. Hu, O. H. Karabey, A. E. Prasetiadi, M. Jost, and R. Jakoby. “Temperature controlled artificial coaxial line for microwave characterization of liquid crystal”. In: *German Microwave Conference*. 2014.

[Let+18] M. Letz, Z. Wu, S. Viswanathan, M. Jotz, H. Maune, M. Jost, and V. Sundaram. “50 microns glass as the next-generation RF system-integration substrate: High Q inductances for 2.35 GHz impedance matching in 0.05 mm thin, glass substrates”. In: *IEEE Electronic Components and Technology Conference*. 2018.

[Mau+16] H. Maune, M. Nikfalazar, C. Schuster, T. Franke, W. Hu, M. Nickel, D. Kienemund, A. Prasetiadi, C. Weickhmann, M. Jost, A. Wiens, and R. Jakoby. “Tunable microwave component technologies for SatCom-platforms”. In: *German Microwave Conference (GeMiC)*. Mar. 2016, pages 23–26.

[Mau+17a] H. Maune, C. Weickhmann, M. Jost, R. Reese, M. Nickel, C. Fritzsch, and R. Jakoby. “Liquid crystal technology for reconfigurable satcom applications”. In: *Topical Workshop on Internet of Space (TWIOS)*. Jan. 2017, pages 1–4.

[Mau+17b] H. Maune, M. Jost, R. Reese, and R. Jakoby. “Microwave Liquid Crystal Technology (invited)”. In: *International Conference on Advanced Electromaterials*. 2017.

[Nic+17] M. Nickel, O. H. Karabey, M. Maasch, R. Reese, M. Jost, C. Damm, R. Jakoby, and H. Maune. “Analysis of hybrid-passive-active phased array configurations based on an SNR approximation”. In: *European Conference on Antennas and Propagation (EUCAP)*. Mar. 2017, pages 852–856.

[Nic+18] M. Nickel, M. Müh, E. Polat, R. Reese, M. Jost, R. Jakoby, and H. Maune. “Liquid Crystal Based Tunable Reflection-Type Power Divider”. In: *European Microwave Conference (accepted)*. Sept. 2018.

[Pra+16] A. E. Prasetiadi, S. Rahmawati, C. Weickhmann, M. Nickel, M. Jost, T. Franke, W. Hu, H. Maune, and R. Jakoby. "Electrical biasing scheme for Liquid-Crystal-based tunable Substrate Integrated Waveguide structures". In: *German Microwave Conference (GeMiC)*. Mar. 2016, pages 136–139.

[Pra+17] A. E. Prasetiadi, M. Jost, B. Schulz, M. Quibeldey, T. Rabe, R. Follmann, and R. Jakoby. "Liquid-crystal-based amplitude tuner fabricated in LTCC technology". In: *European Microwave Conference (EuMC)*. Oct. 2017, pages 1085–1088.

[Ree+17b] R. Reese, M. Jost, H. Maune, and R. Jakoby. "Design of a continuously tunable W-band phase shifter in dielectric waveguide topology". In: *IEEE MTT-S International Microwave Symposium (IMS)*. 2017, pages 180–183.

[Ree+17c] R. Reese, E. Polat, M. Jost, M. Nickel, R. Jakoby, and H. Maune. "Liquid crystal based phase shifter in a parallel-plate dielectric waveguide topology at V-band". In: *European Microwave Conference (EuMC)*. Oct. 2017, pages 353–356.

[Ree+18] R. Reese, M. Jost, E. Polat, M. Nickel, R. Jakoby, and H. Maune. "Liquid Crystal Based Multimode Interference Switch for Dielectric Waveguides at W-Band". In: *IEEE MTT-S International Microwave Symposium (IMS)*. 2018.

[Str+14] S. Strunck, A. Gaebler, O. H. Karabey, M. Jost, and R. Jakoby. "Electrically reconfigurable waveguide polarizer using liquid crystal technology for Ka-band applications". In: *European Microwave Conference (EuMC)*. Oct. 2014, pages 508–511.

[Wei+13a] C. Weickhmann, N. Nathrath, R. Gehring, A. Gaebler, M. Jost, and R. Jakoby. "A light-weight tunable liquid crystal phase shifter for an efficient phased array antenna". In: *European Microwave Conference (EuMC)*. 2013, pages 428–431.

[Wei+14] C. Weickhmann, M. Jost, D. Laemmle, and R. Jakoby. "Design and fabrication considerations for a 250 GHz liquid crystal phase shifter". In: *International Conference on Infrared, Millimeter, and Terahertz waves (IRMMW-THz)*. Sept. 2014, pages 1–2.

[Wei+15] C. Weickhmann, S. Schmidt, M. Jost, W. Hu, R. Jakoby, A. Manabe, C. Fritzsch, and M. Wittek. "Measuring Liquid Crystal Permittivity With High Accuracy". In: *Condensed Matter and Materials Meeting*. 2015.

Patente

[Jos+17b] M. Jost, R. Reese, H. Maune, and R. Jakoby. “Hohlleiteranordnung für sich kreuzende Hohlleiter zur Übertragung von elektromagnetischen Wellen”. Patent. DE Patent 10 2017 110 150.0. May 2017.

[Let+14] M. Letz, J. Lingner, and M. Jost. “Glaskeramik, thermoelektrisches Bauelement umfassend die Glaskeramik und Verwendung der Glaskeramik”. Patent. DE Patent 102,013,215,662. Dec. 2014.

[Ree+16a] R. Reese, M. Jost, M. Nickel, H. Maune, and R. Jakoby. “Antenneneinrichtung und Verfahren zum Abstrahlen von elektromagnetischen Wellen mit der Antenneneinrichtung”. Patent. DE Patent 10 2016 117 424.6. Sept. 2016.

Workshop

[Jos+16b] M. Jost, C. Weickhmann, O. H. Karabey, H. Maune, and R. Jakoby. “Electronically Liquid Crystal-Based Beamsteering Antennas for SatCom-Applications”. In: *Workshop-Proceedings European Microwave Week*. 2016.

[Jos+17a] M. Jost, R. Jakoby, and H. Maune. “Continuously Tunable Liquid Crystal Devices for Space Applications”. In: *Workshop-Proceeding IEEE MTT-S International Microwave Symposium*. 2017.

[Jos+17e] M. Jost, C. Weickhmann, R. Reese, H. Maune, O. H. Karabey, and R. Jakoby. “Microwace Liquid Crystal Technology for Reconfigurable SatCom systems”. In: *Nationale Konferenz Satellitenkommunikation in Deutschland*. 2017.

[Jos13] M. Jost. “Recent Development in Design and Applications of Passive Tunable Liquid Crystal (LC) Devices in the Millimetre-Wave (mmW) and THz Regime”. In: *Workshop-Proceedings European Microwave Week*. 2013.

Supervised Theses

- Roland Reese - *Fundamental investigations of continuously tuneable dielectric waveguides in the mmW-regime based on liquid crystal technology*, Master Thesis
- Ali Abdallah - *Design und Fertigung eines kontinuierlich steuerbaren Flüssigkristallphasenschiebers im W-Band*, Bachelor Thesis
- Ersin Polat - *Fundamental Investigations of Low-Loss, Non-Radiating Waveguide Topologies for Phase Shifting*, Master Thesis

Curriculum Vitae

Personal Information

Name:	Matthias Jost
Date of birth:	10. July 1985
Place of birth:	Birkenfeld (Nahe), Deutschland

Education

1996–2005 –	Gymnasium Birkenfeld, Birkenfeld (Degree: Abitur)
2005–2006 –	Community service Stefan-Morsch-Stiftung, Birkenfeld
2006–2012 –	Studies: Physics Johannes Gutenberg-Universität, Mainz (Degree: Diplom)
seit 2012 –	Research assistant Institute for microwave engineering and photonics, Technische Universität Darmstadt

Darmstadt, den 02.02.2018